

OPTICAL PERFORMANCE OF RANDOM ANTIREFLECTION STRUCTURED
SURFACES ON OPTICAL FLATS AND DIFFRACTIVE COMPONENTS

by

Karteek Kunala

A dissertation submitted to the faculty of
The University of North Carolina at Charlotte
in partial fulfillment of the requirements
for the degree of Doctor of Philosophy in
Optical Science and Engineering

Charlotte

2018

Approved by:

Dr. Menelaos Poutous

Dr. Glenn Boreman

Dr. M. Yasin Raja

Dr. Thomas Suleski

Dr. Ryan Adams

©2018
Kartek Kunala
ALL RIGHTS RESERVED

ABSTRACT

KARTEEK KUNALA. Optical Performance of Random Antireflection Structured Surfaces on Optical Flats and Diffractive Components.
(Under the direction of DR. MENELAOS K. POUTOUS)

Random anti-reflection surface structures (rARSS) are non-periodic, densely packed, sub-wavelength structures, fabricated on an optical surface. Light incident to such a boundary propagates from superstrate to substrate through a gradient effective refractive index profile, where the gradual transition reduces the reflective losses and increases the transmission through the interface. The present dissertation mainly discusses anti-reflection (AR) treatments on optical components by the implementation of rARSS. Two fundamentally different rARSS fabrication techniques on planar substrates are featured, for applications as optical windows in the visible and infrared (IR) wavelengths. The rARSS were fabricated on fused silica (FS) flat optical windows, which were first masked by a discontinuous metal layer, then followed by etching the substrate in a reactive-ion (RIE) plasma process. The physical characteristics of the rARSS are presented, such as, the effective depth and lateral dimensions of the random structures, and the resulting spectral transmission performance. It was found that rARSS on FS act as a broad-band anti-reflective treatment. Following, a different technique to create rARSS on Cleartran Zinc Sulfide (ZnS) is presented, by irradiating the surface with a high-power, nanosecond-duration pulsed laser, resulting in localized sputtering and re-deposition in atmospheric conditions. The surface is characterized by measuring the structure's height and lateral dimensions. The surface is then analyzed for presence of any contaminants, like zinc oxide (ZnO), due to the atmospheric conditions. The optical

performance tests show that rARSS on Cleartran ZnS acts as an AR treatment in the IR wavelength region as well. Finally, the plasma-etching method, used previously on the planar optical silica windows, was transferred to transmissive silica binary diffraction gratings. Two pre-fabricated commercially available transmission gratings were used to investigate the rARSS effects on their surfaces. A comparison study of the performance of the original gratings (unprocessed) and the rARSS enhanced gratings is done, using a multi-wavelength He-Ne laser (594nm, 612nm and 633nm), to measure the propagating diffracted order angles and, individual reflection and transmission diffraction efficiencies of all non-evanescent orders. The diffracted beams profiles were measured, to quantify any effects after rARSS fabrication. Tests were also performed to measure the diffraction efficiency at variable angles of light incidence (AOI), from 0° to 70° , to determine the rARSS performance for AOI greater than 40° and, were compared to a single-layered AR coated grating simulation. It is shown that the fabrication of rARSS on pre-existing binary FS gratings was possible and produced the desired reduction in diffracted reflection efficiency, and enhancement of the total diffraction transmission efficiency, while maintaining the original diffractive properties of the pre-fabricated gratings. The work verifies that rARSS are applicable to optical windows, as well as, diffraction gratings, increasing their spectral transmittance, without any component performance degradation.

DEDICATION

This dissertation is dedicated to...

...my parents, who have always been, and continue to be, the most amazing role models.
I would not have made it this far without their constant unconditional support and encouragement.

ACKNOWLEDGMENTS

First and foremost, I would like to express my sincere gratitude to my advisor Dr. Menelaos Poutous for the continuous support of my Ph.D study and related research, for his patience, motivation, and immense knowledge. His guidance helped me in all the time of research and writing of this thesis. I am grateful for all the time and energy he has given to me in my time at UNC Charlotte. I could not have imagined having a better advisor and mentor for my Ph.D study.

Besides my advisor, I would like to thank the rest of my thesis committee: Dr. Glenn Boreman, Dr. M Yasin Raja, Dr. Thomas Suleski, and Dr. Ryan Adams, for their insightful comments and encouragement, and for the hard questions which incited me to widen my research from various perspectives. I greatly appreciate all the time my committee has invested in me.

My sincere thanks also go to Dr. Ishwar Aggarwal, the Naval Research Laboratory, and the GASP fellowship for funding me during my graduate school career. I know that I am incredibly lucky to have been given such generous financial support and that without it completing this dissertation would have been much more difficult.

I would also like to thank the Center for Optoelectronics and Optical Communications for the use of its equipment and facilities. Thank you also to Dr. Robert Hudgins, Dr. Lou Deguzman, and Mr. Scott Williams for their patient training sessions and frequent help with equipment issues.

Thank you to the past and present members of the Optical Micro-Structured Interfaces Laboratory, Gopal Sapkota, Kevin Major, Abigail Peltier, Jason Case, Chris Wilson and Tom Hutchins, for all the training, troubleshooting, brainstorming, and

general support they've given me. I consider myself very lucky to have had such a supportive lab team.

And finally, I'm incredibly grateful to all my friends and family for their continuous support and encouragement throughout this entire process. I'd especially like to thank my parents for supporting me throughout writing this thesis and my life in general. I truly could not have done this without you.

TABLE OF CONTENTS

LIST OF TABLES	xi
LIST OF FIGURES	xiii
LIST OF ABBREVIATIONS.....	xix
CHAPTER 1: INTRODUCTION.....	1
1.1 Anti-Reflection Treatments.....	1
1.2 Fabrication Techniques	8
1.3 Optical performance characterization methods for rARSS.....	10
1.4 Application of AR treatment on Diffraction Gratings	12
1.5 Dissertation Overview.....	15
CHAPTER 2: RANDOM ANTI-REFLECTION STRUCTURED SURFACES ON FLAT OPTICAL WINDOWS (FUSED SILICA AND CLEARTRAN)	18
2.1 Introduction	18
2.2 Fused Silica	19
2.2.1 Introduction	19
2.2.2 Fabrication of rARSS on Fused Silica.....	20
2.2.3 Surface analysis and confocal microscopy of rARSS on Fused Silica.....	21
2.2.4 Optical Performance of rARSS on Fused Silica.....	24
2.2.5 Scanning electron microscope images and Granulometry	27
2.3 Cleartran Zinc Sulfide	30

2.3.1 Introduction	30
2.3.2 Fabrication of rARSS on Cleartran ZnS.....	34
2.3.3 Surface analysis and confocal microscopy of rARSS on Cleartran ZnS.....	37
2.3.4 Optical Performance of rARSS on Cleartran ZnS in Mid-IR Spectral region .	44
2.3.5 Scanning electron microscope images and Granulometry	45
2.4 Summary.....	49
CHAPTER 3: RANDOM ANTI-REFLECTION STRUCTURED SURFACES ON BINARY DIFFRACTION GRATINGS.....	51
3.1 Introduction	51
3.2 Fabrication of rARSS on binary diffraction gratings	55
3.2.1 Fabrication process	55
3.2.2 Scanning electron microscope images.....	57
3.3 Experimental setup and Optical performance testing	60
3.3.1 Experimental test setup.....	60
3.3.2 Measurement of diffraction order angular separation	63
3.3.3 Simulated diffraction order angular separation and efficiencies	66
3.3.4 Diffraction Efficiency measurements	69
3.3.5 Diffracted Beam profile measurements	78
3.3.6 Granulometry results	81
3.4 Optical performance vs angle of incidence	85
3.5 Diffraction efficiency comparison of measured and simulated gratings.....	92

3.6 Summary and Discussion	97
CHAPTER 4: CONCLUSIONS	101
4.1 Summary of Optical performance of Random Anti-reflection Structured Surfaces on Flat Optical Windows.....	101
4.2 Summary of Optical performance of Random Anti-reflection Structured Surfaces on Binary Diffraction Gratings	103
4.3 Potential Future Work	105
REFERENCES	107
APPENDIX A: Publications	111
APPENDIX B: List of Optical Components	112

LIST OF TABLES

Table 1: Etching process parameters of the RIE to fabricated rARSS on FS substrate. Four samples have been etched for varying etch times.	21
Table 2: Energy density and structure height values of three samples with similar irradiation per pulse energy and different number of irradiation pulses.	46
Table 3: Calculated 1 st and 2 nd Bragg angle of incidence in degrees for 1.595 μ m and 1.166 μ m period gratings.	62
Table 4: Measured 1 st and 2 nd Bragg angle of incidence in degrees for 1.595 μ m and 1.166 μ m period gratings	64
Table 5: Measured diffraction angles of the 1.595 μ m period grating, for all propagating orders of the pre-processed original (Blank) and the post-processed rARSS gratings, at 594nm, 612nm and 633nm, for three angles of incidence.	65
Table 6: Measured diffraction angles of the 1.166 μ m period grating, for all propagating orders of the pre-processed original (Blank) and the post-processed rARSS gratings, at 594nm, 612nm and 633nm, for three angles of incidence.	65
Table 7: Simulated diffraction angles of the 1.595 μ m period grating, for all propagating orders of the pre-processed original (Blank) grating, at 594nm, 612nm and 633nm, for three angles of incidence.	66
Table 8: Simulated diffraction angles of the 1.166 μ m period grating, for all propagating orders of the pre-processed original (Blank) grating, at 594nm, 612nm and 633nm, for three angles of incidence.	67
Table 9: Comparison between total transmission intensity of all propagating orders for the original (blank) and rARSS grating, for various angle of incidence at 594 nm, 612 nm and 633 nm, for the 1.595 μ m period grating.	71
Table 10: Comparison between total transmission intensity of all propagating orders for the original (Blank) and rARSS grating, for various angles of incidence at 594 nm, 612 nm and 633 nm, for the 1.166 μ m period grating.	72

Table 11: Percentage coverage density of voids and islands for bottom and top surfaces of 1.595 μm and 1.166 μm period gratings.....	83
--	----

LIST OF FIGURES

<p>Figure 1: Light incident on: (a) single layered AR thin film, (b) sub wavelength grating (SWG) structure and (c) random AR surface structure (rARSS). The side inserts show the refractive index variation as a function of vertical position from the superstrate, through the AR surface and, into the substrate.....</p>	2
<p>Figure 2: Simulated transmission of an ideal AR thin film ($n=1.204$) on Fused silica ($n=1.450$): (a) at normal incidence (0° AOI) over a wavelength range of $0.3 - 1.8 \mu\text{m}$ and (b) at 633 nm wavelength over 0° to 90° AOI, for both incident light wave polarization states. Both the plots show the transmission of bare fused silica as FS for comparison.</p>	4
<p>Figure 3: Simulated 0th order transmission of a 500nm period linear SWG on Fused silica ($n=1.45$) (a) at normal incidence (0° AOI) over a wavelength range of $0.2 - 1.0 \mu\text{m}$ and (b) at 633 nm wavelength over 0° to 90° AOI. Both plots show the transmission intensity for S and P incident light wave polarization states.</p>	6
<p>Figure 4: Measured transmission of rARSS on Fused silica ($n=1.45$) (a) at normal incidence (0° AOI) over a wavelength range of $0.3 - 1.8 \mu\text{m}$ and (b) at 633 nm wavelength vs AOI, for both incident light wave polarization states. Both plots show the transmission of bare fused silica as FS for comparison.</p>	7
<p>Figure 5: (a) Flow diagram depicting the general fabrication process of periodic subwavelength structures onto a substrate [14]. (b) Fabrication technique used in the present work to create rARSS structures on fused silica substrates.</p>	8
<p>Figure 6: General depiction of deposition technique to fabricate: (a) Conformal AR coated grating and (b) Layered AR coated grating.</p>	13
<p>Figure 7: Various diffractive optical components: (a) Binary diffraction grating, (b) Fresnel lens, (c) 1-dimentional and (d) 2-dimentional Spot array generators.</p>	14
<p>Figure 8: Depiction example of the difference between the maximum (R_z) and RMS (R_q) height of a random surface line profile.</p>	22

Figure 9: Depiction example of a bearing area length curve showing the percentage of material present for varying height into the substrate.	23
Figure 10: UV confocal microscope images of an unprocessed fused silica (left) and rARSS processed with 25min etch time (right).....	23
Figure 11: Bearing area length curve showing the variation with varying etch time.	24
Figure 12: Measured spectral transmission for fused silica substrate with rARSS fabricated on a single surface of the substrate. Five different substrates are shown, an unprocessed (Blank) FS substrate and 4 samples with different etch times. The measurements were taken at normal incidence (0°). The black dashed line indicates the theoretically possible maximum transmission for a single side rARSS processed FS substrate.	25
Figure 13: Measured spectral transmission for fused silica substrate with rARSS fabricated on both surfaces of the substrate. Two different samples are shown, an unprocessed (Blank) FS substrate and a 25 min etched sample. The measurements were taken at normal incidence (0°). The black dashed line indicates the theoretically possible maximum transmission.	26
Figure 14: Sample scanning electron micrograph of rARSS fabricated on FS substrate, using a RIE process with a 25min etch time, listed in Table 1.	27
Figure 15: Distributed histograms of the feature sizes corresponding to the SEM micrograph of the random structure on FS substrate shown in Fig. 3. The distribution of islands is represented by the Black bars and the voids by white bars. The total populations are normalized to the total surface area.	28
Figure 16: Transmission curve of the enhancement between an untreated and laser ablated Cleartran ZnS using a low power (power < 10mW) CW 325 nm wavelength laser [42].	32
Figure 17: EDAX measurement of the Cleartran substrate (a) before irradiation and (b) after irradiation with a CW laser (Previous OSS lab work) [42].	33
Figure 18: Measured Transmission of an unprocessed Cleartran ZnS sample.	34
Figure 19: Setup used to create random structures on Cleartran ZnS using nanosecond pulsed High power laser ablative irradiation.	35

Figure 20: Energy of incident pulse with varying Q-Switch delay time of the Nd: YAG laser used to irradiated Cleartran ZnS.	36
Figure 21: Microscope images of an unprocessed Cleartran (left) and after irradiation using laser ablation (right).....	37
Figure 22: EDAX measurement of the Cleartran substrate (a) before irradiation and (b) after irradiation with a Nd: YAG laser.	38
Figure 23: Maximum roughness as a function of (a) Net irradiation energy and (b) Irradiation energy per pulse. The number of pulses in both the plots have been specified using different markers. The dashed line represents the roughness of the non-irradiated Cleartran substrate.....	39
Figure 24: RMS roughness as a function of (a) Net irradiation energy and (b) Irradiation energy per pulse. The number of pulses in both the plots have been specified using different markers. The dashed line represents the roughness of the non-irradiated Cleartran substrate.....	40
Figure 25: (a) Maximum roughness and (b) RMS roughness as a function of number of irradiation pulses. The bars represent the maximum and minimum value of the measured roughness for a specific pulse number.....	41
Figure 26: Stratification ratio as a function of (a) Net irradiation energy and (b) Irradiation energy per pulse. The number of pulses in both the plots have been specified using different markers. The dashed line represents the roughness of the non-irradiated Cleartran substrate.....	43
Figure 27: Measured single side transmission, at 0° AOI, vs wavelength (μm) for a non-irradiated Cleartran and Cleartran with rARSS on one surface, fabricated using laser irradiation and re-deposition. The black dotted line represents the moving average trendline for each curve.....	44
Figure 28: SEM image of an rARSS structure on Cleartran ZnS, fabricated using Laser irradiation.	45
Figure 29: Scanning electron micrographs and lateral feature size distribution histograms of irradiated Cleartran substrate with (a) 10 pulses, (b) 3 pulses and (c) 1 pulse using a high-energy pulsed laser at 354nm. The average energy density per pulse was around $600\text{mJ}/\text{cm}^2$	47

Figure 30: General depiction of the various orders of the angular spectrum, for a binary diffraction grating on (a) reflection and (b) in transmission, due to the diffractive grating surface.	53
Figure 31: Measured transmission intensity of the fused silica witness flat across the test wavelength for unprocessed (original), single side processed, and double side processed.....	57
Figure 32: Top-down scanning electron micrographs of commercially available linear binary fused silica gratings with periods of: (a) 1.595 μ m and (b) 1.166 μ m. Micrographs of rARSS fabricated on the gratings with the respective periods above (c, d).....	59
Figure 33: Scanning electron microscope (a, c) tilted cross-sections and, (b, d) side-view cross-sections of rARSS fabricated on top of the gratings with periods of: (a, b) 1.595 μ m and (c, d) 1.166 μ m.	59
Figure 34: Experimental layout for measurement of diffraction efficiencies of all orders for the grating under test (G), using the detector (D) placed on a rotating stage (R). Polarization of incident light is controlled by rotating a half-wave plate (HWP) and a linear polarizer (LP).	60
Figure 35: Angle of incidence test setup for all gratings tested. (a) The grating is aligned at Normal incidence. (b) The grating is aligned at 1st Bragg angle of incidence, where the “-1st” reflected order goes back in the direction of the incident light. (c) The grating is aligned at 2 nd Bragg angle of incidence, where the “0th” reflected order is aligned along the normal to the grating plane.....	61
Figure 36: Simulated Transmission diffraction efficiencies of all orders for (a) 1.595 μ m and (b) 1.166 μ m period gratings at 594nm and S polarization grouped by angle of Incidence.	68
Figure 37: Measured reflection diffraction efficiencies of (a)1.595 μ m 0th order, (b)1.595 μ m +1st order, (c)1.166 μ m 0th order and (d)1.166 μ m +1st order for normal, 1st Bragg and, 2nd Bragg angles of incidence at 594 nm, 612 nm and 633 nm. Solid bars represent the original grating measurements, while the patterned bars show the same grating post-processed measurement with rARSS.....	70
Figure 38: Transmission diffraction efficiencies for the 1.595 μ m period grating at normal incidence (a-d). Comparison between efficiencies of all propagating orders for (a) unprocessed FS grating for S polarization, (b) rARSS FS grating for S polarization, (c) unprocessed FS grating for P	

polarization and (d) rARSS FS grating for P polarization, at each test wavelength. Similar plots at (a ₁ – d ₁) 1 st Bragg incidence and (a ₂ – d ₂) 2 nd Bragg incidence.	75
Figure 39: Transmission diffraction efficiencies for the 1.166μm period grating at normal incidence (a-d). Comparison between efficiencies of all propagating orders for (a) unprocessed FS grating for S polarization, (b) rARSS FS grating for S polarization, (c) unprocessed FS grating for P polarization and (d) rARSS FS grating for P polarization, at each test wavelength. Similar plots at (a ₁ – d ₁) 1 st Bragg incidence and (a ₂ – d ₂) 2 nd Bragg incidence.	77
Figure 40: Transverse beam profile comparison between original and rARSS grating, for -1 st and +1 st diffraction orders at normal incidence (a-b), 1 st Bragg incidence for 1.595μm period grating (c-d) and, 1 st Bragg incidence for 1.166μm period grating (a ₁ -b ₁). The data was measured for an incident wavelength of 612nm (S pol). The vertical (intensity) scale is logarithmic to accentuate differences between the profiles.	79
Figure 41: Transverse beam profile comparison between original and rARSS grating, for -1 st and +1 st diffraction orders at normal incidence (a-b), 1 st Bragg incidence for 1.595μm period grating (c-d) and, 1 st Bragg incidence for 1.166μm period grating (a ₁ -b ₁). The data was measured for an incident wavelength of 612nm (P pol). The vertical (intensity) scale is logarithmic to accentuate differences between the profiles.	80
Figure 42: Distributed histograms of the rARSS feature populations on 1.595μm period grating's: (a) Bottom surface and, (b) Top surface; as well as, 1.166μm period grating's: (c) Bottom surface and, (d) Top surface. The feature sizes correspond to the SEM micrographs of the random structure on the gratings shown in Fig. 3(c,d). The distribution of islands is represented by the black bars and the voids by white bars. The populations are normalized to the total surface area.	82
Figure 43: Visual representation of the percentage island coverage in the top and bottom of the rARSS grating with a period of (a) 1.595μm and (b) 1.166μm.	84
Figure 44: Measured transmission diffraction efficiency vs AOI for 1.595μm period grating at S polarization. The cross labels represent the original grating, while the circles represent the rARSS grating. The plots represent (a) Total summed efficiency and (b ₁ – b ₈) individual order efficiencies.	87

Figure 45: Measured transmission diffraction efficiency vs AOI for 1.595 μ m period grating at P polarization. The cross labels represent the original grating, while the circles represent the rARSS grating. The plots represent (a) Total summed efficiency and (b ₁ – b ₈) individual order efficiencies.....	88
Figure 46: Measured transmission diffraction efficiency vs AOI for 1.166 μ m period grating at S polarization. The cross labels represent the original grating, while the circles represent the rARSS grating. The plots represent (a) Total summed efficiency and (b ₁ – b ₅) individual order efficiencies.....	90
Figure 47: Measured transmission diffraction efficiency vs AOI for 1.166 μ m period grating at P polarization. The cross labels represent the original grating, while the circles represent the rARSS grating. The plots represent (a) Total summed efficiency and (b ₁ – b ₅) individual order efficiencies.....	91
Figure 48: Visual representation of the comparison between (a) original, (b) SLAR, and (c) rARSS grating.....	92
Figure 49: Measured and simulated transmission diffraction efficiency vs AOI for 1.595 μ m period grating at 612nm incidence wavelength (S polarization). The plots give a comparison between the original (blank), SLAR and rARSS grating. The plots represent (a) Total summed efficiency and (b ₁ – b ₈) individual order efficiencies.....	94
Figure 50: Measured and simulated transmission diffraction efficiency vs AOI for 1.166 μ m period grating at 612nm incidence wavelength (S polarization). The plots give a comparison between the original (blank), SLAR and rARSS grating. The plots represent (a) Total summed efficiency and (b ₁ – b ₅) individual order efficiencies.....	95
Figure 51: Figure showing the intersection point of +1 and -1 order for (a) unprocessed and (b) rARSS processed 1.595 μ m period grating.	96
Figure 52: Comparison of the variation of the intersection angle of ± 1 order with changing phase depth of the grating. The solid lines represent the simulated results and the individual points represents the measured data for both S and P incidence polarization.	97
Figure 53: Microscope image of (a) Fresnel lens and (b) Spot array generators.....	106

LIST OF ABBREVIATIONS

ALD	atomic layered deposition
AlN	aluminum nitride
AOE	advanced oxide etch
AOI	angle of incidence
AR	anti-reflection
ARSS	anti-reflection surface structures
Au	gold
C ₄ F ₈	octafluorocyclobutane
CCD	charge-coupled device
CHF ₃	trifluoromethane
CVD	chemical vapor deposition
CW	continuous wave
EDAX	energy-dispersive X-ray analysis
F	fluorine
FeCl ₃	ferric chloride
FS	fused silica
FTIR	Fourier-transform infrared
H ₂	hydrogen
HeNe	helium neon
HWP	half-wave plate
ISB	ion beam sputtering

ICP	inductively coupled plasma
IR	infrared
LP	linear polarizer
LWIR	long-wavelength infrared
MLA	microlens array
MWIR	mid-wavelength infrared
TE	transverse electric
Nd: YAG	neodymium-doped yttrium aluminum garnet
Ni	nickel
O ₂	oxygen
PAR	perfect anti-reflection thin film
PECVD	plasma enhanced chemical vapor deposition
PVD	physical vapor deposition
rARSS	random anti-reflective surface structures
RCWA	rigorous coupled wave analysis
RF	radio frequency
RIE	reactive ion etching
RMS	root mean square
RTA	rapid thermal annealing
R _q	root-mean-square roughness
R _z	maximum roughness
sccm	standard cubic centimeter per minute
SEM	scanning electron microscope

SF ₆	sulfur hexafluoride
Si	silicon
SiF ₄	silicon tetrafluoride
SLAR	single layered anti-reflective
SWG	sub wavelength grating
TE	transverse electric
TM	transverse magnetic
UNC	the University of North Carolina
UV	ultraviolet
VIS	visible
ZnO	zinc oxide
ZnS	zinc sulfide
ZnSe	zinc selenide

CHAPTER 1: INTRODUCTION

1.1 Anti-Reflection Treatments

When light travels through a boundary separating two materials with different refractive index, a fraction of the light intensity is reflected. Fresnel equations account for the reflected amount, which depends on the angle of incidence, refractive indices of both media and, the polarization of the incident light (Eq (1) and (2)). This phenomenon can be readily observed with many common transparent surfaces as well, such as: car windows, cameras and display panels; as well as, specialized optical windows, sensors, and laser high power optical systems.

$$r_s = \frac{n_1 \cos \theta_i - n_2 \cos \theta_t}{n_1 \cos \theta_i + n_2 \cos \theta_t} ; r_p = \frac{n_1 \cos \theta_t - n_2 \cos \theta_i}{n_1 \cos \theta_t + n_2 \cos \theta_i} \quad (1)$$

$$t_s = \frac{2n_1 \cos \theta_i}{n_1 \cos \theta_i + n_2 \cos \theta_t} ; t_p = \frac{2n_1 \cos \theta_i}{n_1 \cos \theta_t + n_2 \cos \theta_i} \quad (2)$$

In the Fresnel equations, the reflection coefficient “ r ” and the transmission coefficient “ t ” are ratios of the reflected and transmitted electric field amplitudes to that of the incidence wave electric field amplitude. The subscripts define the S (TE) and P (TM) incidence polarizations. In each equation “ θ_i ” is the angle of incident wave and “ θ_t ” is the angle of the transmitted wave with respect to the normal, where “ n_i ” is the refractive index of the incident medium and “ n_t ” the refractive index of the transmitted medium.

The power reflection coefficient (R) and the power transmission coefficient (T) are:

$$R = |r|^2; \quad T = \frac{n_2 \cos \theta_t}{n_1 \cos \theta_i} |t|^2 \quad (3)$$

Different techniques are used to reduce Fresnel reflections on optical elements. The simplest solution to suppress these reflections can be achieved by depositing a thin film of lower refractive index than the substrate, onto the element substrate. Thin film coatings on optical surfaces (interfaces) act as an anti-reflective (AR) treatment, by causing destructive interference between the reflected light from the top and bottom of the thin film (Figure 1(a)) [1].

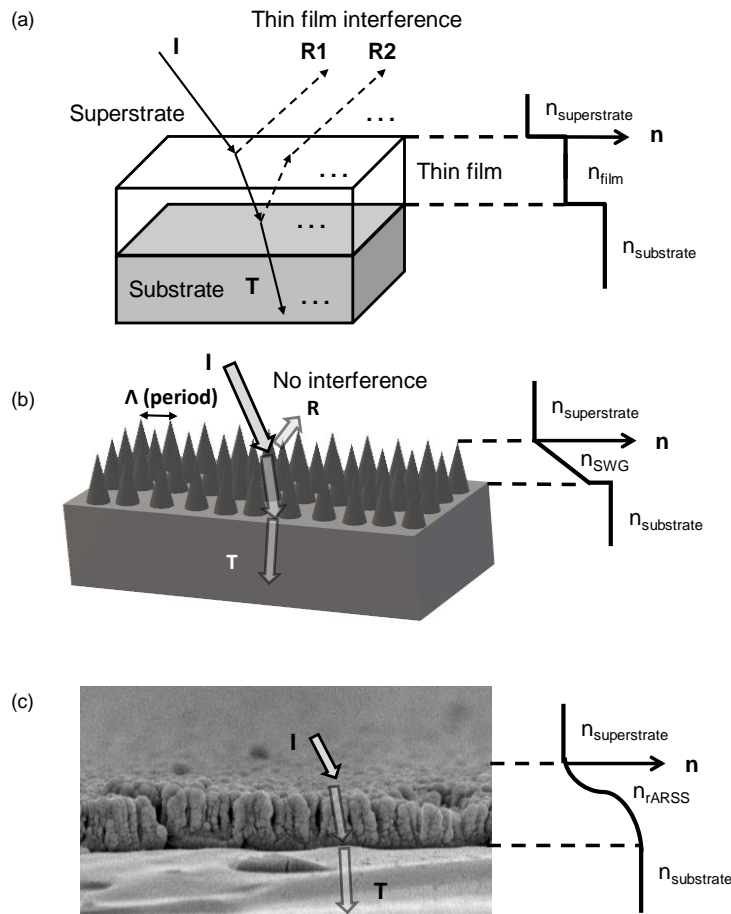


Figure 1: Light incident on: (a) single layered AR thin film, (b) sub wavelength grating (SWG) structure and (c) random AR surface structure (rARSS). The side inserts show the refractive index variation as a function of vertical position from the superstrate, through the AR surface and, into the substrate.

AR thin films are designed for specific wavelengths. To induce destructive interference between the reflected light waves from top and bottom of the thin film, a phase difference of $m\pi$ is required, for m restricted to odd integer value. The relative phase difference between the waves, is a consequence of the optical path length difference travelled by each of the reflected wave fronts. This occurs for a film thickness of $\lambda/4$ and for an index of refraction of the film equal to $\sqrt{n_{superstrate} n_{substrate}}$. For a thin film, of thickness $\lambda/4$ (quarter wave), interference for the transmitted and reflected waves depends on the incident wavelength and angle. Simulation of a perfect anti-reflective (PAR) thin film on fused silica (FS) substrate indicate that maximum transmission can be achieved at the desired wavelength but has a reduced transmission over a broad spectral bandwidth (Figure 2(a)), rendering thin film performance bandwidth non-uniform [2]. Changes in angle of incidence (AOI), changes the optical path length and the constructive interference of the transmitted wavefronts, reducing the transmission intensity at higher incidence angles (Figure 2(b)) [3]. In many cases the specific index required for a perfect AR thin film coating, does not exist and people design multilayered thin film coatings. Multi-layered thin film coatings are often preferred as an AR treatment, due to high-transmission efficiency and broad-band designs, but their fabrication can be complicated due to repetitive layer depositions, and their large total number of layers. Multi-layered AR thin film coatings contain a minimum of two dissimilar materials, which further introduces thermal mismatches and mechanical instability due to deposition-induced stresses in the interfacial regions.

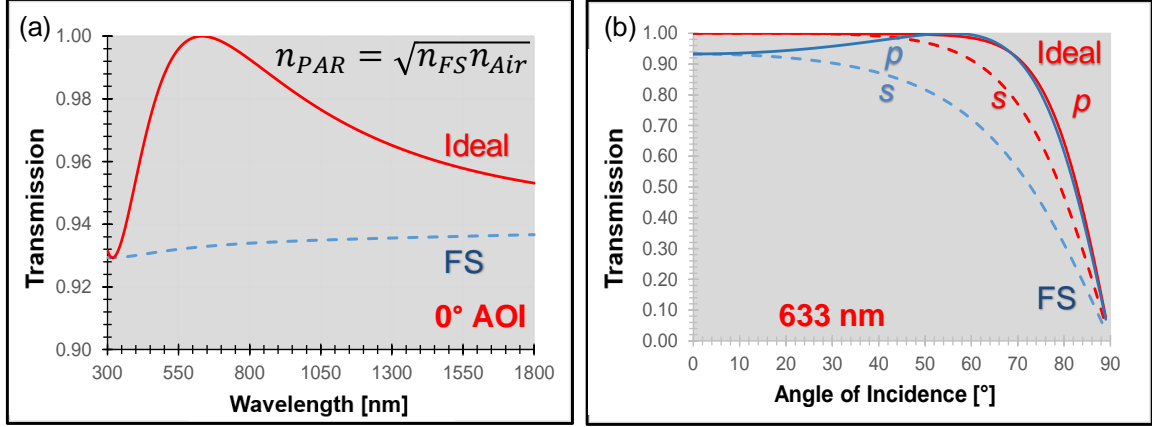


Figure 2: Simulated transmission of an ideal AR thin film ($n=1.204$) on Fused silica ($n=1.450$): (a) at normal incidence (0° AOI) over a wavelength range of $0.3 - 1.8 \mu\text{m}$ and (b) at 633 nm wavelength over 0° to 90° AOI, for both incident light wave polarization states. Both the plots show the transmission of bare fused silica as FS for comparison.

An alternative to conventional AR thin film coatings are periodic sub-wavelength gratings (SWG) fabricated on the substrate's surface, also known as anti-reflection surface structures (ARSS) or "Moth Eye" structures.

The general grating equation determines the transmitting and reflecting orders through a grating, given by:

$$\sin \theta_m - \sin \theta_i = m(\lambda/\Lambda) \quad (4)$$

Where light propagating at an incident wavelength " λ " enters the grating, with a period of " Λ ", at an angle " θ_i " with respect to the grating normal, and transmits " m " orders, each at an angle of " θ_m " relative to the grating normal. This equation must be satisfied for an order " m " to propagate through the grating, where " m " is an integer.

From equation 4, for wavelengths (λ) greater than the period of the grating (Λ), at normal incidence ($\theta_i = 0^\circ$), only the 0th order transmits and reflects, all other orders become evanescent. This condition can be used to define a sub-wavelength grating. Optimizing the height of the grating, such that a linear change in the refractive index occurs across the interface (Figure 1(b)), rather than a step index change (Figure 1(a)), reduces the Fresnel reflection to act as an AR surface [4, 5]. For wavelengths (λ) less than the period of the grating (Λ) at normal incidence ($\theta_i = 0^\circ$), higher diffraction orders become non-evanescent reducing the transmission intensity of the 0th diffraction order, which is now considered a super-wavelength grating. The simulation results of a 500nm period linear grating on fused silica shows how the grating acts as SWG for $\lambda > 500\text{nm}$ and super-wavelength grating for $\lambda < 500\text{nm}$. The transmission intensity of the 0th order versus incident wavelength in Figure 3 (a) shows a high intensity for $\lambda > 500\text{nm}$, acting as a SWG and for $\lambda < 500\text{nm}$ the transmitted intensity reduces for the 0th order, due to higher diffraction orders becoming non-evanescent, acting as a super-wavelength grating. The transmission intensity of the SWG also depends on the AOI. Due to reduced diffraction efficiency of the propagated orders at higher AOI, the total transmission intensity of SWG reduces (Figure 3(b)) [6].

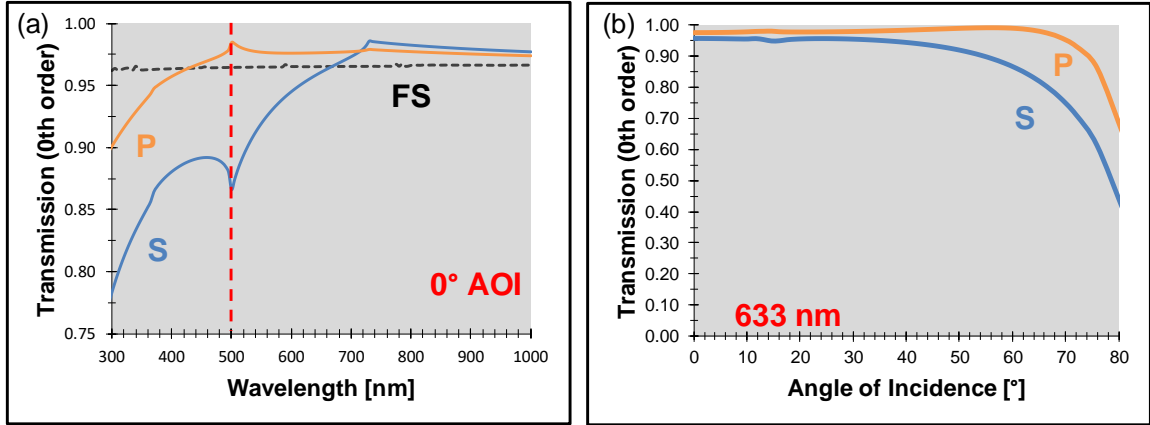


Figure 3: Simulated 0th order transmission of a 500nm period linear SWG on Fused silica ($n=1.45$) (a) at normal incidence (0° AOI) over a wavelength range of $0.2 - 1.0 \mu\text{m}$ and (b) at 633 nm wavelength over 0° to 90° AOI. Both plots show the transmission intensity for S and P incident light wave polarization states.

Random anti-reflection surface structures (rARSS) are a different solution to AR treatment. These are random (non-periodic), densely packed, sub-wavelength structures fabricated on the substrate's surface. The incident light sees a gradient effective refractive index change from superstrate to the substrate, due to the gradual increase in the ratio of glass to air volume (Figure 1(c)). An effective medium layer model can be used to approximate the random structures for analysis purposes, where the effective gradual transition in refractive index value from ambient to substrate, reduces the reflective losses and increases the transmission through the interface [7]. The height of the random structures determines the range of wavelength for which the random structures act as an AR treatment. Increasing the height of the structures shifts the maximum enhancement to a longer wavelength region. Reports by Douglas S. Hobbs, et. al [8] have indicated wide broadband transmission enhancement achieved by random AR structures on borosilicate glass, fused silica, plastic and silicon in visible region. Recent reports by Byron Zollars, et. al [9] have indicated high transmission due to random structures on ZnS and ZnSe

windows over broad spectral ranges from near-IR to far-IR, over a range of incidence angles from 0° to 70° . Figure 4 (a) shows the measured transmission intensity of fused silica (FS) substrate at 0° AOI, post and pre-processing of rARSS. The random structures on fused silica gave rise to a broadband enhancement with maximum intensity at 633nm wavelength. Figure 4 (b) shows the transmission intensity for both S and P incident polarizations for variable AOI at 633nm incident wavelength, where the original FS substrate is compared to the rARSS processed substrate [10]. The rARSS processed substrate gave a high transmission intensity to about 55° AOI with similar transmission for both S and P incident polarizations [10, 11]. This polarization insensitivity at a high AOI was observed only for rARSS surface treatment, whereas for thin film and SWG, the polarization splitting starts at around 30° AOI. The random structure's thermal and stress properties are identical to the substrate as they are fabricated into the surface of the substrate, resulting in a AR surface which can work under varying temperature and environmental conditions [12, 13].

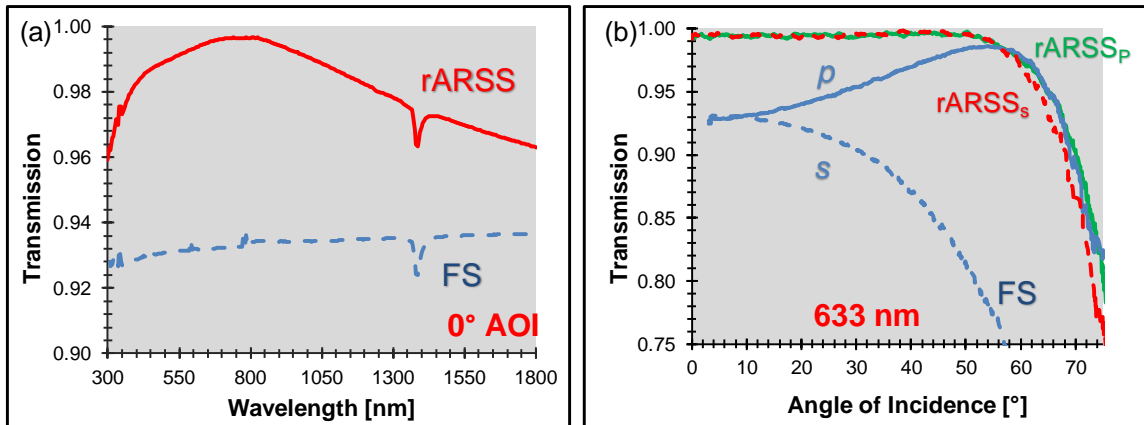


Figure 4: Measured transmission of rARSS on Fused silica ($n=1.45$) (a) at normal incidence (0° AOI) over a wavelength range of $0.3 - 1.8 \mu\text{m}$ and (b) at 633 nm wavelength vs AOI, for both incident light wave polarization states. Both plots show the transmission of bare fused silica as FS for comparison.

1.2 Fabrication Techniques

The fabrication techniques for SWG structures is more complicated compared to that of the random surface structures. Figure 5(a) depicts the general fabrication process of periodic subwavelength structures onto a substrate. To realize a SWG, the substrate is first coated with a photosensitive polymer (photoresist) and lithographic techniques are used to expose the image of the periodic geometry on the resist. The photoresist mask can be created using either direct exposure of the photoresist or by using an interference pattern projection. The resist lithograph is then etched to transfer the pattern into the surface of the substrate, and any remaining resist is stripped off, leaving a periodic structure onto the substrate [14].

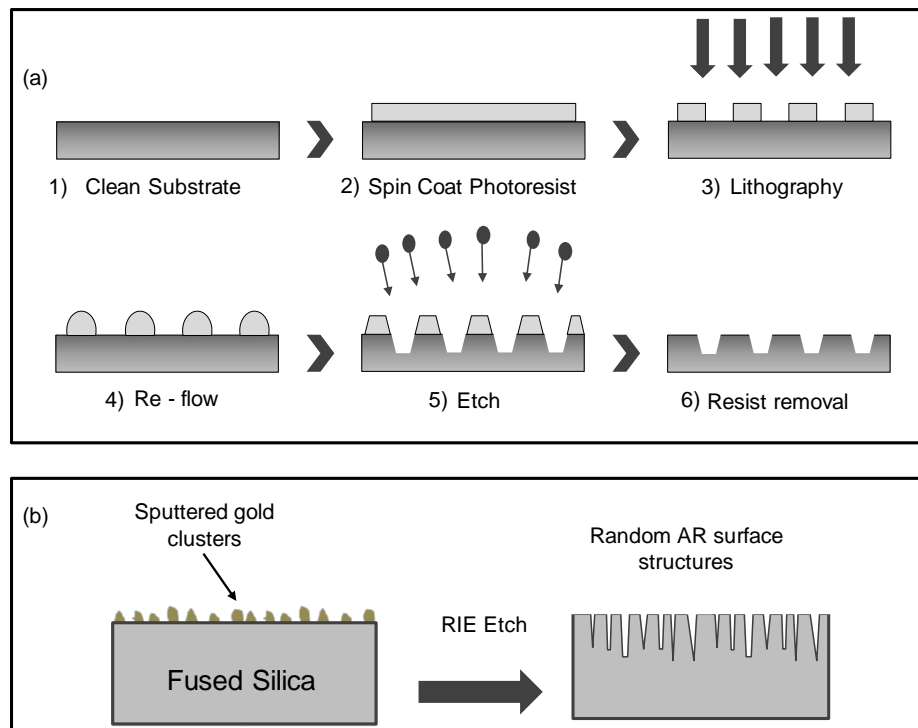


Figure 5: (a) Flow diagram depicting the general fabrication process of periodic subwavelength structures onto a substrate [14]. (b) Fabrication technique used in the present work to create rARSS structures on fused silica substrates.

For rARSS structures, a variety of fabrication methods has been investigated to-date, on many types of substrate materials [8, 14-16]. The fabrication methods can be grouped into two large classes, “bottom-up” and “top-down”. Nanostructures are created using “bottom-up” methods by different growth techniques like solution processing [17], and physical or chemical vapor deposition (CVD) [18, 19]. The “top-down” methods use wet or dry etching to transfer these structures permanently into the substrate. The etching process can be done either with or without prior masking [2]. Fabrication of anti-reflective microstructures has been reported for optical windows in the visible wavelength, such as fused silica and silicon [8] to infrared wavelength optical windows ZnS and ZnSe, using reactive ion etching (RIE) and inductively coupled plasma (ICP) etching processes, with or without metallization masking [9]. The structures have also been created on borosilicate glass and plastic polymers, and various IR optical windows [8, 13-15]. Certain groups have reported a technique where nanostructures have been created by self-masking using specific plasma two-cycle passivation-etching processes [20, 21].

Figure 5(b) represents the technique used in this dissertation to fabricate the random nanostructures on FS. The fabrication process involved the deposition of a thin discontinuous layer of gold (<20nm) as a partial mask using a sputter deposition system. The discontinuous layer of gold is used to initialize the random etch process. A reactive-ion plasma etching step followed, using a mixture of SF₆ and O₂ gas plasma. The surface post-processing showed that no gold on the surface was left after the plasma etch was

completed, resulting in a random structured surface on the substrate. A detailed discussion about the etching parameters of the RIE process is included in Chapter 2.

1.3 Optical performance characterization methods for rARSS

There are many techniques to quantify the effectiveness of an anti-reflective treatment onto an optical substrate. It sometimes depends on the desired application of the optical component on which we fabricate these structures. The overall goal is to achieve transmission intensity enhancement, over the desired wavelength range. For example, in the case of optical windows, enhanced transmittance is required over specific wavelength bandwidths, at selectable AOI and light polarization states. For optical components with focusing capabilities such as lenses, it is important to observe what the rARSS structures does to the profile of the incident beam as it passes through the optical component. And for diffractive optical components such as gratings, their diffractive performance such as the angular separation of the orders, period and duty cycle should not change due to rARSS fabrication.

Previous work by members of our group have verified that the fabrication of random subwavelength structures onto the substrates act as an AR treatment. They were successful in creating random structures on fused silica optical windows with a broadband enhancement. It was shown that the enhancement occurs for variable AOI and, polarization insensitivity was achieved for a very high AOI [10, 11]. Courtney Taylor's dissertation work included the fabrication of these random structures on 1" diameter lenses. She did a detailed analysis of the effects of rARSS as an AR treatment on curved

substrates [22]. The work done by Abigail Peltier was concentrated on fabrication of rARSS on microlens arrays (MLAs). She was successful in getting an enhanced transmission and did a detailed study on the effects of rARSS to the MLA beam profiles.

In this dissertation, transmission measurements were taken at normal incidence, over the broadband transmission wavelength range of the optical window. It is important to show that an enhancement in the transmission intensity is observed due to the rARSS treatment and not just a reduced reflection intensity. As reduced reflection intensity might result in increased scattered light, and not enhancing the specular transmission. All the transmission measurements were made for unprocessed substrates before fabrication of rARSS, to have a reference and to compare the data after AR treatment. Specific details of the spectrophotometers used to measure the transmission will be discussed in chapter 2.

For the diffractive optics, as the incident light separates an angular spectrum of different diffraction orders, a He-Ne laser was used as a source instead of a spectrophotometer. A standard photodiode power sensor was used to measure the intensity of the diffracted orders, and CCD camera beam profiler was used to compare the beam profiles of the incident light, when passed through the unprocessed and rARSS-processed optical components. This was done to get a complete understanding of the effects of the random structures on optical components. To quantify the dimensions of the structures created on the substrate, a UV confocal microscope was used to measure the height (R_z) of the structures and, granulometry was used to quantify the size distribution (lateral dimensions - $S(x,y)$) of the random structures [23]. Scanning electron microscope (SEM) images of the rARSS substrates were obtained and the high-resolution images

were used to quantify the lateral size of the random structure. The granulometry program processed the SEM images, to obtain the distribution of various sizes of pixel clusters. SEM images give details regarding the lateral dimensions of the random structures, via image processing numerical operators such as: erosion and dilation, opening and top-hat transform, used to find the boundaries of the fine random structures. Image filtering techniques like salt and pepper filtering, ASF (Alternating sequential filtering) and opening filters are used to remove the noise from SEM image [23]. This technique is used to create a histogram to show the size distribution of the structures present on the surface. The calculation results in an average lateral size dimension of the random structures and their percent area coverage.

The scattering of the random surface depends on the structures height (R_z) and the structure size distribution in the plane of the substrate (x, y). The enhancement in transmission due to the random structures depends on scattering through the structure which varies with the structure parameters. Low scattering is desired for an enhancement in the transmission for the random structure to act as an anti-reflective surface.

1.4 Application of AR treatment on Diffraction Gratings

Most reported work on rARSS has been limited to planar surfaces, such as optical windows. Some reports are available for lens surfaces as well [22, 24, 25]. Diffractive elements, such as gratings, also have Fresnel reflection losses. Diffraction gratings have been widely used as spectroscopic components, laser tuning, optical pulse compressing devices and beam splitters. The goal is to reduce back scattered reflections from the

diffractive optical components to enhancing the propagating transmission intensity in the optical systems.

A common technique to fabricate diffraction gratings is by micro-lithographic techniques. Where the substrate is coated with a photosensitive material and the required pattern is created on the photoresist by lithographic techniques, which is then transferred into the substrate by dry etching using reactive ion plasma.

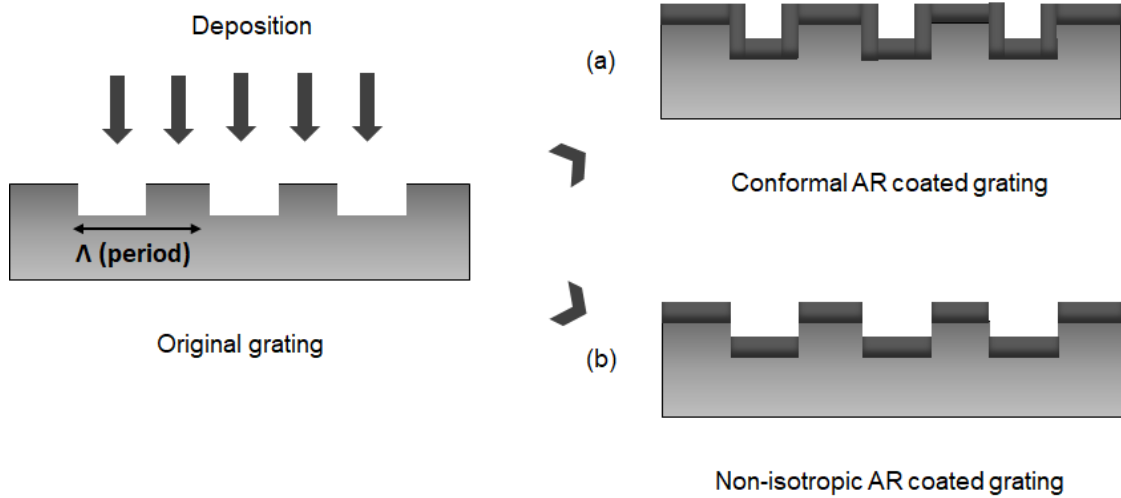


Figure 6: General depiction of deposition technique to fabricate: (a) Conformal AR coated grating and (b) Layered AR coated grating.

Reduction of reflectance from dielectric gratings can be accomplished using thin-film coatings by a variety of deposition methods, such as: ion-beam sputtering (IBS), atomic layer deposition (ALD) [26-29], layer-by-layer assembly [30], plasma-enhanced chemical vapor deposition (PECVD) [31], or physical vapor deposition (PVD) [32]. The coatings vary from conformal, as in the case of atomic layer deposition (Figure 6 (a)), to layered without sidewall coverage, as is the case of physical vapor deposition (Figure 6 (b)). In all cases the AR coating should be considered as part of the grating design, as it

will perturb the grating's diffractive performance by the introduction of the deposited dielectric layers [33]. The goal is to fabricate rARSS structures on gratings as an anti-reflective treatment, to suppress Fresnel reflectivity and enhance transmission, while retaining the diffractive properties of the original unprocessed grating.

Few reports are available on fabrication of tapered (cone-shaped) subwavelength nanostructures, integrated on the surface of a microscale diffractive element. While they have achieved a very low reflection loss with periodic patterns on top of the gratings, the fabrication process included photoresist spin coating, etching (masking using lithography), followed by mask removal for the subwavelength nanostructures, then a repetition of the fabrication cycle in order to fabricate the diffractive grating itself [34]. No experimental work has been found in the literature to-date, where an AR treatment has been presented for pre-fabricated diffraction gratings. Some of the work present in this dissertation describes an AR treatment for pre-fabricated, commercially available, binary gratings. This also increases the scope of AR treatment on other existing and available diffractive elements like holograms, spot array generators and Fresnel lenses (Figure 7).

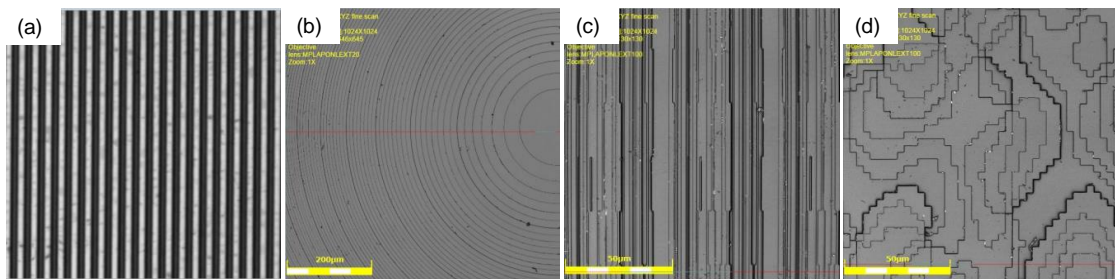


Figure 7: Various diffractive optical components: (a) Binary diffraction grating, (b) Fresnel lens, (c) 1-dimensional and (d) 2-dimensional Spot array generators.

1.5 Dissertation Overview

The present work discusses anti-reflection treatments on optical components by fabrication of random surface structures. Chapter 2 presents fabrication of rARSS onto FS and Cleartran ZnS optical windows, and how that affects their performance. The rARSS were fabricated on FS substrate by depositing a thin layer of gold, then etching the substrate using a Fluorine plasma RIE process. A comparison in the spectral transmission is made for various etch times, to achieve maximum transmission enhancement in the visible wavelength region (300-800nm). The physical characteristics of the rARSS were measured to get an estimate of the effective depth and lateral dimension of the random structures. The effective depth is measured using a confocal microscope and, the lateral dimensions were studied using scanning electron microscopy and granulometry image processing techniques. It is shown that rARSS on FS acts as a broad-band anti-reflective treatment.

Chapter 2 also explores a different fabrication technique used to create rARSS on Cleartran ZnS optical windows, where any etching or lithographic processes were not involved. The technique involves irradiating a Cleartran substrate with a high-power, nanosecond-duration pulsed laser, resulting in localized sputtering and redeposition, in atmospheric conditions. Micro and nano-structures are formed on the surface of the substrate, and consequently act as an AR treatment. The surface is characterized by measuring the structure's height and lateral dimensions, just as in the FS-etched surface. The surface is analyzed for presence of any contaminants like zinc oxide (ZnO), due to irradiation in atmospheric conditions. The optical performance tests were carried out in

the IR wavelength region and it is demonstrated that rARSS on Cleartran ZnS acts as an AR treatment. The goal of Chapter 2 was to show two fundamentally different techniques to fabricate rARSS on two planar substrates that are used as optical windows for visible and IR wavelength applications.

Chapter 3 expands the work from planar optical windows to diffraction gratings. This chapter focuses on characterizing the optical performance of near-wavelength binary fused silica gratings, with rARSS optimized for flat FS substrates. Two pre-fabricated commercially available transmission gratings were used to investigate the rARSS effects on diffraction gratings.

The fabricated rARSS on fused silica diffraction gratings were characterized using scanning electron micrographs to observe the differences in the surface of the grating post-and pre-rARSS fabrication. A comparison study of original gratings (unprocessed) and the rARSS enhanced gratings is done by using a multi-wavelength He-Ne laser to measure the propagating diffracted order angles and individual reflection, and transmission diffraction efficiencies of all orders. The intensity profile of the propagating diffracted beams is measured, to quantify any effects after rARSS fabrication. The work presented includes measurements at three incident wavelengths (594nm, 612nm and 633nm), three angles of incidence (normal, 1st Bragg and 2nd Bragg) and, both S and P polarization states. The surface is then characterized using granulometry, to obtain the lateral feature sizes of the rARSS. This was done to observe any differences between the structural size of the rARSS in the grooves (bottom) and the top of the grating surface.

Further the study includes performance measurements of the gratings at a varied angle of incidence from 0° to 70° . This was done to determine the gratings optical performance due to the random profile for AOI greater than 40° . A perfect single-layered anti-reflective (SLAR) grating was simulated and its optical performance was compared to the measured data of rARSS processed grating.

Chapter 4 of this dissertation contains the final conclusions drawn from the work presented in Chapters 2 and 3. It also discusses some potential future work that could be explored from the results of the work presented here.

CHAPTER 2: RANDOM ANTI-REFLECTION STRUCTURED SURFACES ON FLAT OPTICAL WINDOWS (FUSED SILICA AND CLEARTRAN)

2.1 Introduction

In this chapter, methods of fabricating rARSS onto fused silica (FS) and Cleartran Zinc Sulfide (ZnS) optical windows are studied. In section 2.2, rARSS were fabricated on fused silica substrates using gold (Au) masking and reactive-ion etching (RIE). Results are shown for spectral transmission of the rARSS FS substrate in visible wavelength region (300-800nm). The resulting rARSS population and the structure dimensions has been studied using scanning electron microscopy and granulometry image processing techniques. This section compares results between samples processed for different etching times, to relate fabrication process to transmission enhancement values. In section 2.3, a new technique for rARSS fabrication on Cleartran ZnS is introduced. The technique involves irradiating a Cleartran substrate with a high-power laser pulse, resulting in sputtering and redeposition. This creates micro and nano-structures on the surface of the substrate, that act as an AR treatment in the infrared (IR) wavelength region. The surface is then analyzed for presence of any contaminants, like zinc oxide (ZnO), due to irradiation in atmospheric conditions. The structure's height and lateral dimensions are then measured using a UV confocal microscope and scanning electron microscope, to better understand the structural properties of the rARSS fabricated on Cleartran. Section 2.4 summarizes the fabrication techniques, optical performances, and presents conclusions on the effect of rARSS on FS and Cleartran.

2.2 Fused Silica

2.2.1 Introduction

As discussed in chapter 1, there are various fabrication techniques to create random structures on FS optical windows. The process used in the thesis is a two-step process, where Au is sputtered on FS substrate, which is then etched in a RIE plasma to create the rARSS surface.

RIE is a dry plasma etching technique, powered by a radio frequency (RF) driven electromagnetic plasma. The chamber contains two electrodes (coil and platen), with the substrate resting on the bottom electrode (platen). A mixture of gases is required to etch, depending on their reactivity with the specific substrate. FS substrate reacts with fluorine-based gases, such as sulfur hexafluoride (SF_6), trifluoromethane (CHF_3), and octafluorocyclobutane (C_4F_8). The plasma is generated by the RF power source between the two electrodes. The F_2 gas is attacked by the plasma electrons to generate neutral radicals (F) and ions (F_2^+). The radicals diffuse towards the substrate and adsorb onto the surface. The ions accelerate vertically and bombard the substrate. These radical and ion bombardment onto the substrate surface produces SiF_4 , which desorbs and gets removed by the outflow of gases. The complete etch process depends on the operating parameters such as: chamber pressure, plasma power, RF frequency, bias potential across the electrodes, flow rate, composition of the gases, and the temperature of the platen. Depending on the type of etch and the substrate, the processes parameters are chosen

accordingly to achieve high etch rate, uniformity, selectivity and required shape of the features etched into the substrate [35-38].

It must be noted that the process parameters vary from one specific tool to another. Our lab group has been successful in past efforts fabricating rARSS on FS using the Plasma-Therm 7000 etcher. The fabrication of rARSS on FS substrates, and the process optimization in this chapter was achieved using an STS advanced oxide etcher (AOE) tool. Although the initial processes variables from the previous tool were used for guidance, the final process parameters on AOE were completely different from that of Plasma-Therm 7000.

2.2.2 Fabrication of rARSS on Fused Silica

The initial step of the fabrication process involved a deposition of thin layer of Au on the FS substrate, using an AJA sputter deposition tool (ATC 1800-F). The thickness of the Au layer was kept less than 20nm to act as a partial discontinuous mask. This non-uniform (random) mask is used to initialize the random etch process. The Au coated FS substrate is then etched using an STS-advanced oxide etcher (AOE), in a mixture of SF₆ and O₂ gas plasma.

Table 1 gives the various process parameters used to etch FS substrates. The coil power was set to zero for all processes, to get a diffused plasma, so that the ion bombardment is not very strong on the surface of the substrate. The etch time was varied from 25 to 75 min to observe any variation in transmission enhancement.

Table 1: Etching process parameters of the RIE to fabricated rARSS on FS substrate. Four samples have been etched for varying etch times.

Parameters				
Platen Power	60 W	60 W	60 W	60 W
Coil Power	0 W	0 W	0 W	0 W
SF ₆ Flow rate	50 Sccm	50 Sccm	50 Sccm	50 Sccm
O ₂ Flow rate	5 Sccm	5 Sccm	5 Sccm	5 Sccm
Pressure	24 mT	24 mT	24 mT	24 mT
Temperature	20°C	20°C	20°C	20°C
Etch Time	75 min	40 min	30 min	25 min

2.2.3 Surface analysis and confocal microscopy of rARSS on Fused Silica

Roughness measurements were carried on the irradiated regions using a UV confocal microscope (OLYMPUS OLS4000). Two roughness quantities, R_z and R_q , were measured. R_z is the max peak-to-valley (p_i, v_i) roughness of the surface described by Equation 5. It gives the maximum height of the structured pattern, while R_q is the root mean squared (RMS) roughness of the surface described by Equation 6. It represents the standard deviation of the height distribution of the structured pattern [39]. Figure 8 shows a general depiction of the difference between the maximum and RMS height of a random surface profile. Where p_i is the height of each peak, v_i is the depth of each valley and y_i is the height of each point in the random surface profile.

$$R_z = \frac{1}{N} \left(\sum_{i=1}^N p_i - \sum_{i=1}^N v_i \right) \quad (5)$$

$$R_q = \sqrt{\frac{1}{N} \left(\sum_{i=1}^N y_i^2 \right)} \quad (6)$$

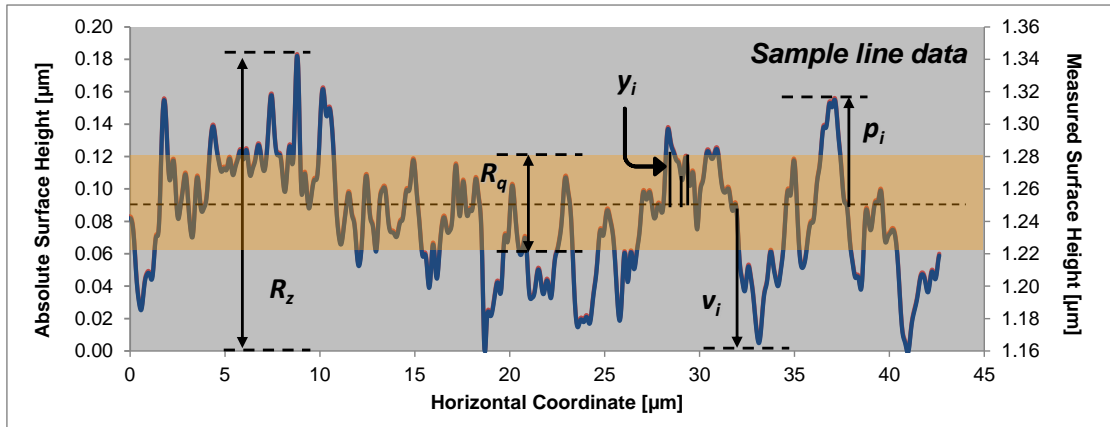


Figure 8: Depiction example of the difference between the maximum (R_z) and RMS (R_q) height of a random surface line profile.

Figure 9 shows the bearing area curve of a surface to describe the effective depth of the roughness created on a substrate. It shows the percentage of material present at each height, when measuring from air (0% material) into the substrate (100% material). It is an indicator of the change of refractive index from air to the substrate. Having a high slope for the linear region, gives a smoother transition of refractive index leading to low reflection and more transmission enhancement.

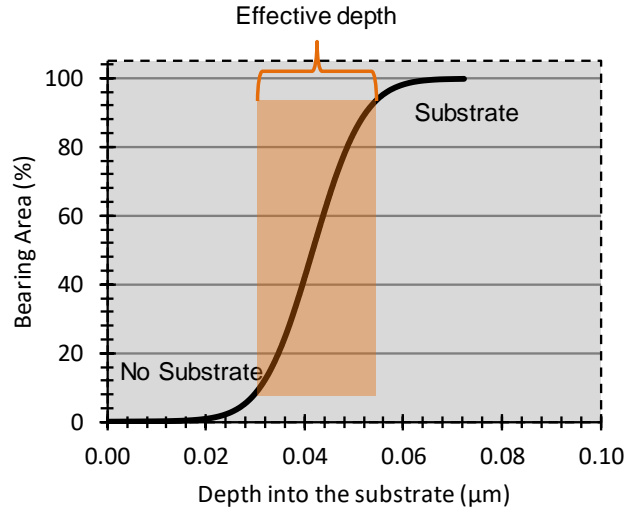


Figure 9: Depiction example of a bearing area length curve showing the percentage of material present for varying height into the substrate.

Microscope images have shown a modification of surface after fabrication of rARSS on fused silica substrates (Figure 10). For the 25min etch time (maximum enhancement substrate: discussed in Section 2.2.4) the measured value of R_z was $0.509\mu\text{m}$ and R_q was $0.053\mu\text{m}$.

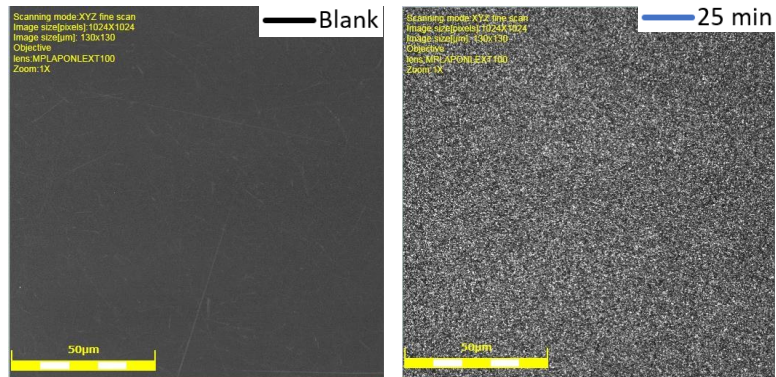


Figure 10: UV confocal microscope images of an unprocessed fused silica (left) and rARSS processed with 25min etch time (right).

The bearing area curves were compared for different etch times (Figure 11). It was observed that as the etch time increases, the depth into the substrate increases for 25, 30 and 40min. But for the 75min etch, the surface becomes smooth again, reducing the roughness due to overexposure of the substrate to the plasma.

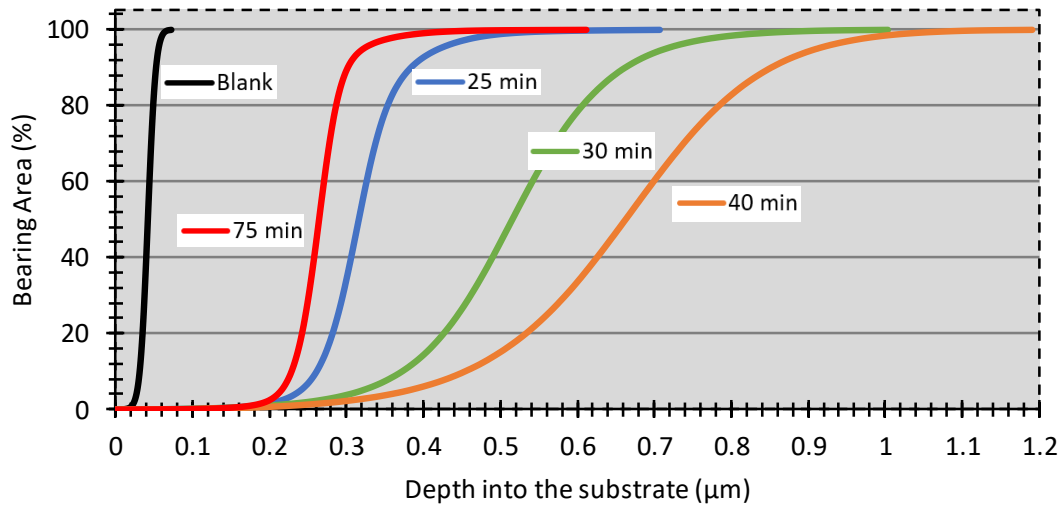


Figure 11: Bearing area length curve showing the variation with varying etch time.

2.2.4 Optical Performance of rARSS on Fused Silica

Optical transmission measurements were conducted on the rARSS FS substrates. Transmission of an unprocessed FS substrate was also measured, to compare with the etched FS substrates. The transmission measurements were made at normal incidence (0°), across the 300 – 800 nm wavelength region. Figure 12 shows the transmission plot of the substrate with varying etch times and the theoretically possible maximum

transmission. The graph displays transmission of FS substrate processed with rARSS on only one side of the substrate. The measurements show a blue shift for the scattering edge with decreasing etch time, as well as, increasing transmission enhancement values in the visible (VIS) and near-infrared (NIR) wavelength regions. A similar effect was observed for the bearing area curves (Figure 11), where 40min had the maximum depth into the substrate, due to which the maximum enhancement shifts towards the higher wavelengths. And for the 75min etch, the roughness change was less as shown in Figure 11, due to which no enhancement was observed either. The maximum enhancement was observed for a 25 min etch time with 96.5% transmission from 500 – 800 nm wavelength region, which is the theoretical possible maximum transmission for a FS substrate with AR treatment on a single surface with Fresnel reflectivity of 3.5% on the other surface.

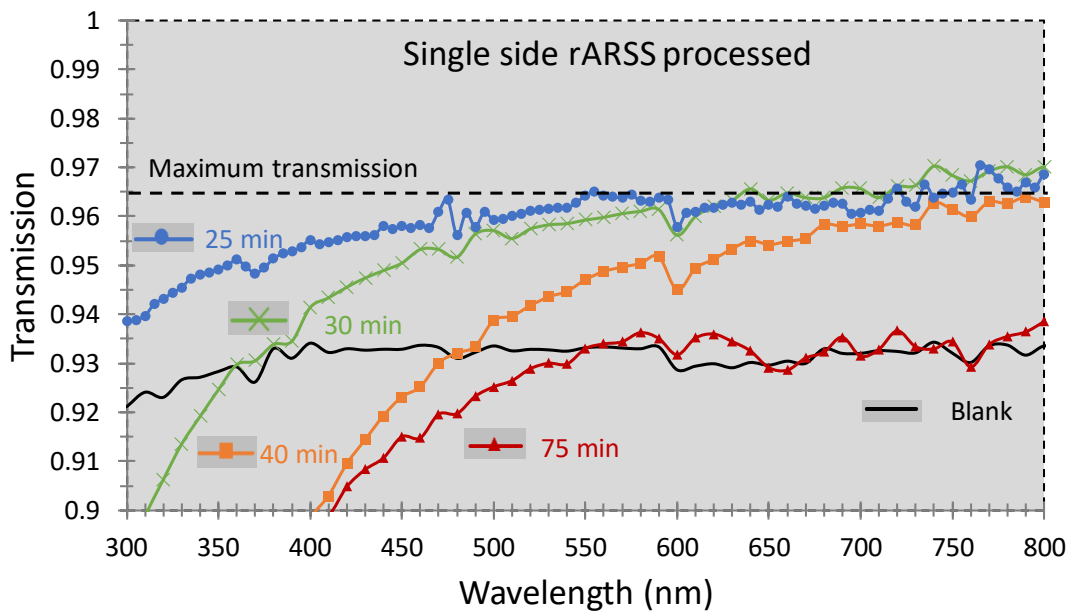


Figure 12: Measured spectral transmission for fused silica substrate with rARSS fabricated on a single surface of the substrate. Five different substrates are shown, an unprocessed (Blank) FS substrate and 4 samples with different etch times. The measurements were taken at normal incidence (0°). The black dashed line indicates the theoretically possible maximum transmission for a single side rARSS processed FS substrate.

The 25 min etch time process was used to fabricate rARSS on both the sides of a FS substrate, to observe the maximum transmission enhancement possible. Figure 13 shows the transmission plot of the substrate with both the sides processed and theoretically possible maximum transmission (100%). Spectral transmission measurements from 300 nm to 2100 nm at normal incidence (0°) were made using a Cary 5000 (Varian) ultraviolet-visible-near-infrared dual-beam grating spectrophotometer. A maximum of 7% transmission enhancement was observed with more than 99% transmission achieved across 500 – 800 nm wavelength region.

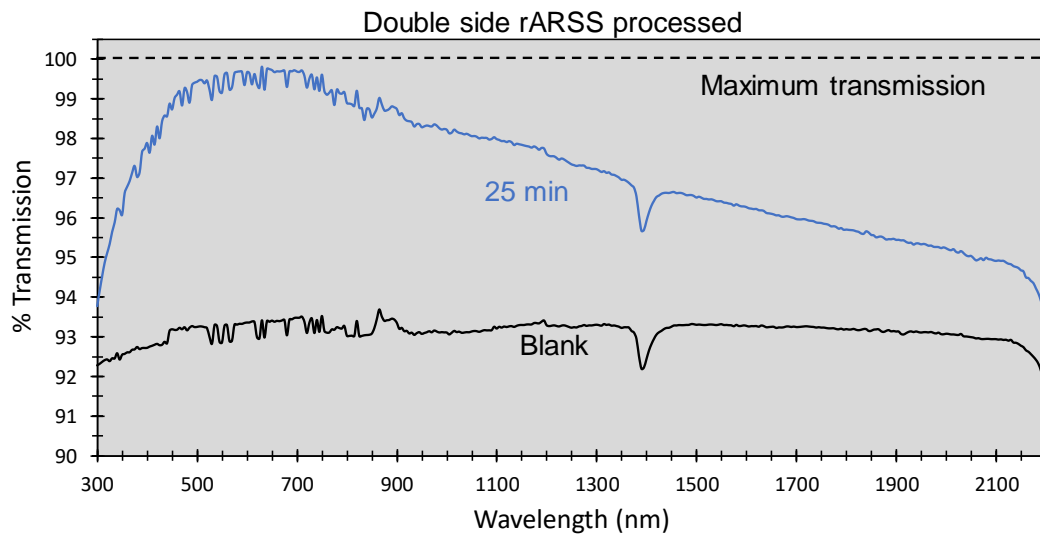


Figure 13: Measured spectral transmission for fused silica substrate with rARSS fabricated on both surfaces of the substrate. Two different samples are shown, an unprocessed (Blank) FS substrate and a 25 min etched sample. The measurements were taken at normal incidence (0°). The black dashed line indicates the theoretically possible maximum transmission.

2.2.5 Scanning electron microscope images and Granulometry

Scanning electron microscope (SEM) images of the rARSS processed FS surfaces were taken using a RAITH150 scanning electron microscope. A representative top-down SEM image of the rARSS processed FS substrates is shown in Figure 14. The random nanostructures were observed across the entire surface of FS substrate.

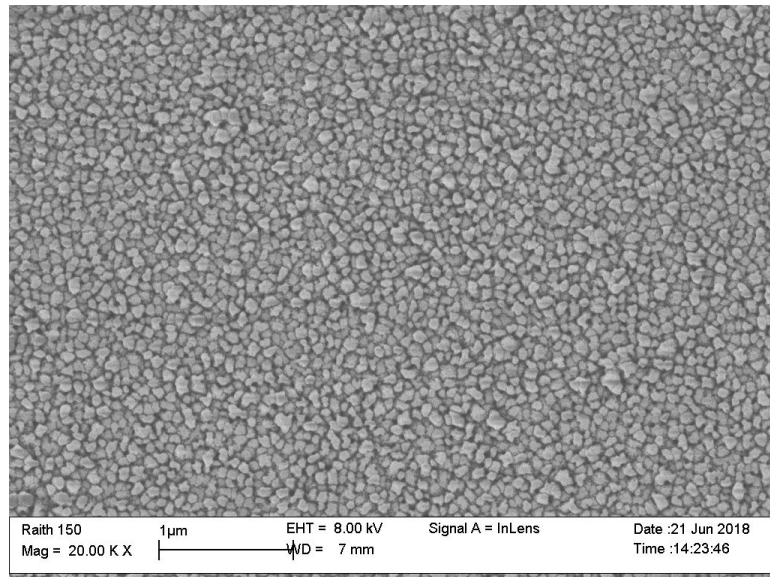


Figure 14: Sample scanning electron micrograph of rARSS fabricated on FS substrate, using a RIE process with a 25min etch time, listed in Table 1.

The top-down SEM images were used to analyze the lateral dimensions of the random structures created on the surface. To quantify the size distribution, granulometry, an image processing technique was used. The program counts the number of different sizes of bright pixel clusters (granules) present in an image, which are called islands, and the dark pixel clusters called voids. With regards to the actual random surface, islands are the fused silica structures, and voids are the empty space (air) in-between those

structures. Both islands and voids are counted separately using gray-scale inversion of the SEM images [23].

The granules used for classification selection were regular octagons, varied from size of 1 to 81 pixels along their diagonal. Each pixel was scaled according to the dimension bar on the SEM image. Figure 15 shows the distribution histogram plot, for the distribution of voids and islands across the SEM image. The plot gives details about the distribution of voids and islands across the SEM image. The plot gives details about the mean diameters of voids and islands present in the image, and the weights of the populations. The mean diameter of the random structures (islands) processed on the FS substrate was observed to be around 55nm. The mean diameter of the islands was more than voids, which means the random structures are of larger size compared to the spacing in-between them.

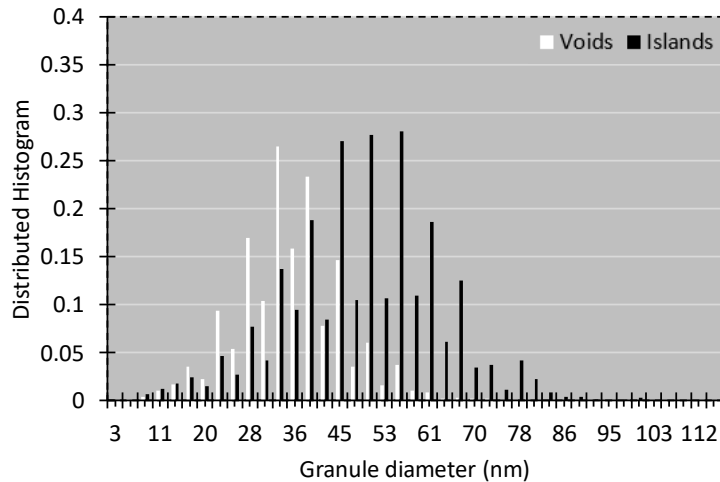


Figure 15: Distributed histograms of the feature sizes corresponding to the SEM micrograph of the random structure on FS substrate shown in Fig. 3. The distribution of islands is represented by the Black bars and the voids by white bars. The total populations are normalized to the total surface area.

Random anti-reflective structures were created on fused silica substrate by gold deposition and reactive-ion etching using the STS AOE tool. Transmission of more than 99% was achieved across 500 – 800 nm wavelength region. The micrographs showed the formation of rARSS with a mean diameter of 55 nm fabricated on the fused silica substrate.

2.3 Cleartran Zinc Sulfide

2.3.1 Introduction

This section focuses on Cleartran ZnS infrared (IR) wavelength range transmissive optical windows, and fabrication of random structures as an AR treatment. Cleartran is a transmission window over a broad range of spectrum from 0.4-12 μm [40]. It has many applications in the IR regime, used with infrared sensor, IR window in aircrafts and, IR spectroscopy [41]. Due to a high refractive index of 2.25, it has a Fresnel reflection of 25% (or 14.5% per surface) across the entire IR region. Reducing Fresnel reflections of Cleartran ZnS by fabricating random structures on its surface and enhancing the transmission in the IR region is presented in this section.

Few reports are available describing fabricated periodic and random structures on Cleartran ZnS acting as AR treatment. Hobbs and Macleod [14] from TelAztec LLC were successful in fabrication of periodic structures (ARSS), with a period of 2.9 μm and height of 3.4 μm , on the substrate using a lithographic mask and subsequent plasma etching. They reported an enhanced transmission of 12% across long-wavelength IR (LWIR) region (8-12 μm) for a single sided substrate. Although no details were provided for the mid-wavelength IR (MWIR), and the diffraction loss (scattering edge due to the periodicity of the structure) was shown to start below 7 μm . Byron Zollars et.al [9] from Nanohmics, Inc. have reported fabrication of random surface structures on ZnS window by a two-step process, that does not use any lithography mask pattern. This was done by initial deposition of amorphous aluminum nitride (AlN) as a buffer layer (20nm) or the actual structure layer (1-5 μm). After that a thin layer (3-30nm) of nickel (Ni) was

evaporated onto the surface. Rapid thermal annealing (RTA) is performed to create sub-micron Ni islands. A dry etching is then followed using a mixture of hydrogen (H_2) and halogen to create a random surface structure either in the AlN layer or through the ZnS substrate depending on the etch time. The last step included removal of excess Ni using aqueous ferric chloride ($FeCl_3$) solution. They were able to achieve a transmission enhancement of around 6-10% for double side etch across the IR region. It must be noted that the index of refraction of AlN is around 2.0 at $3\mu m$ wavelength, and it will play a role in reducing the reflection due to lower refractive index compared to Cleartran ($n=2.25$), acting as an intermix region between air and the substrate. Although both these processes achieved some amount of enhancement, the fabrication process is complicated.

Previous work on creating random structures on Cleartran was reported by Dr. Kevin Major [42], A post-Doctorate fellow working with our group. This was done by irradiating the substrate's surface, using a low power (power $<10mW$) continuous-wave (CW) 325nm-wavelength laser. A raster scanning method was used to irradiate a limited area of the substrate, by focusing the incident laser light to a very small spot and then scanning the spot across the substrate. He was successful in creating random structures by partial ablation and subsequent re-deposition of the irradiating surface. An enhancement in transmission of about 4.5-7 % per single surface was achieved across a wavelength region of 0.6-1.2 μm (Figure 16).

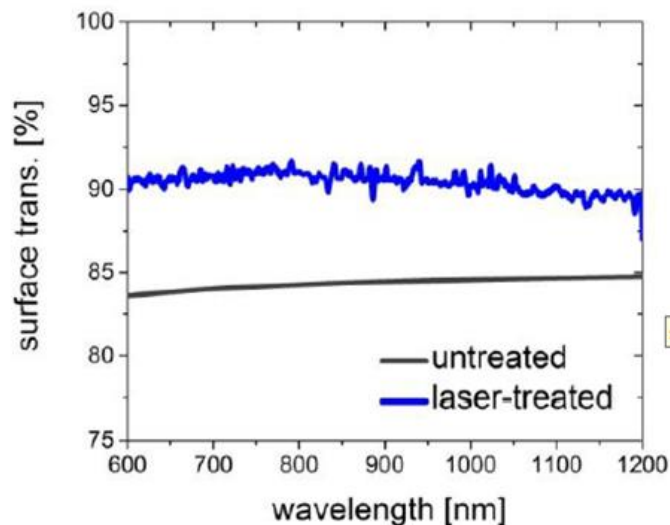


Figure 16: Transmission curve of the enhancement between an untreated and laser ablated Cleartran ZnS using a low power (power < 10mW) CW 325 nm wavelength laser [42].

To achieve enhanced transmission, a very long exposure time (> 30-40min) was required, due to the low power of CW laser. Moreover, the spectral region of interest, from 1 to 10 μm , was not explored with the CW irradiated Cleartran, although Cleartran is extensively used for applications in the MWIR and LWIR wavelength region. EDAX measurement of Cleartran substrate before and after irradiation with CW laser was also reported (Figure 17). A presence of O_2 peak was observed after irradiation, pertaining to formation of Zinc Oxide (ZnO) layer on the surface of the substrate due to oxidation. The refractive index of ZnO is around 2.0, which is in between the refractive index of air ($n=1$) and Cleartran ($n=2.25$) and the transmission of ZnO thin film is reported as being greater than 90% in the visible and near IR wavelength region. The reason for the observed enhanced transmission of the Cleartran might be due to the ZnO interfacial

layer acting as an AR thin film on top of Cleartran substrate and not entirely due to the random structures.

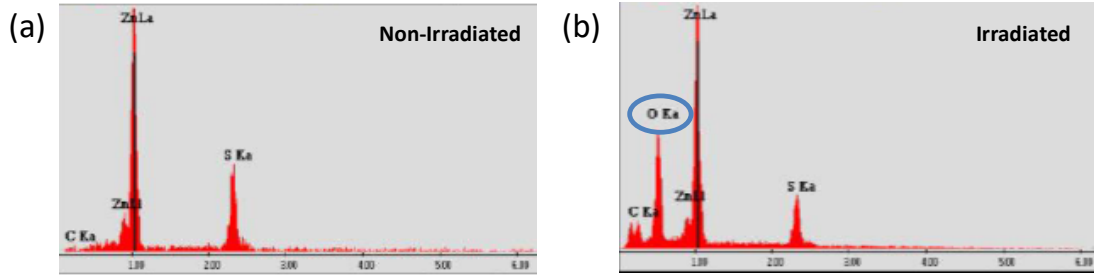


Figure 17: EDAX measurement of the Cleartran substrate (a) before irradiation and (b) after irradiation with a CW laser (Previous OSS lab work) [42].

There are studies referring to surface modification by creating microstructures by irradiation using high power laser pulses. Michael A. Sheehy et. al [43] have shown that $10\mu\text{m}$ tall conical microstructures can be created on silicon (Si) using femtosecond (fs) laser pulses in presence of sulfur as a background gas. They were able to achieve near-unity absorption from $0.25\mu\text{m}$ to $1.1\mu\text{m}$ wavelength range. And Jingtao Zhu et. al [44] have reported micro structuring on Silicon by irradiating with pico-second (ps) and fs laser pulses in SF_6 ambient, but not for the purpose of transmission enhancement. The results showed that the spike formation is different under ps and fs irradiation. This occurs due to the fundamental difference of thermal diffusion and laser ablation dependence on the relaxation time. In case of fs pulses there is a direct solid-vapor transition, while for a ps laser pulse an intermediate molten state is present before the spike formation. Other studies have also shown micro-structuring and nano-structuring on various optical materials, while most of the reported work is for silicon and to increase its absorption [45-49]. However, laser irradiation of infrared optical windows has not

been widely investigated, and no work has been found to-date studying the AR treatment on Cleartran by high power pulsed laser irradiation.

2.3.2 Fabrication of rARSS on Cleartran ZnS

Pulsed laser ablation was used as a fabrication technique in the present effort to create random structures on Cleartran ZnS. Measured transmission (Figure 18) of the Cleartran window shows more than 95% absorption of the incident light for wavelengths shorter than 355nm. Irradiating Cleartran with a high energy pulsed laser, working at 354nm wavelength, should absorb most of the incident energy, leading to localized sputtering and localized re-deposition of the surface material. The resulting surface gets roughened, and a random structure is formed on the substrate.

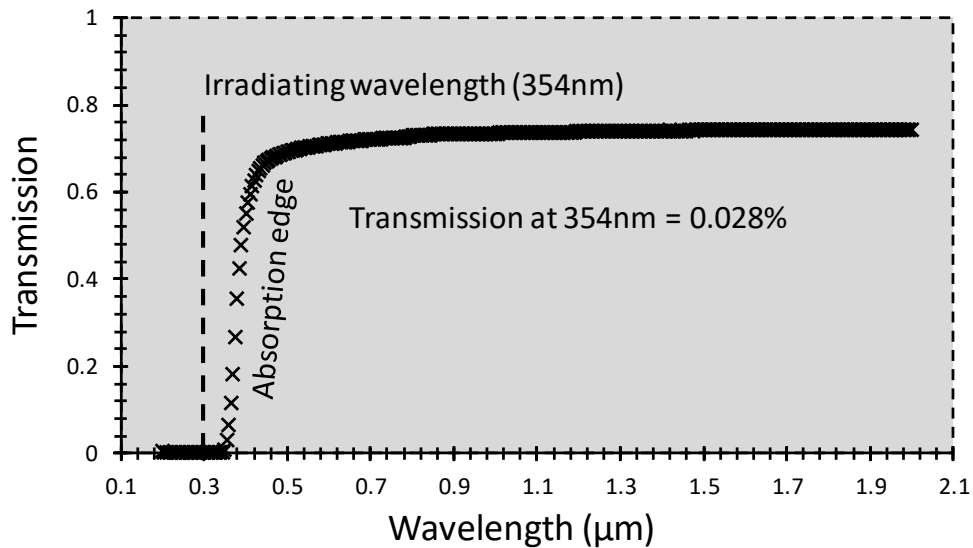


Figure 18: Measured Transmission of an unprocessed Cleartran ZnS sample.

The experimental setup used for ablative irradiation of Cleartran is shown in Figure 19. A high-power Nd: YAG laser, at triple frequency conversion (354 nm), irradiates nanosecond pulses (6 to 9 ns pulse width) onto Cleartran substrate. The energy density of ablation/re-deposition was controlled by the Q-switch time of the laser. A beam of 4.6mm spot diameter was used to illuminate the test samples, through a power sampling mirror placed on an x-y translational stage. A He-Ne laser was used to align the sample and optical components along the beam path. The sampling mirror was used to get a 6-7% of energy from the laser pulse, to monitor real time ablation energy of each pulse.

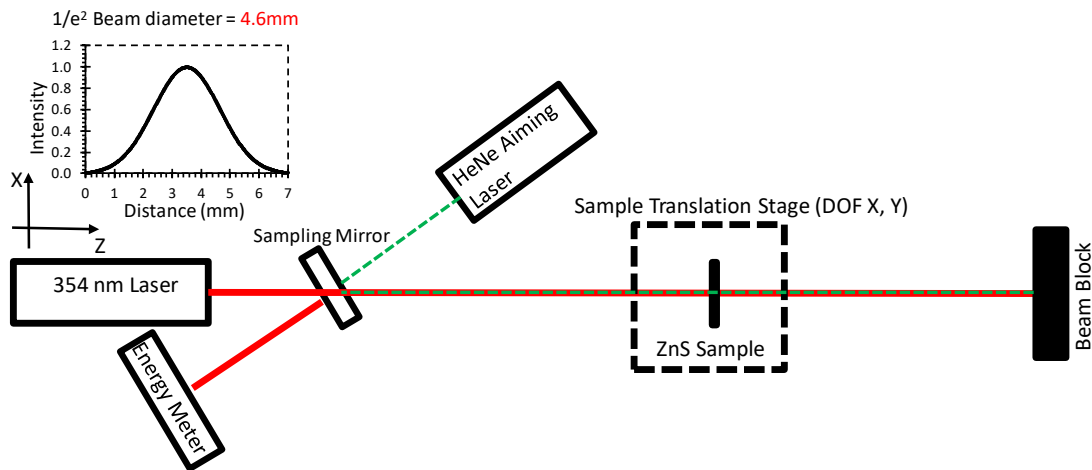


Figure 19: Setup used to create random structures on Cleartran ZnS using nanosecond pulsed High power laser ablative irradiation.

Two variable parameters were used to control the amount of energy of the ablation process. The Q-switch time of the Nd: YAG laser, that gives the amount of energy per pulse, and the number of pulses, that add up to the total irradiation energy on the substrate. These two parameters were used to control the structure parameter of the

random surface created. In order to have an estimate of the ablated energy, the energy output of the laser was measured using a photodetector by varying the Q-switch time and measuring the intensity of one single pulse (Figure 20). This gave a range of ablation energies varying from 10mJ to 200mJ per each pulse.

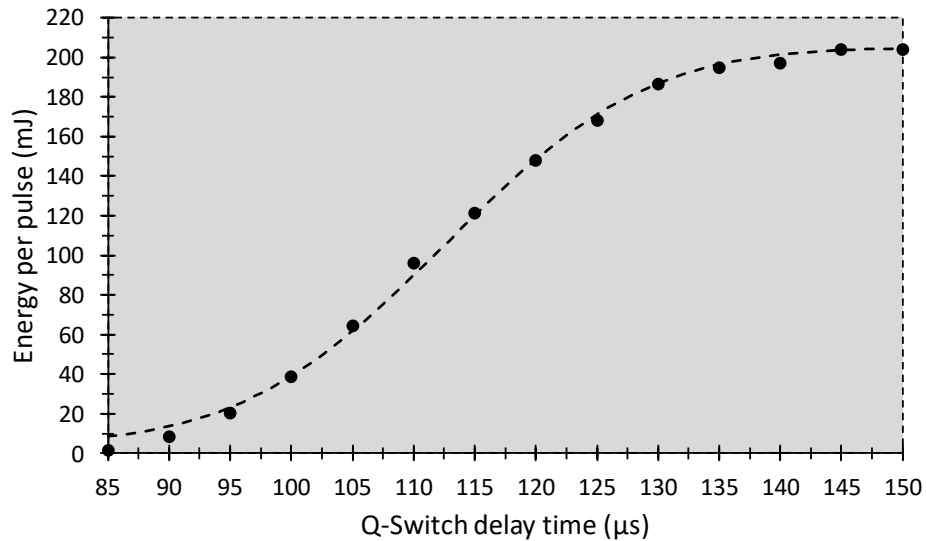


Figure 20: Energy of incident pulse with varying Q-Switch delay time of the Nd: YAG laser used to irradiated Cleartran ZnS.

The structure height-parameter of the random surface was determined by measuring the height of the structure, which was achieved using a UV confocal microscope. This is discussed in the section below. The lateral dimension of the random structures was determined by granulometry, where the image is obtained by SEM of the ablated surface as previously discussed in section 2.2.5.

2.3.3 Surface analysis and confocal microscopy of rARSS on Cleartran ZnS

Initial tests of substrates irradiated at $120\mu\text{s}$ Q-switch time with a total of 3 pulses from the laser, were observed under a microscope. Two microscope images of the surface before and after irradiation are shown in Figure 21. The results from the images indicate that the surface has changed due to ablation and re-deposition, at least as far as the roughness is concerned.

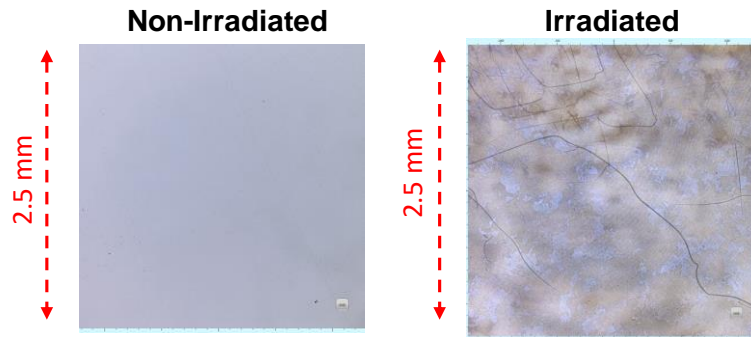


Figure 21: Microscope images of an unprocessed Cleartran (left) and after irradiation using laser ablation (right).

EDAX is a technique used to find the compounds and molecular composition present in a substrate using X-rays. The measurement provides surface analysis of the irradiated substrate, to identify any contamination, or oxidation due to sputtering and localized re-deposition due to ablation. EDAX measurement (Figure 22) of the Cleartran irradiated with Nd: YAG showed that the surface does not have any ZnO formation after irradiation (Figure 22(b)). It is important to identify any formation of ZnO on the surface of the substrate, as it will affect the enhancement in transmission, acting as a thin film dielectric layer with lower index of refraction between Cleartran and air.

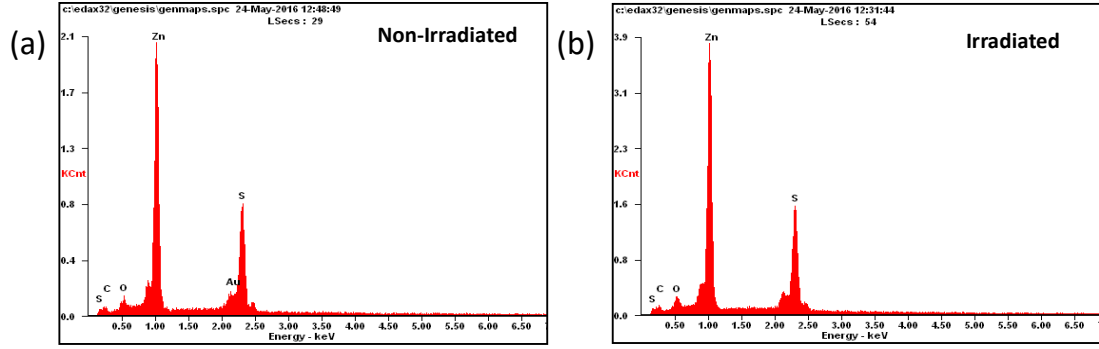


Figure 22: EDAX measurement of the Cleartran substrate (a) before irradiation and (b) after irradiation with a Nd: YAG laser.

Cleartran substrates were irradiated with laser pulses at several Q switch times from 90 – 150 μs . The incidence pulse(s) have a beam width diameter of 4.6mm, allowing the calculation of the amount of energy density (mJ/cm^2), which is irradiation energy for each pulse divided by the irradiated area on the substrate. The energy density (u) was varied from 30 – 960 mJ/cm^2 per pulse, and the number of pulses were varied from 1 to 30. The net irradiation energy is given by, where m is the number of pulses:

$$u_{Net} = (u_{per\ pulse})(m) \quad (7)$$

Roughness measurements were carried on the irradiated regions using a UV confocal microscope (OLYMPUS OLS4000). Two roughness quantities, R_z (given by Equation 5) and R_q (given by Equation 6), were measured. The maximum roughness was plotted as a function of increasing irradiation energy density (Figure 23). It was observed that the maximum roughness increased with increasing the u_{Net} (Figure 23(a)), corresponding to a possible control parameter of the amount of roughness created on the substrate. Plotting the max roughness with respect to irradiation energy per pulse (Figure 23(b)) showed that an energy threshold occurs at $300\text{mJ}/\text{cm}^2$, before which no

roughness was observed on the substrate's surface. It was also observed that for a specific number of pulses the maximum roughness remained unchanged with varying energy density from 350 – 950 mJ/cm². This observation leads to a tentative conclusion that maximum roughness is controlled with the number of pulses, but remains constant for specific pulse numbers.

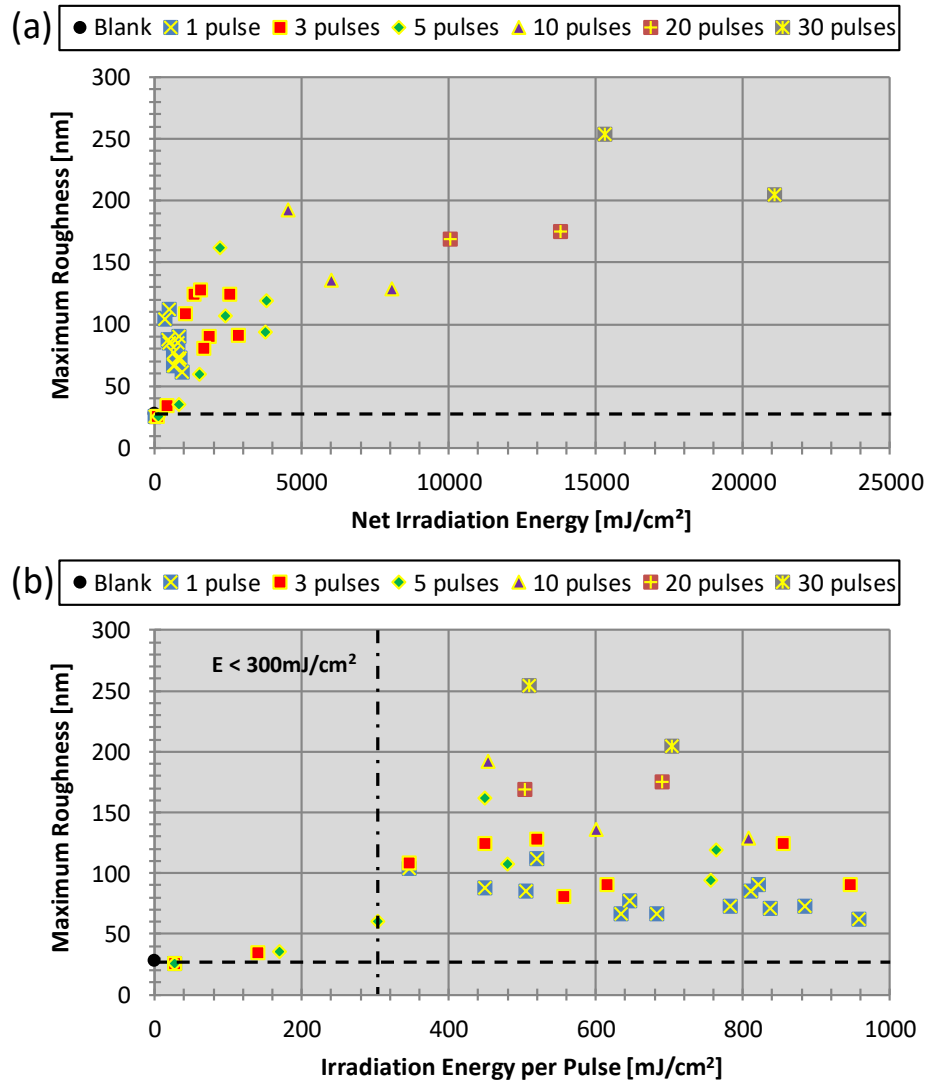


Figure 23: Maximum roughness as a function of (a) Net irradiation energy and (b) Irradiation energy per pulse. The number of pulses in both the plots have been specified using different markers. The dashed line represents the roughness of the non-irradiated Cleartran substrate.

To see if this effect pertained over the whole surface, the RMS roughness was plotted versus varying irradiation energy (Figure 24). A similar effect was observed with an increased roughness by increasing the number of pulses. The roughness remained same per pulse over the test energy density.

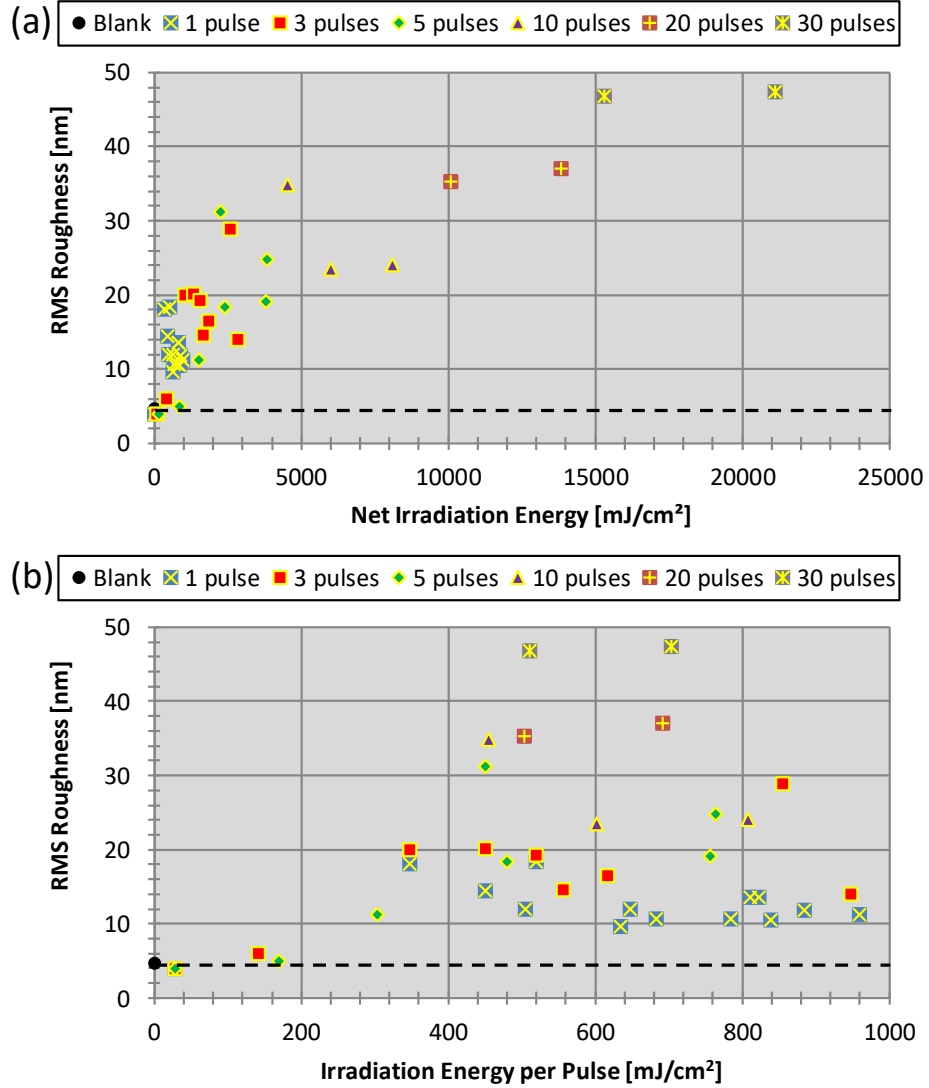


Figure 24: RMS roughness as a function of (a) Net irradiation energy and (b) Irradiation energy per pulse. The number of pulses in both the plots have been specified using different markers. The dashed line represents the roughness of the non-irradiated Cleartran substrate.

In order to identify the cause of the roughness variation, all roughness values for specific pulse numbers were averaged irrespective of the irradiation energy. Figure 25 shows the averaged roughness values as a function of number of irradiation pulses. A definite increase in the maximum and RMS roughness were observed with increasing number of pulses. These observations assisted in identifying the amount of irradiation energy required to achieve a certain structured pattern height.

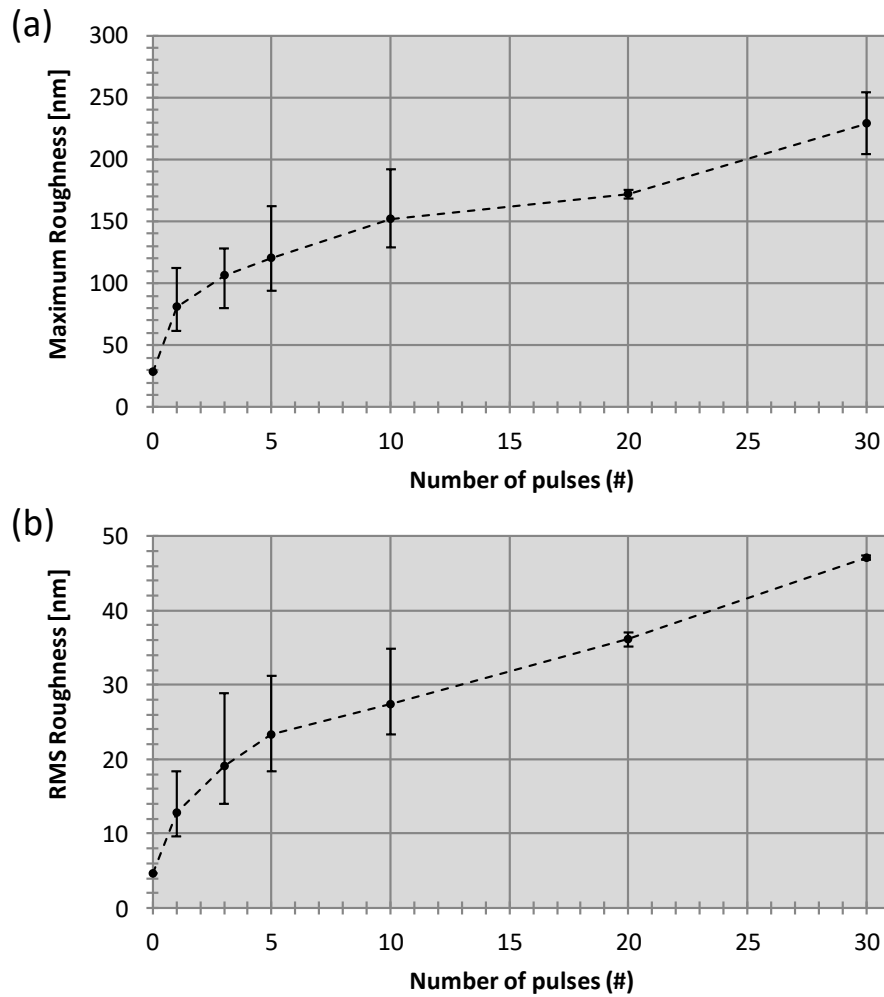


Figure 25: (a) Maximum roughness and (b) RMS roughness as a function of number of irradiation pulses. The bars represent the maximum and minimum value of the measured roughness for a specific pulse number.

To examine the dependence between maximum and rms roughness with varying irradiation energy, the ratio of R_q over R_z was calculated. This ratio is called stratification ratio, and can vary from 0 to 1, where 1 is the limit for all structures on the surface to be same in height (Homogeneous surface).

Figure 26 shows the variation of stratification ratio with changing net and per pulse irradiation energy density. No large variations in the stratification ratio were observed, due to the similar trend between R_q and R_z roughness observed in Figure 25. It was noted that the roughness variations achieved by irradiating the substrate was not uniform across the whole ablated region, due to the gaussian irradiation beam profile, with higher intensity at the center compared to the beam periphery.

It is possible to create random structures on Cleartran ZnS by irradiation using a high-power UV pulsed laser. The net irradiation energy was controlled using varying Q-switch delay time and the number of irradiation pulse. The EDAX results have shown no oxidation on the substrate due to irradiation in atmosphere, leaving no contaminations on the surface. Controlling the amount of roughness (structure height) can be explored by varying the amount of net irradiation energy. A minimum threshold energy was required to achieve a rough surface, after which the roughness increased linearly with the number of irradiation pulses. The rms and maximum roughness have shown similar trends resulting in a constant stratification ratio for varying irradiation energy.

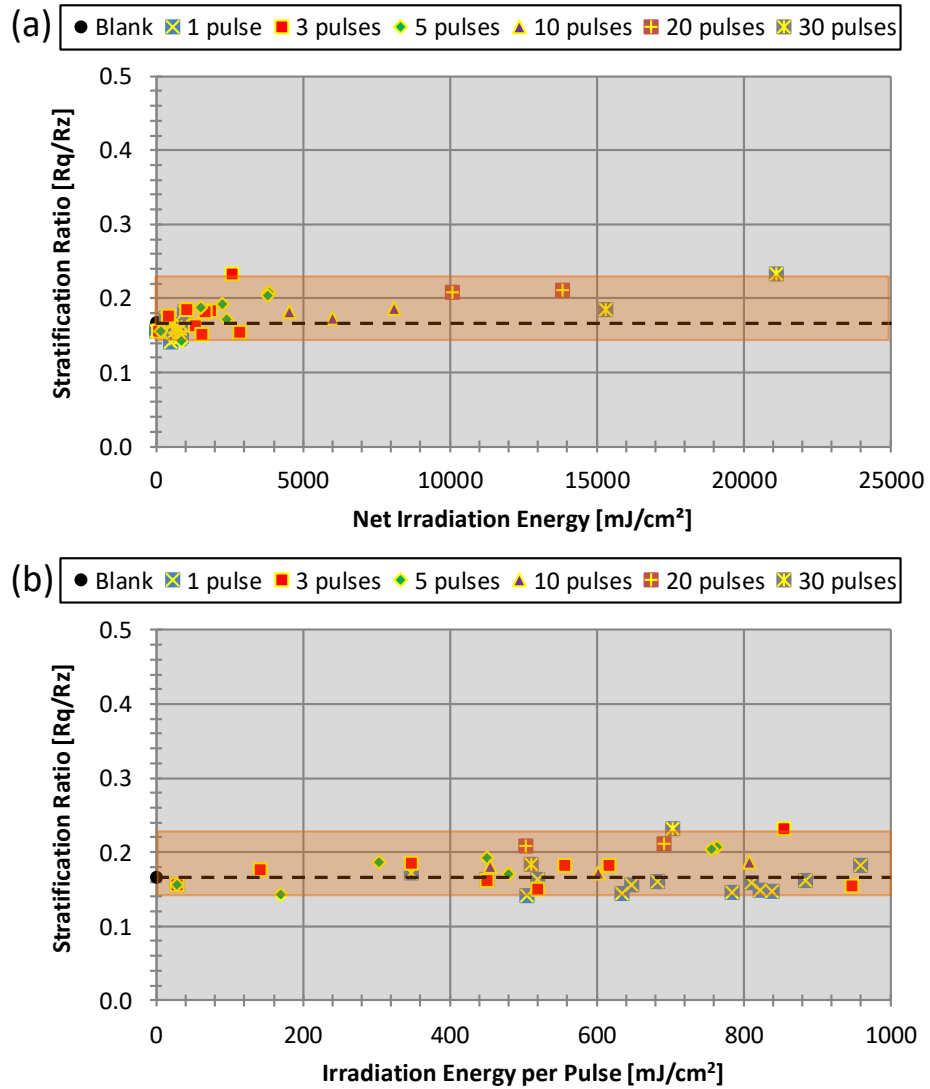


Figure 26: Stratification ratio as a function of (a) Net irradiation energy and (b) Irradiation energy per pulse. The number of pulses in both the plots have been specified using different markers. The dashed line represents the roughness of the non-irradiated Cleartran substrate.

2.3.4 Optical Performance of rARSS on Cleartran ZnS in Mid-IR Spectral region

Optical transmission measurements were conducted on the irradiated Cleartran substrates. A Fourier-transform infrared (FTIR) spectrometer was used to measure the transmission of Cleartran in the MWIR spectral region. Transmission of a non-irradiated substrate was also measured to compare with the irradiated substrate. Figure 27 shows the transmission plot at normal incidence (0°) of the Cleartran substrate with the maximum enhancement achieved. The graph represents transmission through a single surface of Cleartran (considering reflection from only one of the substrate's surfaces) across the 3-10 μm wavelength range.

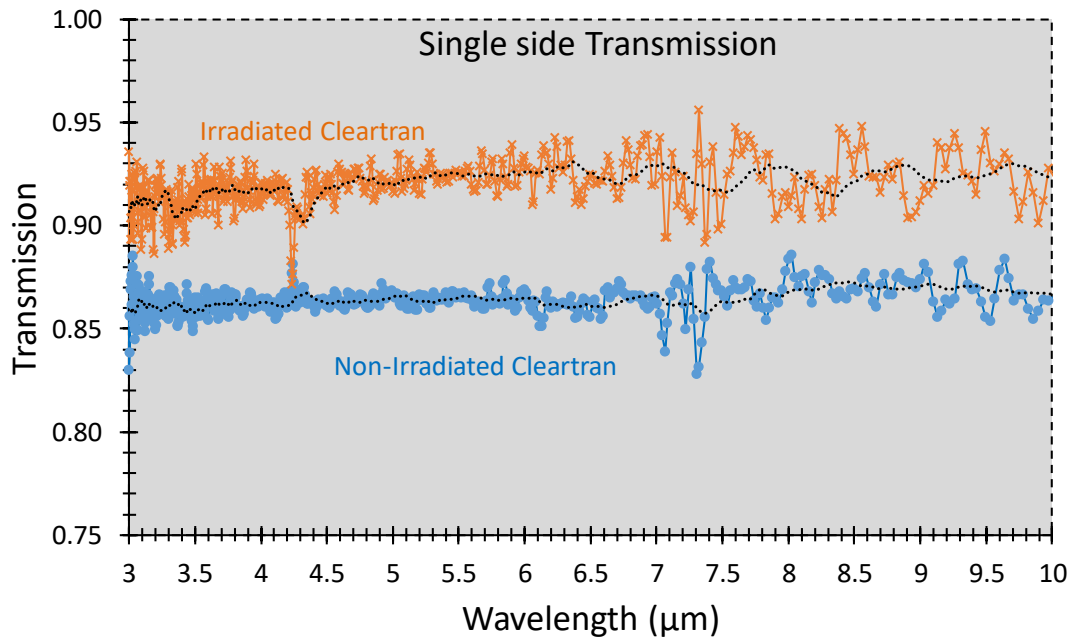


Figure 27: Measured single side transmission, at 0° AOI, vs wavelength (μm) for a non-irradiated Cleartran and Cleartran with rARSS on one surface, fabricated using laser irradiation and re-deposition. The black dotted line represents the moving average trendline for each curve.

The irradiated sample gave an enhancement in the transmission by 7% across the MWIR region. The measurements indicate that the random structured surface formed by the irradiation and re-deposition technique using a high power pulsed laser resulted in an enhanced transmission across the wavelength region of interest. It must be noted that this was the maximum enhancement we were able to generate by the ablation technique, although Cleartran has a Fresnel's reflection of 14.5% in the MWIR wavelength region for one surface. This was achieved for 10 pulses with irradiation energy density per pulse of 602 mJ/cm^2 .

2.3.5 Scanning electron microscope images and Granulometry

To quantify the structure's lateral dimensions, SEM image of the irradiated surface is analyzed using granulometry. Figure 28 is a SEM image of the Cleartran surface which shows the difference between the irradiated (B) and non-irradiated (A) area on the surface. This is clear indication of random structure formation on Cleartran.

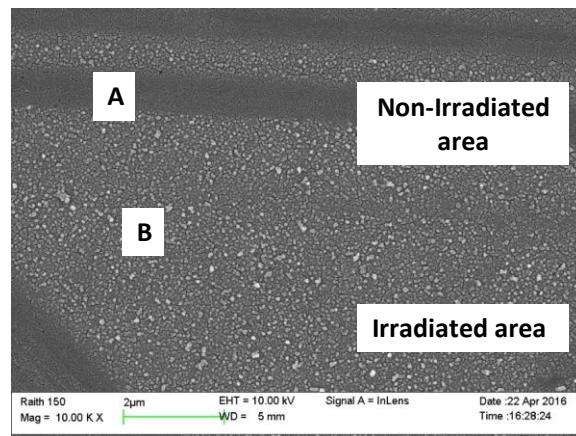


Figure 28: SEM image of an rARSS structure on Cleartran ZnS, fabricated using Laser irradiation.

To understand how the structure's lateral dimensions, vary with the net irradiation energy, three samples were analyzed using granulometry. Table 2 gives the details about these three samples. The energy density per pulse was similar for all three samples and the number of pulses were varied from 1 to 10. As shown earlier, increasing the net irradiation energy increases the height of the structure (Table 2). Sample "A" with 10 irradiation pulses had the maximum measured structure height. These three samples were analyzed to observe the effect of lateral structure dimensions to the increase in number of irradiation pulses.

Table 2: Energy density and structure height values of three samples with similar irradiation per pulse energy and different number of irradiation pulses.

Sample	Energy density per pulse (mJ/cm²)	# Pulses	Total irradiation energy (mJ/cm²)	R_z (nm)
A	602	10	6017	135
B	616	3	1848	90
C	635	1	635	66

Figure 29 shows sampled SEM images using the RAITH150, from the three samples along with the normalized histogram plots for each image. The SEM images show that the structures were formed on all three samples with energy density around 600mJ/cm² per pulse.

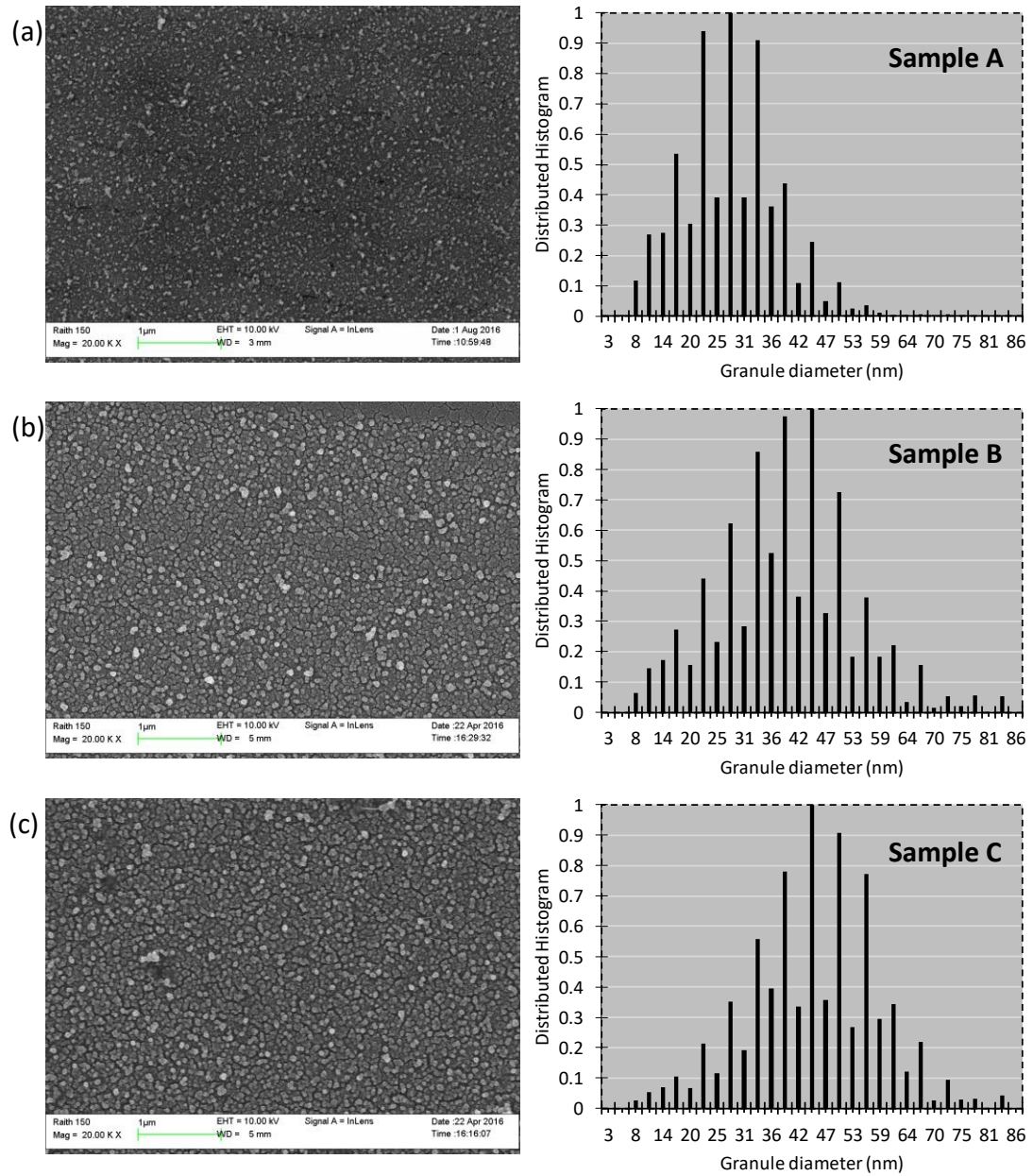


Figure 29: Scanning electron micrographs and lateral feature size distribution histograms of irradiated Cleartran substrate with (a) 10 pulses, (b) 3 pulses and (c) 1 pulse using a high-energy pulsed laser at 354nm. The average energy density per pulse was around 600mJ/cm².

Granulometry was used to analyze the size distributions of the granules (random structures). Granules used for classification were regular octagons, which were varied

from size of 1 to 61 pixels along their diagonal. Each pixel was scaled according to the dimension bar on the SEM image. The distribution histogram plots show the distribution of islands across the SEM image. The plots give details about the mean diameters of the granules present in the image. A difference in the granule diameter was observed for the three samples. Samples “B” and “C” with 1 and 3 pulses have a mean granule diameter of 45nm, while sample “A”, with 10 pulses has a mean granule diameter of 25nm.

The reduced granule diameter by increasing the number of pulses can be understood due to ballistic collisions of the high energy pulses on the surface, leading to sputtering and redeposition of the material. A transmission enhancement of 7%, shown earlier in Figure 27, was for Sample “A” with a structure height of 135nm and a mean granule diameter of 25nm, which indicates tall random structure with small granule diameters. While the 10 pulses gave an enhanced transmission, increasing the pulses further to 20 and 30 did not give any enhancement. Moreover, other samples with 10 pulses, with an energy density of around 450 and 800 mJ/cm² per pulse did not show any enhancement either. This could be modelled as a simple harmonic oscillator system, interacting with incident pulses. The structural modification using nanosecond (ns) laser pulses is thermal ablation in nature, unlike the femtosecond (fs) laser, which is a non-thermal process [50, 51]. For a ns laser, the surface goes through a molten state (liquid phase) before the structure is formed [44, 52]. Considering the simple pendulum’s rest state as the sample’s non-irradiated surface, when the sample is hit with the first pulse, it goes into an excited state (higher energy). Now the incident arrival of the second pulse will define if the structure formed has an additive or averaging effect. If the pendulum experiences an external force along the direction of motion of the oscillation, it increases

velocity. If the force is experienced in the opposite direction of motion of the oscillation, it reduces velocity. Similarly, it depends on when the other pulses are arriving at the sample and whether the irradiated spot is in the molten state or it has reached equilibrium (solid state). It is difficult to deduce if all pulses have a positive effect in creating the structure pattern, without a high-power precision shutter and accurate control on the time difference between the pulses.

2.4 Summary

This chapter presented results from two different fabrication methods of rARSS applied to fused silica and Cleartran zinc sulfide. In section 2.2, a fabrication technique to create rARSS on FS was investigated. The process involved a deposition of thin layer of Au (20nm) to act as a partial discontinuous mask, followed by etching the Au sputtered substrate using an STS AOE etcher, in a mixture of SF₆ and O₂ plasma. It was observed that varying the etch time resulted in an increased transmission enhancement in the visible (400 – 800 nm) spectral region. Maximum transmission of greater than 99% was achieved from 500 – 800 nm spectral region for a double side processed FS substrate. Scanning electron micrographs of the etched surface showed the formation of random structures across the whole substrate and granulometry of the images gave a mean structure lateral dimension of around 55nm. Overall, the etching technique created rARSS on FS substrate.

The work outlined in section 2.3 included investigating a new fabrication technique for the fabrication of rARSS on IR optical windows. The initial results have

shown that roughness can be created by irradiating the Cleartran ZnS substrate with high power pulsed laser. And the EDAX results have shown that no contaminations have been formed due to oxidation like ZnO. Detailed analysis of the roughness of the surface, as a function of net irradiation energy, has shown that increasing the energy density will result in a higher structure height. Comparing the results with energy density per pulse has shown that the roughness remains same for a particular pulse number with energy density varying from 350 – 950 mJ/cm². The stratification ratio remained unchanged over varied energy density due to similar trends of R_z and R_q. A maximum enhancement of 7% in the transmission was observed across the MWIR (3 - 10 μm) spectral region, for a single surface irradiation. The random structured surfaces formed through the irradiation and re-deposition triggered by high power pulsed laser, and formed an anti-reflective treatment on Cleartran surface. The confocal microscopy gave the random surface structure height value of 135nm and the granulometry of the random surface has shown the structure lateral dimensions to be around 25nm. Overall, the irradiation technique successfully created rARSS on Cleartran ZnS [53]. This fabrication technique is fundamentally different from the plasma etching process used with fused silica.

CHAPTER 3: RANDOM ANTI-REFLECTION STRUCTURED SURFACES ON BINARY DIFFRACTION GRATINGS

3.1 Introduction

Chapter 2 presented the optical performance of rARSS on fused silica and ZnS flat optical windows. A number of studies are available in the literature on fabrication and testing of these structures on optical flats. Light travelling through any optical component, such as a diffraction grating will have Fresnel reflections at the interface. Quantifying the optical performance of flat substrates is different compared to diffraction gratings. Transmission measurements from flat substrates is confined to a single propagating beam direction, while the incident beam through a diffraction grating separates the angular spectrum into several orders, and each of these propagating orders must be examined. As mentioned in Chapter 1, using a thin film coating as an AR treatment is quite possible and has been accomplished by different methods, but the coating should be considered as part of the grating design prior to the fabrication of the grating itself. Deposition of AR thin films on pre-fabricated (commercially available) gratings using conformal layered deposition would change the diffractive properties of the grating by perturbing the duty cycle of the original diffraction grating and a non-uniform, non-conformal vapor deposition would change the relative phase depth resulting in variation of diffraction order efficiency. Fabrication of random structures to act as an AR treatment on already existing diffraction gratings would expand the applications of rARSS.

This chapter focuses on characterizing the optical performance of near-wavelength binary fused silica gratings, with rARSS previously optimized for application onto flat fused silica substrates. Two commercially available transmission gratings were used to investigate the rARSS effects on diffraction gratings.

Because this chapter focuses on the optical performance of rARSS on diffraction gratings, it is important to thoroughly discuss any similar studies in the literature, of which there are a few. A group from MIT, Chih-Hao Chang et. al. successfully fabricated tapered (cone-shaped) subwavelength nanostructures, integrated on the surface of a microscale diffractive grating. The fabrication consisted of the realization of the nanostructures, followed by the grating profile implementation, on a silicon substrate. While they have achieved a very low reflection loss with periodic patterns on top of the gratings, the fabrication process included photoresist spin coating, etching (masking using lithography), followed by mask removal for the subwavelength nanostructures, then a repetition of the fabrication cycle in order to fabricate the diffractive grating itself [34]. In the wavelength range they tested the surface, silicon absorbs all the transmitted orders, which makes the elements unsuitable for transmission applications, whereas it can be used as an absorption element. Xin Ye et. al. fabricated AR structures on 3 μm period fused silica grating and showed a total reduced reflection of 7.5 to 4.5% [54]. The work reported did not include any specific details regarding the grating such as the phase depth or the measurement details. And no data was shown on the efficiency of the individual orders.

Figure 30 shows the geometrical relation between the incident light, and the grating interface parameters. When light of a specific wavelength travels across the

grating boundary, it separates the angular spectrum of various orders (m) to different propagation direction wavevectors (k_m). This is valid on both the reflection (Figure 1(a)) and transmission (Figure 1(b)) side of the grating. The number of orders, and the angular spread of the orders, is described by the diffraction grating equation (Equation 1 and 2). Where n_1 and n_2 represent the index of refraction of the incident medium and the transmitted medium. The equation shows that for light incident with a wavelength λ , on a periodic surface with period Λ , at an incidence angle of θ_i , the incident light separates an angular spectrum of various orders m , which satisfy the equation (m being an integer). The propagating orders travel at an angle of θ_m with respect to the grating normal, in the plane of incidence. The propagating transmission orders obey Equation 8, while the propagating reflection orders obey Equation 9.

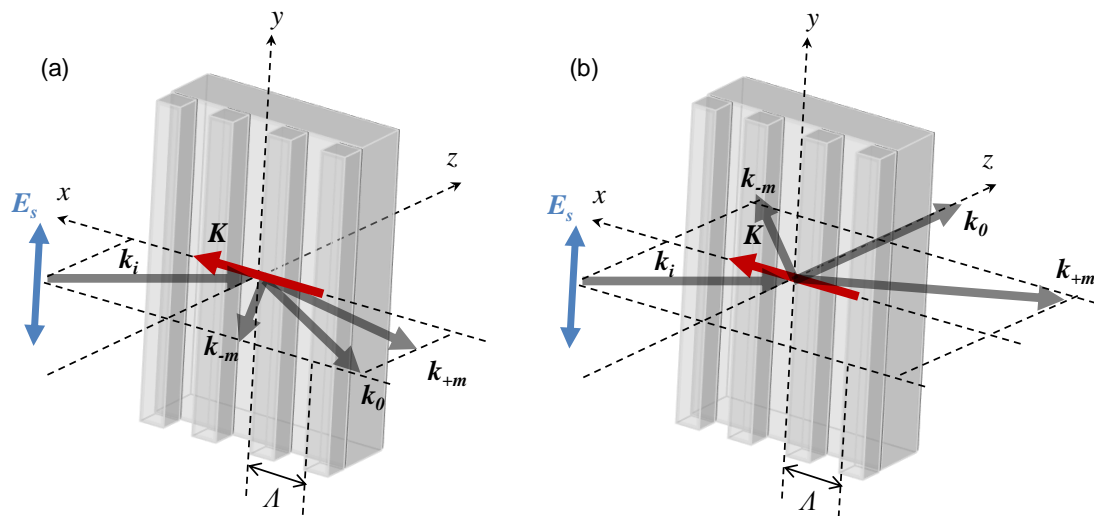


Figure 30: General depiction of the various orders of the angular spectrum, for a binary diffraction grating on (a) reflection and (b) in transmission, due to the diffractive grating surface.

$$n_1 \sin \theta_m - n_2 \sin \theta_i = m\lambda/\Lambda \quad (8)$$

$$n_1 \sin \theta_m + n_1 \sin \theta_i = m\lambda/\Lambda \quad (9)$$

Section 3.2 will present results from the fabrication of rARSS on both sides of the binary fused silica diffraction gratings, as well as, the scanning electron micrographs which show the differences in the surface of the grating post-and pre-rARSS fabrication. The cross-sectional micrographs show a clear formation of the random nanostructures on the surface of the grating.

Section 3.3 presents the characterization of the random nanostructures' optical performance. A detailed comparison is included, to determine any performance variations due to the presence of the rARSS on the surface of the gratings. The propagating diffracted order angles and, individual reflection and transmission diffraction efficiencies of all orders were measured, first on the original gratings (unprocessed) and then on the rARSS enhanced gratings. The intensity profile of the propagating diffracted beams was measured, to quantify any effects after rARSS fabrication. The work presented here includes measurements at three incident wavelengths (594nm, 612nm and 633nm), three angles of incidence (normal, 1st Bragg and 2nd Bragg) and, both S and P polarization states. To conclude this section, the surface was characterized using granulometry, to obtain a statistical distribution of the lateral feature sizes of the rARSS. This was done to

observe if any differences were present, between the structural size of the rARSS in the grooves (bottom) and the top of the grating surface.

Section 3.4 investigates the performance of the gratings at a varied angle of incidence from 0° to 70° , to determine how the random profile will affect the gratings optical performance for AOI greater than 40° . A measurable enhancement of around 20-30% was observed for the total summed transmission of all the propagating orders at 612 nm for S polarized incident light. This effect was observed for both $1.595\mu\text{m}$ and $1.166\mu\text{m}$ period gratings.

Section 3.5 presents the comparison of performance of the gratings at a varied angle of incidence for, the unprocessed grating, a perfect single-layered anti-reflective (SLAR) grating and rARSS processed grating.

Finally, section 3.6 summarizes the results from the previous sections and draws final conclusions about the optical performance of pre-fabricated diffraction gratings processed with rARSS.

3.2 Fabrication of rARSS on binary diffraction gratings

3.2.1 Fabrication process

Two commercially available, uncoated, linear, binary phase, fused silica gratings, with periods of $1.595\pm 0.050\mu\text{m}$ (fill factor = 0.5; depth = 700nm) and $1.166\pm 0.050\mu\text{m}$ (fill factor = 0.55; depth = 600nm), were processed to fabricate rARSS on their planar

surfaces, including the substrate's planar backside. Both gratings were cleaned prior to processing, by immersion into methanol for 10-15 min and drying using forced nitrogen gas. The fabrication process involved the deposition of a thin discontinuous layer of gold (<20nm) as a partial mask using an AJA international ATC 1800-F sputter deposition system. The discontinuous gold film is used to initialize the random etch process. A reactive-ion plasma etching step followed in PlasmaTherm RIE 7000, using a mixture of 35 sccm SF₆ and 5 sccm O₂ gas plasma with a platen power of 700W and a chamber pressure of 24mT. The planar backside was etched initially, along with a witness sample for 40 minutes, to verify the process effectiveness for a fused silica window. The process was repeated for the grating structure with the same etch parameters as that for the planar backside along with the opposite side of the witness sample. X-ray scattering measurements (EDAX) of the surface post-processing, showed that no gold remained on the surface after the plasma etch was completed. There was no attempt to customize the process to the grating topography in any way, as we chose to investigate any adverse effects to the grating's performance due to process-induced profile changes.

To inspect the effectiveness of the etching process, transmission of the fused silica witness flat was measured at 5 different test wavelengths (543nm, 594nm, 604nm, 612nm and 633nm). Figure 31 shows the measured transmission intensity values of the unprocessed (original), single side processed, and double side processed witness flat. A 3-3.5% enhancement was measured after a single side etch, and a similar enhancement was observed after etching both sides of the witness flat, resulting in >99% transmission across the test wavelength region.

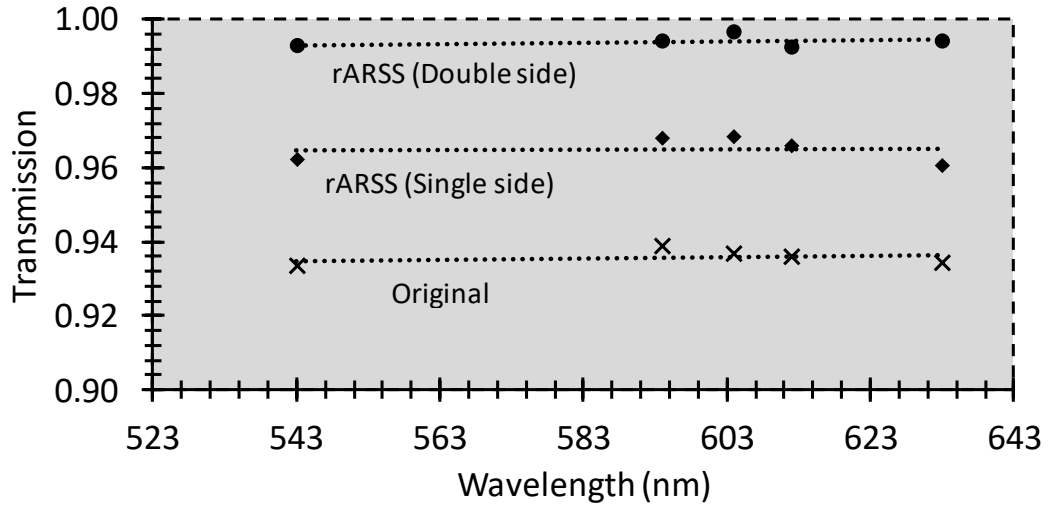


Figure 31: Measured transmission intensity of the fused silica witness flat across the test wavelength for unprocessed (original), single side processed, and double side processed.

3.2.2 Scanning electron microscope images

Scanning electron microscope (SEM) images of the unprocessed and rARSS processed diffraction grating surface were taken using a RAITH150 scanning electron microscope. Top-down SEM images of the original unprocessed fused silica gratings and the rARSS processed gratings, are shown in Figure 32. The random nanostructures were observed on the entire surface of both gratings imaged (Figure 32(c,d)). We measured the period and duty cycle, and confirmed that it was unchanged after the rARSS fabrication process, within our measurement's uncertainty limits ($\pm 5\text{nm}$). To compare the height of the random structures on the top and bottom of the grating grooves, both gratings were edge-diced, to image the cross-sectional view of the random nanostructures on the grating surfaces. Figure 33 (a,c) shows a sample tilted cross-sectional view of the surface of the gratings with rARSS. There is clear identification of structure formation on the top and

bottom of the grating grooves. It was also observed that no structures were formed on the sidewalls of the grating, and that the sidewalls remained near-vertical, which can be seen in the cross-sectional SEM images (Figure 33 (a and c)).

Figure 33 (b,d) are cross-sectional sample images, used to measure the average height of the nanostructures. For the larger period grating (1.595 μm), the average structure height on the top surface was 267 nm and the bottom (trench) was 287 nm. For the smaller period grating (1.166 μm), the average structure height on the top surface was 204 nm and the bottom (trench) was 211 nm. Small protruding features were observed at the grating groove edges, in the SEM images (Figure 33 (b,d)), more predominant on the 1.166 μm period grating. These features were not present prior to the rARSS fabrication, and therefore were classified as process defects. The defects appear as a single columnar feature, with an average diameter of 40nm, and are restricted to the side-edge boundary of the binary phase step. As such, it could have an effect on the gratings diffraction order efficiencies, or some scatter contribution. The feature size is well subwavelength in scale for our tests, which are conducted between 594nm and 633nm. Nonetheless, we tested all possible measurable effects, such as, the perturbation of the grating periodicity, all propagating diffraction-order efficiencies in reflection and transmission, the total overall reflected and transmitted diffraction efficiency, using three test wavelengths, both incident polarization states and, three incident beam mounting angles, as well as, the propagating diffracted order beam profiles before and after the fabrication process.

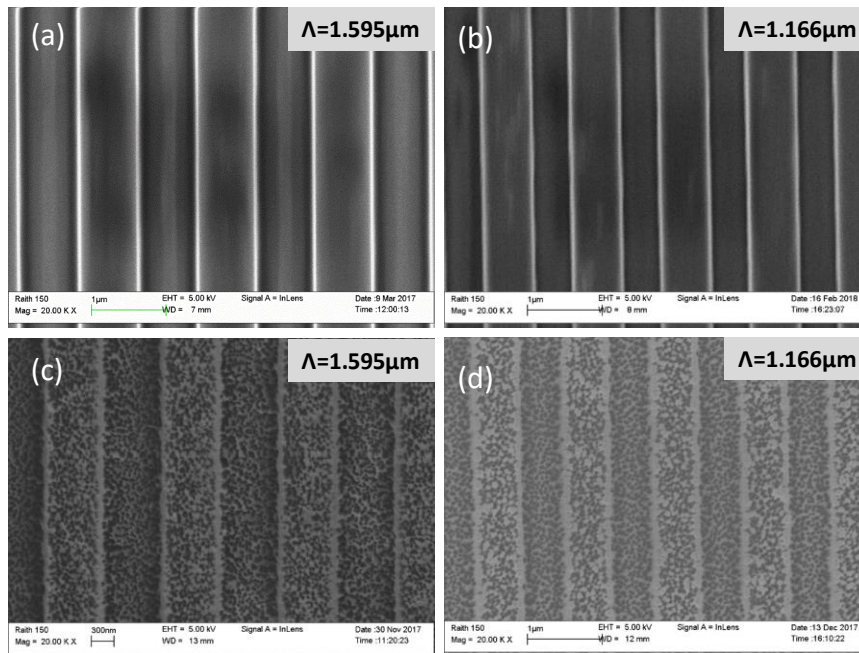


Figure 32: Top-down scanning electron micrographs of commercially available linear binary fused silica gratings with periods of: (a) $1.595\mu\text{m}$ and (b) $1.166\mu\text{m}$. Micrographs of rARSS fabricated on the gratings with the respective periods above (c, d).

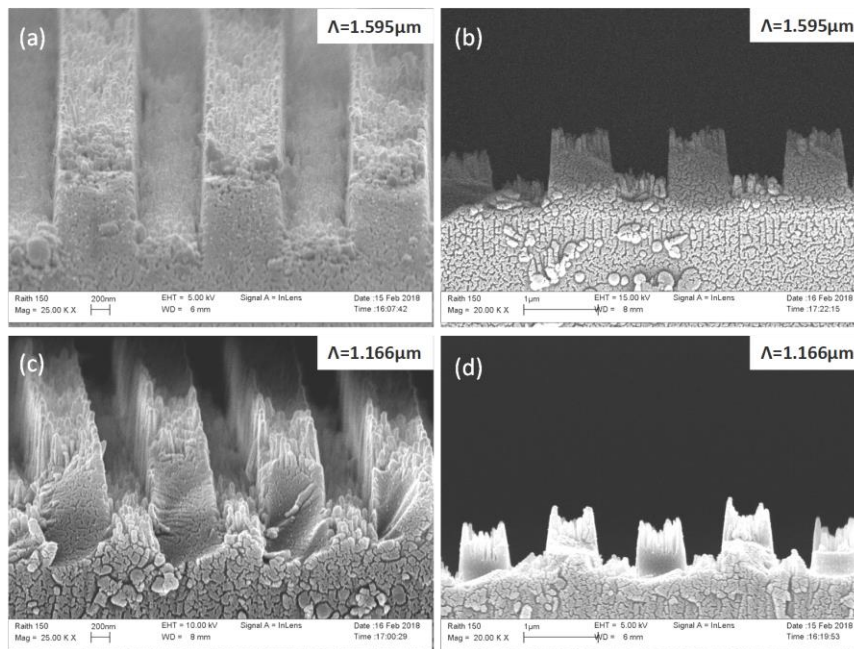


Figure 33: Scanning electron microscope (a, c) tilted cross-sections and, (b, d) side-view cross-sections of rARSS fabricated on top of the gratings with periods of: (a, b) $1.595\mu\text{m}$ and (c, d) $1.166\mu\text{m}$.

3.3 Experimental setup and Optical performance testing

3.3.1 Experimental test setup

The experimental test setup to measure the grating's optical performance is shown in Figure 34. Incident light from a He-Ne laser was passed through a beam splitter on to a half-wave-plate (HWP), which was used to control the polarization of the incident light from S to P, and then through a linear polarizer towards the test grating. A standard silicon photodiode power sensor (S120C THORLABS) was mounted on a rotating table and was used to measure the diffraction efficiency and the angle of diffraction of the all propagating diffraction orders. A spectrometer was used on the other side of the beam splitter to verify the wavelength selection for each test.

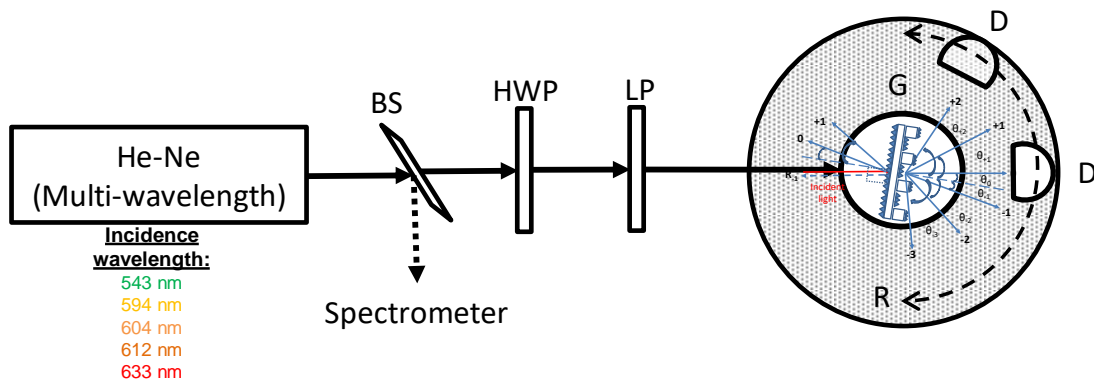


Figure 34: Experimental layout for measurement of diffraction efficiencies of all orders for the grating under test (G), using the detector (D) placed on a rotating stage (R). Polarization of incident light is controlled by rotating a half-wave plate (HWP) and a linear polarizer (LP).

Using this setup, a detailed comparison was done to determine any performance variations due to the presence of the rARSS on the surface of the gratings. The propagating diffracted order angles and, individual reflection and transmission diffraction efficiencies of all orders were measured, first on the original gratings (unprocessed) and then the same measurements were repeated after fabrication of rARSS on the surface of the gratings. The work presented here includes measurements at three incident wavelengths (594nm, 612nm and 633nm), three angles of incidence (normal, 1st Bragg and 2nd Bragg) and, both S and P polarization states.

Figure 35 shows the alignment and the angular spread of the gratings at the test angles of incidence.

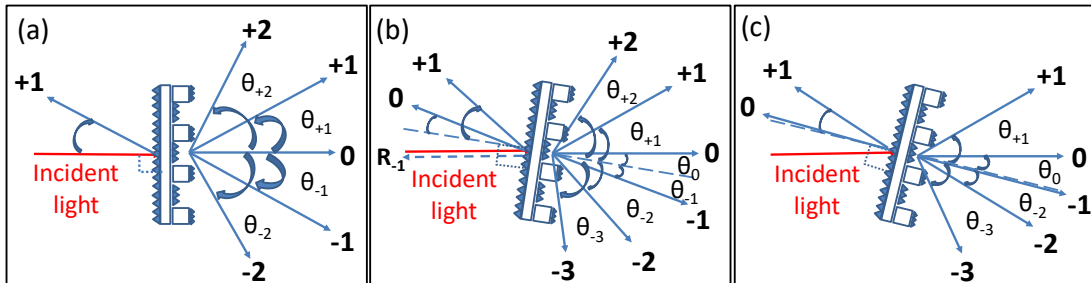


Figure 35: Angle of incidence test setup for all gratings tested. (a) The grating is aligned at Normal incidence. (b) The grating is aligned at 1st Bragg angle of incidence, where the “-1st” reflected order goes back in the direction of the incident light. (c) The grating is aligned at 2nd Bragg angle of incidence, where the “0th” reflected order is aligned along the normal to the grating plane.

The Bragg incidence angle depends on the wavelength of the incident light according to Equation (10,11):

$$\theta_{1st\ Bragg} = \sin^{-1} \frac{\lambda}{2\Lambda} \quad (10)$$

$$\theta_{2nd\ Bragg} = \sin^{-1} \frac{\lambda}{\Lambda} \quad (11)$$

At normal incidence the incidence angle is aligned to the grating normal (Figure 35(a)). At 1st Bragg incidence the “-1” reflected order traces back into the incident light direction (Figure 35(b)) and at 2nd Bragg incidence the “0th” reflected order is aligned with the normal to the grating (Figure 35(c)). The calculated values of 1st and 2nd Bragg incidence for both the gratings are in Table 3.

Table 3: Calculated 1st and 2nd Bragg angle of incidence in degrees for 1.595µm and 1.166µm period gratings.

λ	1.595 µm		1.166 µm	
	1 st Bragg	2 nd Bragg	1 st Bragg	2 nd Bragg
594nm	10.73°	21.86°	14.75°	30.63°
612nm	11.06°	22.56°	15.21°	31.66°
633nm	11.45°	23.38°	15.75°	32.88°

Having measurable tilt orientations, based on the diffraction order locations for each configuration, allowed us to consistently align the gratings and further identify the measured diffraction order intensities without ambiguity.

3.3.2 Measurement of diffraction order angular separation

Diffraction angles were measured for the unprocessed and the rARSS processed gratings for both S and P polarization. The angle of diffraction (θ_m) depends on the period of the grating (Λ) for a particular incident wavelength and incidence angle (θ_i) (Equation 12). Any perturbation of the grating's period will have a measurable effect on the diffraction angles of higher orders.

$$\sin \theta_m = n_2 \sin \theta_i + m\lambda/\Lambda \quad (12)$$

We measured and compared the diffraction angles pre-and-post processing to verify that the grating period was not in any way affected by the random-etch process on the diffraction gratings.

Diffraction angles of all propagating orders were measured pre-and-post rARSS etching, for both S and P polarizations at all three wavelengths (594 nm, 612 nm and 633 nm). The angular spread was measured at normal incidence, 1st Bragg incidence and 2nd Bragg incidence as mentioned in Table 4.

Table 4: Measured 1st and 2nd Bragg angle of incidence in degrees for 1.595 μ m and 1.166 μ m period gratings

λ	1.595 μ m		1.166 μ m	
	1 st Bragg	2 nd Bragg	1 st Bragg	2 nd Bragg
594nm	11.0° \pm 0.5°	22.5° \pm 0.5°	14.5° \pm 0.5°	30.5° \pm 0.5°
612nm	11.5° \pm 0.5°	23.0° \pm 0.5°	15.0° \pm 0.5°	31.5° \pm 0.5°
633nm	11.5° \pm 0.5°	24.0° \pm 0.5°	15.5° \pm 0.5°	32.5° \pm 0.5°

The measured diffraction angles of all propagating orders were unaffected by the addition of rARSS, for both S and P polarizations, at normal, 1st Bragg and, 2nd Bragg incidence angles. Similar results were observed for all test wavelengths, confirming that the period of the original grating was not affected by the rARSS fabrication process, or the presence of the edge defect, and validating the measurements made by the SEM micrographs.

The measurements have been tabulated in Tables 5 and 6 according to angle of incidence (normal, 1st Bragg and 2nd Bragg), for each test wavelength and at each incidence angle. The propagating order diffraction angles of both S and P polarizations is listed as a single column for the original (Blank) and the rARSS gratings, since no deviation of the angles was observed for either period grating.

Table 5: Measured diffraction angles of the 1.595 μm period grating, for all propagating orders of the pre-processed original (Blank) and the post-processed rARSS gratings, at 594nm, 612nm and 633nm, for three angles of incidence.

Normal	Measured (rARSS and Blank)			1 st Bragg	Measured (rARSS and Blank)			2 nd Bragg	Measured (rARSS and Blank)		
	594nm (S/P)	612nm (S/P)	633nm (S/P)		594nm (S/P)	612nm (S/P)	633nm (S/P)		594nm (S/P)	612nm (S/P)	633nm (S/P)
θ_{+2}	48.0	50.0	52.0	θ_{+2}	68.5	73.5	83.5	-	-	-	-
θ_{+1}	22.0	22.5	23.5	θ_{+1}	34.0	35.5	36.5	θ_{+1}	49.0	51.0	53.5
θ_0	0.0	0.0	0.0	θ_0	11.0	11.5	11.5	θ_0	22.5	23.0	24.0
θ_{-1}	-22.0	-23.0	-23.5	θ_{-1}	-11.0	-11.0	-11.5	θ_{-1}	0.0	0.0	0.0
θ_{-2}	-48.5	-50.5	-53.0	θ_{-2}	-34.0	-35.0	-37.0	θ_{-2}	-22.0	-22.5	-23.5
-	-	-	-	θ_{-3}	-69.0	-73.5	-81.0	θ_{-3}	-48.0	-50.0	-52.0

Table 6: Measured diffraction angles of the 1.166 μm period grating, for all propagating orders of the pre-processed original (Blank) and the post-processed rARSS gratings, at 594nm, 612nm and 633nm, for three angles of incidence.

Normal	Measured (rARSS and Blank)			1 st Bragg	Measured (rARSS and Blank)			2 nd Bragg	Measured (rARSS and Blank)		
	594nm (S/P)	612nm (S/P)	633nm (S/P)		594nm (S/P)	612nm (S/P)	633nm (S/P)		594nm (S/P)	612nm (S/P)	633nm (S/P)
θ_{+1}	29.5	30.5	32.0	θ_{+1}	48.0	50.0	52.5	-	-	-	-
θ_0	0.0	0.0	0.0	θ_0	14.5	15.0	15.5	θ_0	30.5	31.5	32.5
θ_{-1}	-30.0	-31.0	-32.0	θ_{-1}	-14.5	-15.0	-15.5	θ_{-1}	0.0	0.0	0.0
-	-	-	-	θ_{-2}	-48.5	-50.5	-53.0	θ_{-2}	-30.0	-30.5	-32.5
-	-	-	-	-	-	-	-	θ_{-3}	-78.5	-	-

3.3.3 Simulated diffraction order angular separation and efficiencies

To verify the measured diffracted angle results of the unprocessed gratings, we simulated each grating using VirtualLab Fusion software [55]. The simulated results of the unprocessed (Blank) grating were compared to the measured values (Table 5 and 6), for all test incidence angles at the three test wavelengths within the uncertainty of our measurement ($\pm 0.5^\circ$). The simulations have been tabulated in Tables 7 and 8 according to angle of incidence (normal, 1st Bragg and 2nd Bragg), for each test wavelength. Good agreement was observed between the simulated and measured diffraction order angular spread.

Table 7: Simulated diffraction angles of the 1.595 μm period grating, for all propagating orders of the pre-processed original (Blank) grating, at 594nm, 612nm and 633nm, for three angles of incidence.

Normal	Simulated			1 st Bragg	Simulated			2 nd Bragg	Simulated		
	(Blank)				(Blank)				(Blank)		
	594nm (S/P)	612nm (S/P)	633nm (S/P)		594nm (S/P)	612nm (S/P)	633nm (S/P)		594nm (S/P)	612nm (S/P)	633nm (S/P)
θ_{+2}	48.1	50.1	52.5	θ_{+2}	69.5	75.4	83.7	-	-	-	-
θ_{+1}	21.9	22.6	23.4	θ_{+1}	34.3	35.7	36.7	θ_{+1}	49.2	50.9	53.7
θ_0	0.0	0.0	0.0	θ_0	11.1	11.6	11.6	θ_0	22.6	23.1	24.1
θ_{-1}	-21.9	-22.6	-23.4	θ_{-1}	-10.4	-10.5	-11.3	θ_{-1}	0.7	0.5	0.7
θ_{-2}	-48.1	-50.1	-52.5	θ_{-2}	-33.6	-34.5	-36.4	θ_{-2}	-21.1	-22.0	-22.6
-	-	-	-	θ_{-3}	-67.7	-71.8	-81.8	θ_{-3}	-47.0	-49.3	-51.4

Table 8: Simulated diffraction angles of the 1.166 μm period grating, for all propagating orders of the pre-processed original (Blank) grating, at 594nm, 612nm and 633nm, for three angles of incidence.

Normal	Simulated (Blank)			1 st Bragg	Simulated (Blank)			2 nd Bragg	Simulated (Blank)		
	594nm	612nm	633nm		594nm	612nm	633nm		594nm	612nm	633nm
	(S/P)	(S/P)	(S/P)		(S/P)	(S/P)	(S/P)		(S/P)	(S/P)	(S/P)
θ_{+1}	30.0	31.1	32.2	θ_{+1}	49.2	51.2	53.7	-	-	-	-
θ_0	0.0	0.0	0.0	θ_0	14.8	15.3	15.8	θ_0	30.8	31.8	33.0
θ_{-1}	-30.0	-31.1	-32.2	θ_{-1}	-14.2	-14.6	-15.1	θ_{-1}	0.7	0.7	0.7
-	-	-	-	θ_{-2}	-48.2	-50.2	-52.6	θ_{-2}	-29.3	-30.3	-31.5
-	-	-	-	-	-	-	-	θ_{-3}	-81.8	-	-

To observe the trend in the ratio of efficiency of the diffracted orders as a function of incidence angle, the simulated gratings in VirtualLab Fusion software were used to plot the diffraction efficiency of individual orders with respect to the incidence angle (Figure 36). The design was operated at 594 nm and S polarization.

For 1.595 μm period grating (Figure 36(a)), at normal incidence there were 5 propagating diffraction orders, with equal 1st- order efficiencies ($\eta_{\pm 1}$). At 1st Bragg incidence η_{-1} was observed to be higher than η_{+1} and, there were 6 transmitted propagating diffraction orders. At 2nd Bragg incidence the +2 order becomes evanescent and η_{-1} was observed to be higher than η_{+1} . And for 1.166 μm period grating (Figure 36(b)), at normal incidence there were 3 propagating diffraction orders, with equal 1st- order efficiencies ($\eta_{\pm 1}$). At 1st Bragg incidence η_{+1} was observed to be higher than η_{-1} and,

there were 4 transmitted propagating diffraction orders. At 2nd Bragg incidence the +1 order becomes evanescent and η_{-1} was observed to be the highest.

Similar trend was observed for diffraction order efficiencies at 612 nm and 633 nm for both the gratings (Not shown in figure). The calculated results indicate that the tilted grating orientation will impact the diffraction efficiencies of the ± 1 orders and, the number of propagating orders.

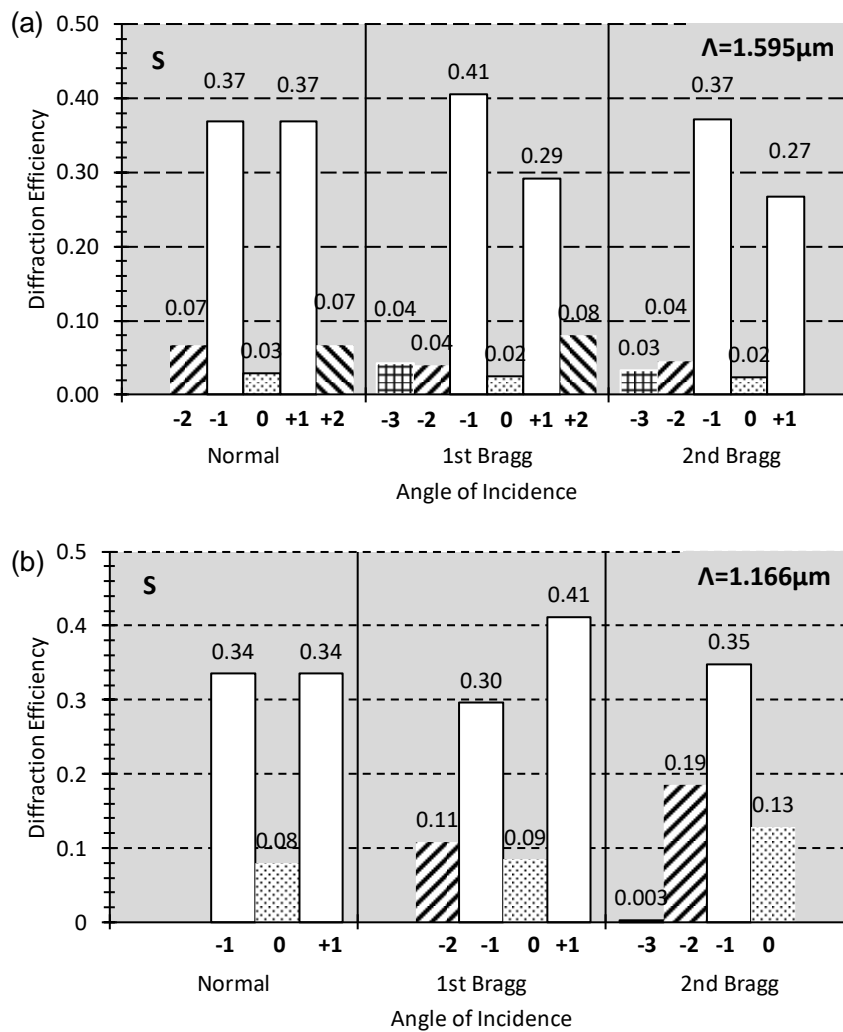


Figure 36: Simulated Transmission diffraction efficiencies of all orders for (a) 1.595 μm and (b) 1.166 μm period gratings at 594nm and S polarization grouped by angle of Incidence.

3.3.4 Diffraction Efficiency measurements

In order to verify that Fresnel reflectivity was suppressed by the rARSS fabrication, the reflected diffraction efficiencies were measured prior and post-application of the random structures. The measured reflection efficiencies of the original and the rARSS processed gratings were compared for zeroth-order (0^{th}) and positive-first-order ($+1^{\text{st}}$) (Figure 37). The measurements were carried out at all three test wavelengths and incidence angles. For the $1.595\mu\text{m}$ period grating (Figure 37(a,b)), at 2^{nd} Bragg incidence, the reflected efficiency for $+1^{\text{st}}$ order has reduced considerably from about 7% to 1% on average. Similar results show at 1^{st} Bragg incidence for 0^{th} order, the reflection efficiency reduced from 9% to 0.5% for the fabricated rARSS enhanced grating surface. For the $1.166\mu\text{m}$ period grating (Figure 37(c,d)), at 2^{nd} Bragg incidence, the reflected efficiency for $+1^{\text{st}}$ order has reduced considerably from about 15% to 6% on average. Similar results show at 1^{st} Bragg angular incidence, the reflection efficiency of the 0^{th} order reduced from 10% to 1% for the rARSS enhanced grating surface. On average after the fabrication of rARSS structures the grating reflection efficiencies reduced to about 1-2% from 7-14%.

Fresnel reflection loss per surface for planar fused silica averages around 3.5% at 633 nm wavelength, and an ideal AR coating on the planar side of the grating substrates would have reduced the reflection loss by that amount. We note that the reflection loss has reduced by a considerable amount from 7-8% for both the gratings. This must be due to the reflectance suppression on both sides of the grating substrates, due to the presence of rARSS structures on both surfaces.

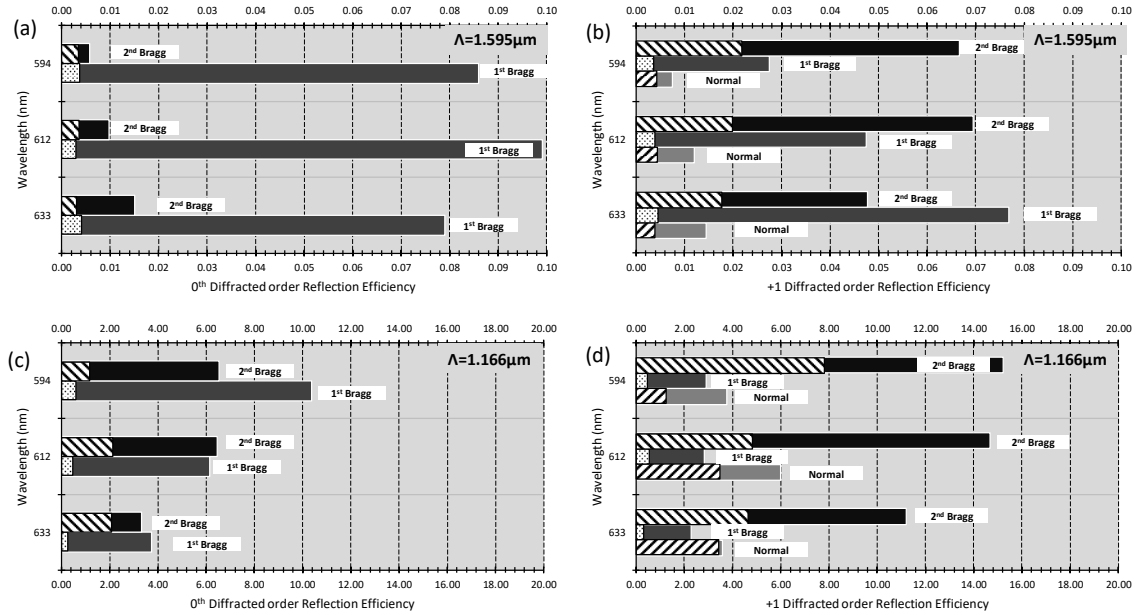


Figure 37: Measured reflection diffraction efficiencies of (a) 1.595 μm 0th order, (b) 1.595 μm +1st order, (c) 1.166 μm 0th order and (d) 1.166 μm +1st order for normal, 1st Bragg and, 2nd Bragg angles of incidence at 594 nm, 612 nm and 633 nm. Solid bars represent the original grating measurements, while the patterned bars show the same grating post-processed measurement with rARSS.

The reduction in reflected diffraction efficiency should result in the transmission enhancement and not lost to surface induced scatter. To confirm this, a comparison between the measured total transmission diffraction efficiency for both the unprocessed (original) and rARSS fused silica grating was made.

Table 9 and 10 show the comparison data for both gratings. Efficiency of all propagating transmission orders were summed, to get the total transmission by the gratings (Equation 13). Measurements shown include, all test wavelengths (594nm, 612nm and 633nm) and the three test angles of incidence: normal, 1st Bragg and 2nd Bragg; and both incident polarizations of light. An enhancement was verified for total transmission in all test cases for both period gratings. Enhancement for S polarized light

was maximum and, was around 7% for 1.595 μ m period grating and 10% for 1.166 μ m period grating at all test incidence angles.

$$\eta_{Total} = \sum_{m=-l}^{+q} \eta_m = \dots + \eta_{+1} + \eta_0 + \eta_{-1} + \eta_{-2} + \dots \quad (13)$$

Where q is the highest propagating positive order and l is the highest propagating negative order.

Table 9: Comparison between total transmission intensity of all propagating orders for the original (blank) and rARSS grating, for various angle of incidence at 594 nm, 612 nm and 633 nm, for the 1.595 μ m period grating.

λ	Blank	rARSS	Blank	rARSS
	Normal (S)		Normal (P)	
594 nm	95.61	97.66	93.55	97.81
612 nm	95.00	99.00	91.15	97.61
633 nm	90.00	96.00	92.35	97.62
	1 st Bragg (S)		1 st Bragg (P)	
594 nm	92.31	97.54	94.97	97.25
612 nm	87.70	99.80	96.10	99.20
633 nm	84.83	94.70	92.88	95.77
	2 nd Bragg (S)		2 nd Bragg (P)	
594 nm	87.31	91.38	86.46	92.97
612 nm	85.68	92.30	90.81	96.67
633 nm	83.70	92.61	95.55	96.14

Table 10: Comparison between total transmission intensity of all propagating orders for the original (Blank) and rARSS grating, for various angles of incidence at 594 nm, 612 nm and 633 nm, for the 1.166 μ m period grating.

λ	Blank	rARSS	Blank	rARSS
	Normal (S)		Normal (P)	
594 nm	73.1	81.1	82.1	82.6
612 nm	73.4	88.5	87.0	86.2
633 nm	76.6	84.7	85.6	91.1
	1 st Bragg (S)		1 st Bragg (P)	
594 nm	87.7	95.4	92.3	96.6
612 nm	91.0	97.3	95.3	98.4
633 nm	89.7	96.7	95.3	97.8
	2 nd Bragg (S)		2 nd Bragg (P)	
594 nm	75.8	78.8	73.0	80.2
612 nm	70.3	88.1	74.1	81.1
633 nm	71.5	82.6	72.5	84.5

The reduction in reflected diffraction efficiency has resulted in the enhancement of the total diffracted propagating order transmittance, which confirms that the reflectance suppression was not lost due to surface induced scatter.

In order to verify the reduced reflected diffraction efficiency by the rARSS, the individual transmission diffraction efficiencies were measured, and summed them up to get a total propagated transmission intensity, prior and post-application of the random structures. To quantify the amount of scattering loss, the total propagated transmission intensity of all orders was added to the amount of reflected intensities from -1, 0, +1

orders and subtracted the result from the total incident intensity. An average scatter loss was calculated for all test wavelengths and AOI. This gave an average intensity loss of 5.16% for 1.595 μ m period grating and 2.23% for 1.166 μ m period grating. It must be noted that the intensity loss includes the total scattering from surface and reflection intensity of higher orders (-3, -2 and +2). Considering from simulations that the intensity of higher reflection orders sums up to around 2-3%, the total scattering loss for 1.595 μ m grating would be less than 2% and for 1.166 μ m grating will be less than 0.5%. The results verify that no substantial scattering losses were observed, on both directions, as the average lateral dimension of the random structures fabricated by our process, was measured to be between 30 nm and 60 nm (Section 3.3.6). This scale is ten to twenty-times smaller than the test wavelengths (594nm, 612nm and 633nm) used, contributing to measurable scatter effects for wavelengths shorter than 300nm.

To verify the transmittance of each individual diffraction order at different test angles of incidence, intensity measurements made pre-and-post etch are plotted in Figure 9 below for the 1.595 μ m period grating and Figure 10 for the 1.166 μ m period grating.

For 1.595 μ m period grating, the equal efficiency η_{+1} and η_{-1} order intensities at normal incidence, changed to an unbalanced efficiency ratio after the fabrication of the rARSS on the grating surface, even though the total transmission from all the orders combined was higher post-process (Figure 38(a-d)). This trend was observed for all three wavelengths and both polarizations.

At 1st Bragg angle of incidence, which is also the Littrow reflection angle, the unprocessed grating simulations indicated unequal $\eta_{\pm 1}$ diffraction efficiencies (Figure

36(a)). We measured the $\eta_{\pm 1}$ order intensities for the unprocessed grating and found them in agreement with the simulations. Post-rARSS application, the grating intensities of $\eta_{\pm 1}$ orders were measured to be nearly equal. This was observed at all three test wavelengths and both polarizations. The reduced reflection has resulted in an enhancement of $\eta_{\pm 2}$ orders (Figure 38(a₁-d₁)).

For 2nd Bragg angle of incidence, the unprocessed grating simulations indicated unequal $\eta_{\pm 1}$ diffraction efficiencies along with +2 becoming evanescent (Figure 36(a)). We measured the $\eta_{\pm 1}$ order intensities for the unprocessed grating and found them in agreement with the simulations efficiencies along with +2 becoming evanescent. The intensity weight of the $\eta_{\pm 1}$ orders reversed after etching. We observe high enhancement in the η_{-2} order for the processed grating, which contributes to the net enhancement in the total summed transmission of all propagating orders (Figure 38(a₂-d₂)).

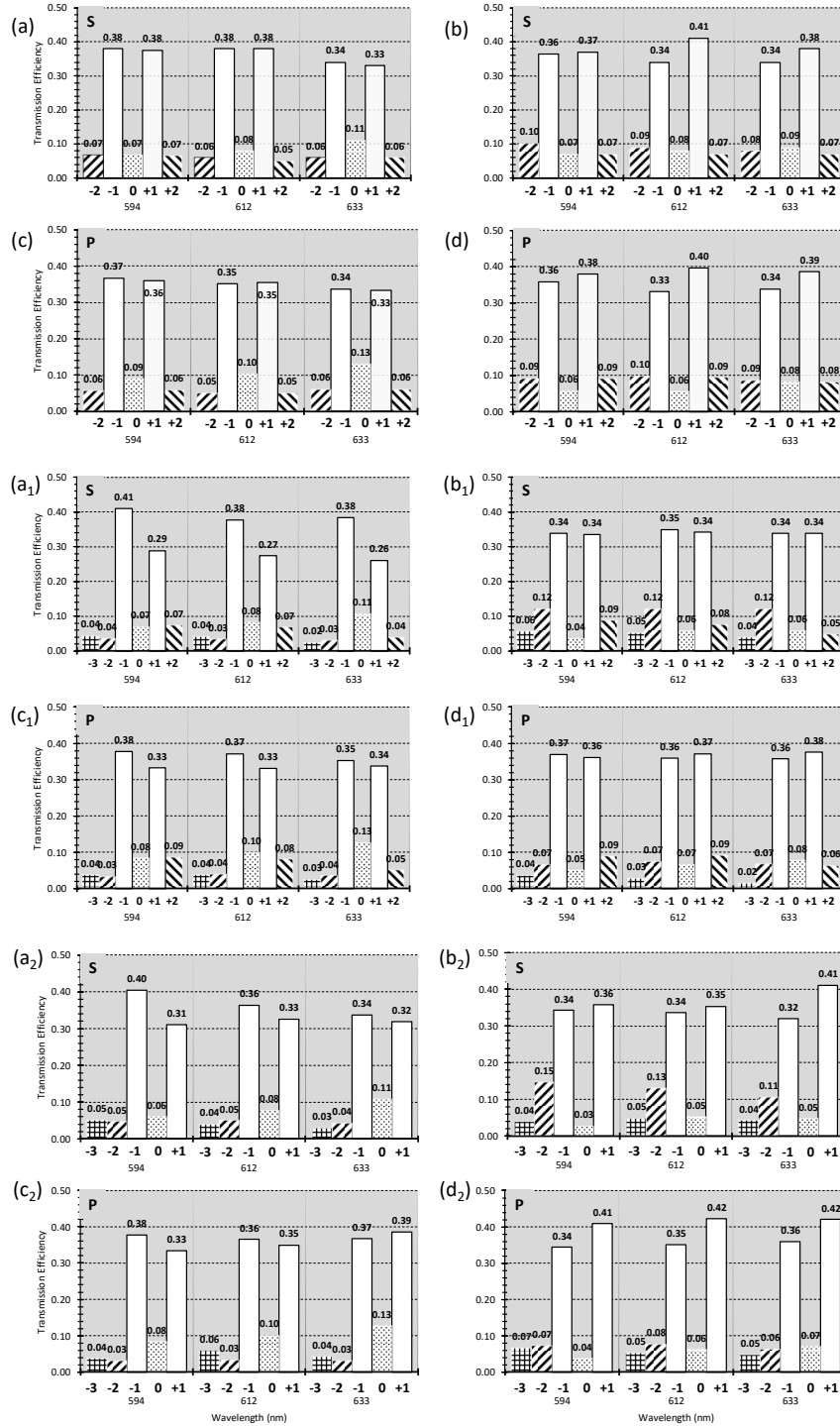


Figure 38: Transmission diffraction efficiencies for the 1.595 μm period grating at normal incidence (a-d). Comparison between efficiencies of all propagating orders for (a) unprocessed FS grating for S polarization, (b) rARSS FS grating for S polarization, (c) unprocessed FS grating for P polarization and (d) rARSS FS grating for P polarization, at each test wavelength. Similar plots at (a₁ – d₁) 1st Bragg incidence and (a₂ – d₂) 2nd Bragg incidence.

For 1.166 μm period grating, under normal incidence mounting, the efficiencies η_{+1} and η_{-1} and the zeroth-order η_0 have the same transmittance enhancement value after the fabrication of the rARSS on the grating surface (Figure 39 (a-d)). This trend was observed for all the test wavelengths and both S and P polarizations. At 612nm incident wavelength a definite enhancement in all individual orders was observed for normal incidence.

For the original unprocessed grating, the measured efficiency (figure 39(a₁ and c₁)) of η_{-1} is greater than η_{+1} under 1st Bragg incidence, which was verified by simulations (figure 36(b)). The fabrication of rARSS on the grating resulted in η_{-1} measured intensities that were considerably higher compared to η_{+1} , with additional enhancement in η_0 (figure 39(b₁ and d₁)). This was verified at all test wavelengths and both S and P polarizations.

At 2nd Bragg incidence the +1-order becomes evanescent. The measured intensity η_{-1} remained almost similar with an enhancement in η_{-2} after rARSS were fabricated on the grating (Figure 39(a₂ – d₂)).

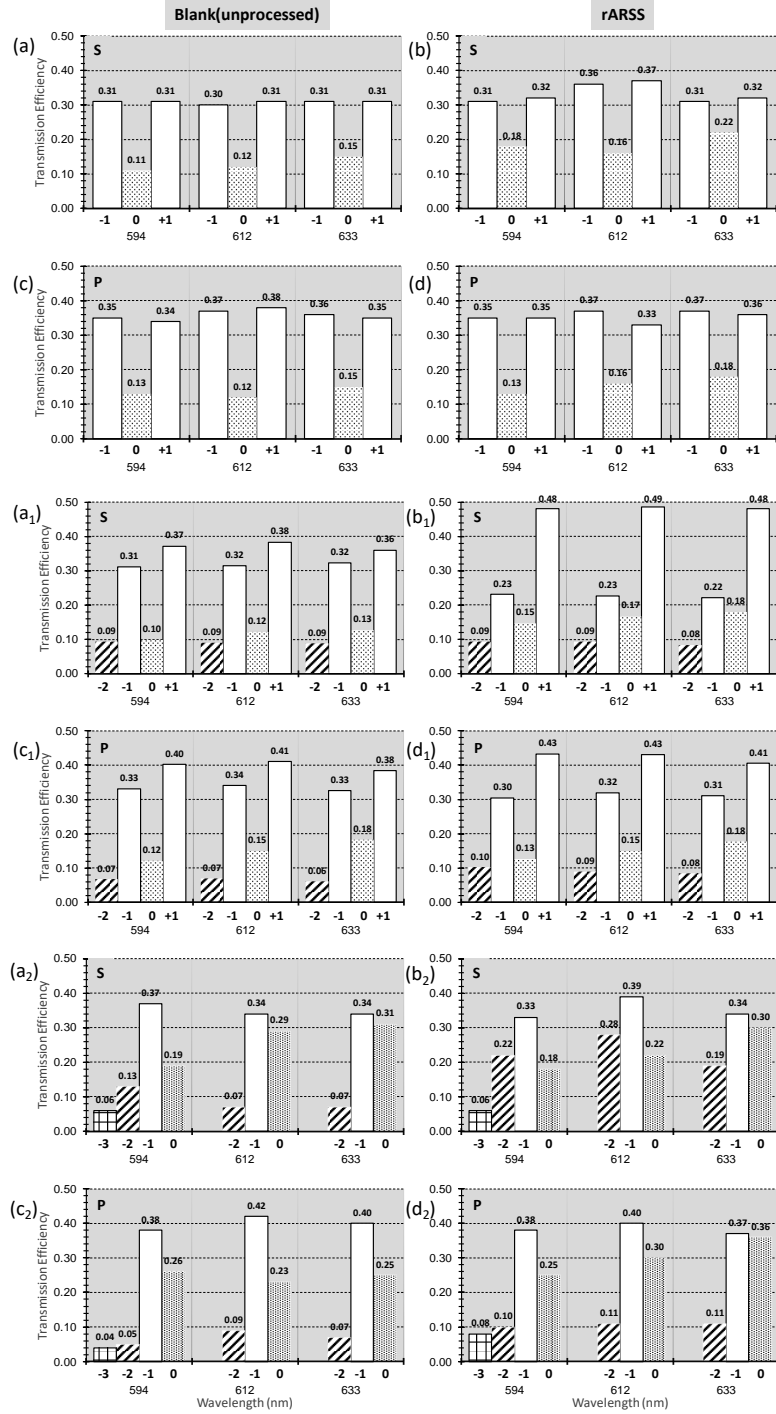


Figure 39: Transmission diffraction efficiencies for the $1.166\mu\text{m}$ period grating at normal incidence (a-d). Comparison between efficiencies of all propagating orders for (a) unprocessed FS grating for S polarization, (b) rARSS FS grating for S polarization, (c) unprocessed FS grating for P polarization and (d) rARSS FS grating for P polarization, at each test wavelength. Similar plots at (a1 – d1) 1st Bragg incidence and (a2 – d2) 2nd Bragg incidence.

3.3.5 Diffracted Beam profile measurements

To complete the tests of the effects of rARSS nanostructures on binary fused silica gratings, the beam profiles of the diffracted light were measured using a CCD camera beam profiler (BC106N by THORLABS). The beam profile of the input gaussian beam from the He-Ne laser was measured for the original grating and rARSS processed grating. The gaussian beam profiles were measured for ± 1 diffraction orders, which carry the maximum transmission efficiency. To see the small variations in the gaussian profiles, the measured beam profiles were plotted on a vertical logarithmic scale, and are shown below for 612nm incident wavelength and both S and P polarization, which was the maximum enhancement wavelength. Figure 40 and 41 show the beam profiles for ± 1 diffraction orders at normal and 1st Bragg incidence. We can observe for both the gratings that the profile of the incident light remained almost unaltered by fabrication of the random AR structures on the gratings.

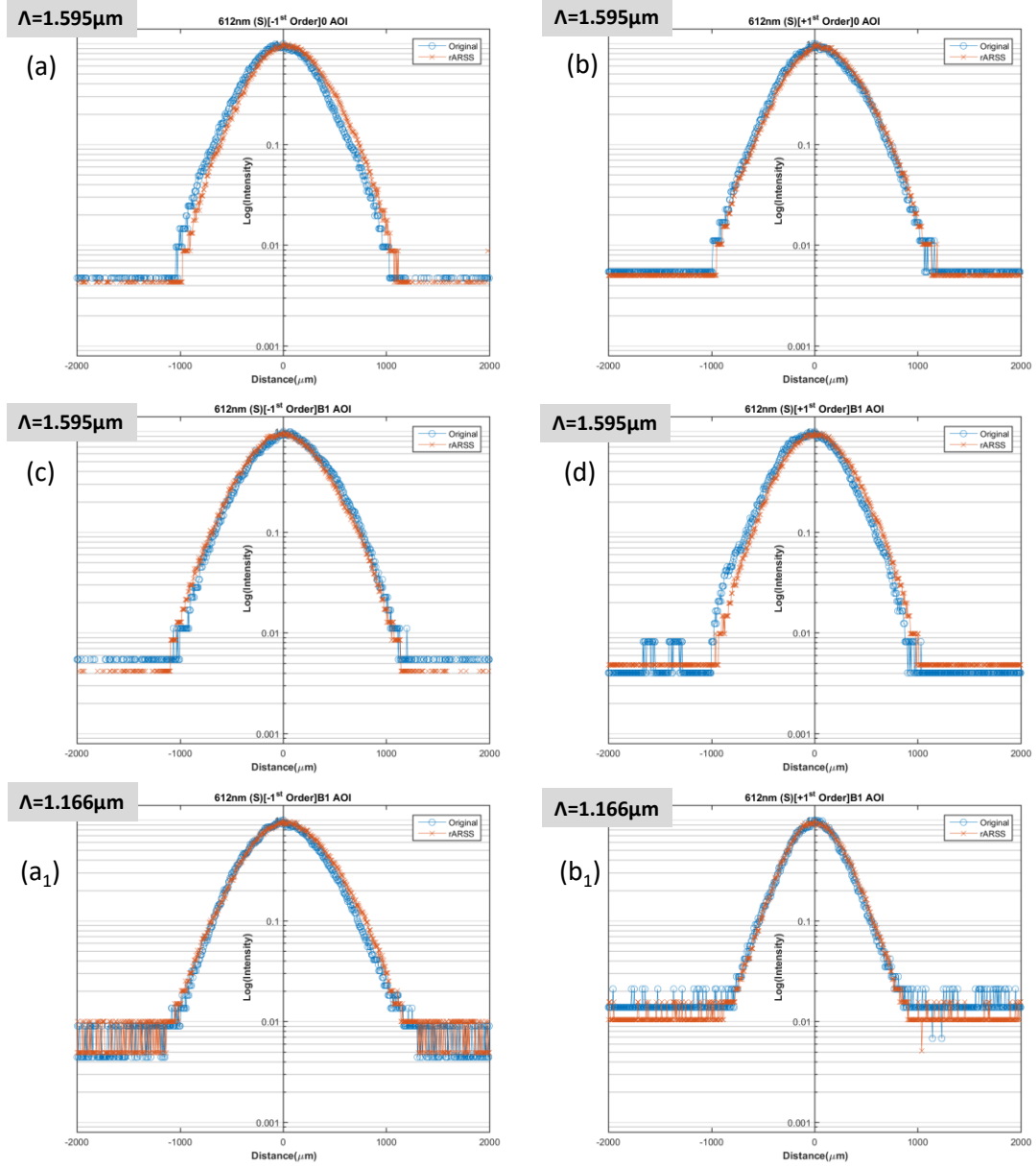


Figure 40: Transverse beam profile comparison between original and rARSS grating, for -1st and +1st diffraction orders at normal incidence (a-b), 1st Bragg incidence for 1.595 μm period grating (c-d) and, 1st Bragg incidence for 1.166 μm period grating (a₁-b₁). The data was measured for an incident wavelength of 612nm (S pol). The vertical (intensity) scale is logarithmic to accentuate differences between the profiles.

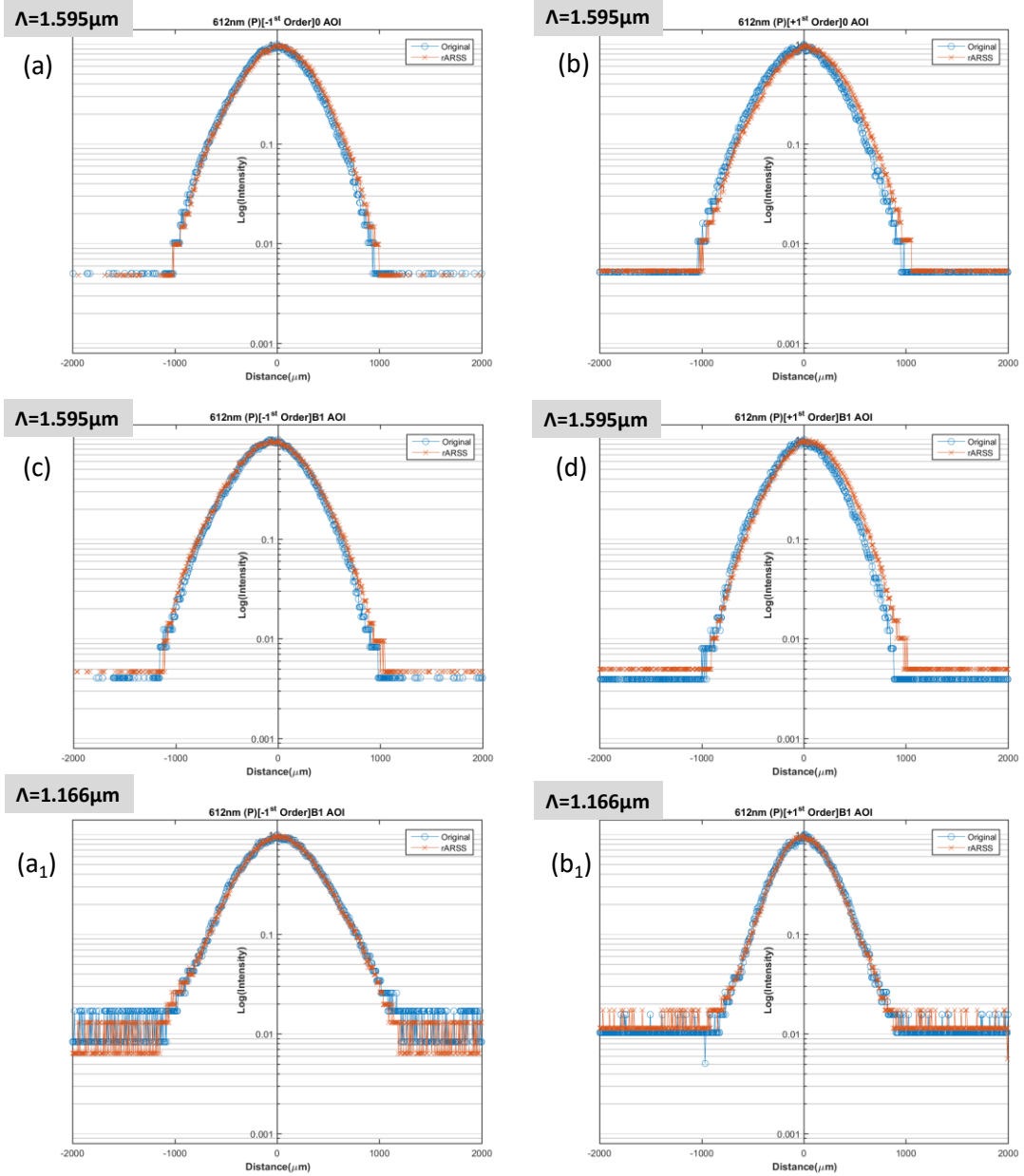


Figure 41: Transverse beam profile comparison between original and rARSS grating, for -1st and +1st diffraction orders at normal incidence (a-b), 1st Bragg incidence for 1.595 μm period grating (c-d) and, 1st Bragg incidence for 1.166 μm period grating (a₁-b₁). The data was measured for an incident wavelength of 612nm (P pol). The vertical (intensity) scale is logarithmic to accentuate differences between the profiles.

3.3.6 Granulometry results

The top-down SEM images shown in Figure 32(c,d) are used to analyze the lateral dimensions of the random structures created on the surface of the grating. To quantify the size distribution, granulometry was used. Granules used for classification were regular octagons, which varied in size from 1 to 81 pixels along their diagonal. Each pixel was scaled according to the dimension bar on the SEM image measurements. In order to observe the difference in size distribution of the structures on top of the grating, compared to the bottom (trenches), each SEM image was cut into different segments and the bottom and top portions of the grating were analyzed separately. This was done for both gratings, where the product of size distribution and corresponding spectrum is plotted across each granule diameter. Figure 42 represents the distribution histogram plots, where each plot shows the distribution of voids and islands within the SEM image. Each figure gives the details about the mean diameters of the voids and islands present in the image and the weights of the respective populations.

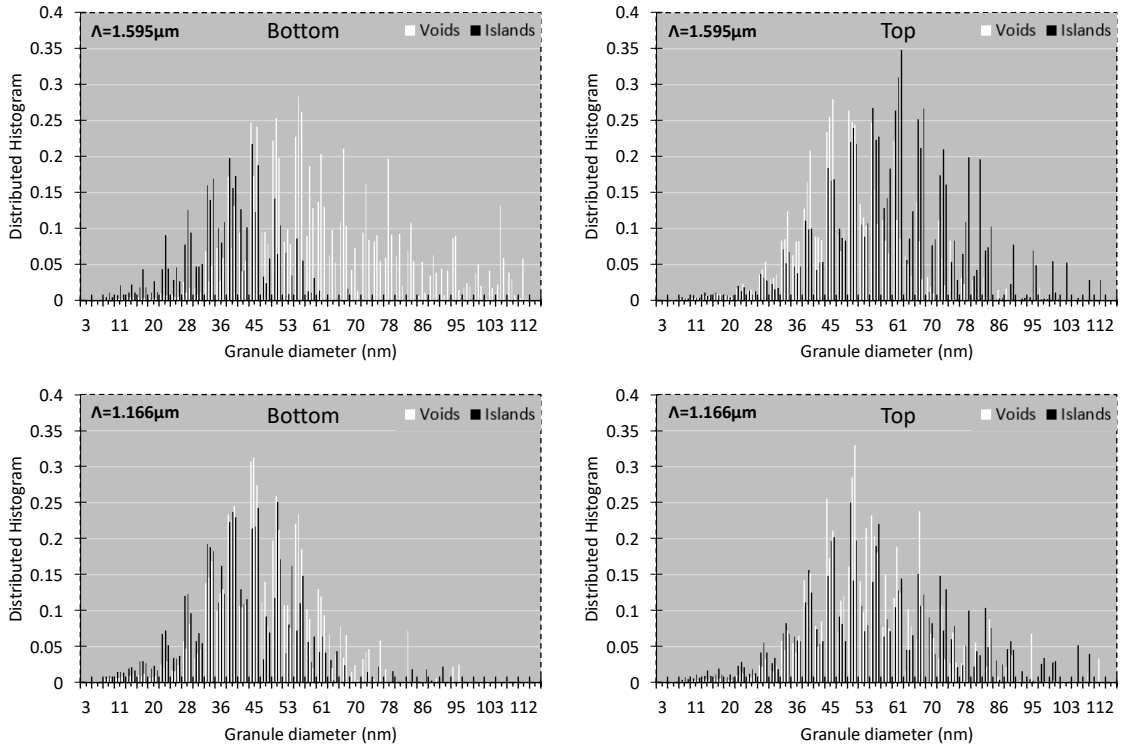


Figure 42: Distributed histograms of the rARSS feature populations on $1.595 \mu\text{m}$ period grating's: (a) Bottom surface and, (b) Top surface; as well as, $1.166 \mu\text{m}$ period grating's: (c) Bottom surface and, (d) Top surface. The feature sizes correspond to the SEM micrographs of the random structure on the gratings shown in Fig. 3(c,d). The distribution of islands is represented by the black bars and the voids by white bars. The populations are normalized to the total surface area.

Figure 42(a,b) shows that for $1.595 \mu\text{m}$ period grating, the bottom of the grating has smaller islands and larger voids, with a mean diameter of 40 nm and 53 nm respectively, while the top of the grating has larger islands and smaller voids, with a mean diameter of 61 nm and 50 nm respectively. This shows a difference in the size distribution of the islands on top compared to the bottom of the grating surface. Figure 42(c,d) shows that the distribution of islands and voids on top and bottom of the grating are similar to each other, with a mean diameter of around 50 nm for both islands and voids.

The coverage density of the islands and voids in an image can be extracted from the granulometry data. The percent coverage (ρ) can be calculated using Equation 14, where the granule size (h_g) is multiplied by the number of such granules occurring (δA_g) in the histogram, and summed up for all granules (N). The coverage was normalized over the total surface area (A) measured. This was done separately for both islands and voids, to get an estimate of the total percentage of the area counted by granulometry. We made sure the total percentage was below 100% to avoid overcounting the pixels (Equation 15). The percent coverage for each grating and its surface is shown in Table 11. It should be noted that the sum of percent coverage of islands and voids should not exceed 100% for an individual image, to make sure that the program is not over-counting the pixel clusters (granules).

$$\rho_{islands} = \left(\frac{1}{A}\right) \sum_{g=1}^N h_g \cdot \delta A_g \quad (14)$$

$$\rho_{islands} + \rho_{voids} \leq 100\% \quad (15)$$

Table 11: Percentage coverage density of voids and islands for bottom and top surfaces of 1.595 μm and 1.166 μm period gratings.

Grating	Bottom coverage (ρ)		Top coverage (ρ)	
	Voids	Islands	Voids	Islands
1.595μm	59.1%	32.8%	46.9%	48.6%
1.166μm	51.2%	41.4%	53.0%	41.5%

The percent coverage of voids and islands for 1.166 μm period grating has the same ratio on bottom and top surface. Which is not the case for 1.595 μm period grating, where the bottom has much higher percentage of voids compared to the top. It is important to note these differences of the random structures, as they change the effective index of the AR region on top and bottom of the grating surfaces.

For better visualization, a depiction of how the surface of the gratings would look with rARSS is shown in Figure 43. Figure 43(a) represents the large period grating (1.595 μm), with more islands on the top compared to the bottom. This implies that in the AR surface on the top, we have more fused silica compared to the AR surface on the bottom. This results to a higher effective index on the top AR surface compared to the bottom AR surface, that has more air and less fused silica. For the small period grating (1.166 μm) shown in Figure 43(b), the density of islands is similar on top and bottom of the grating surface (41.5%). This results to a similar effective index of the AR surface on the top and bottom of the grating.

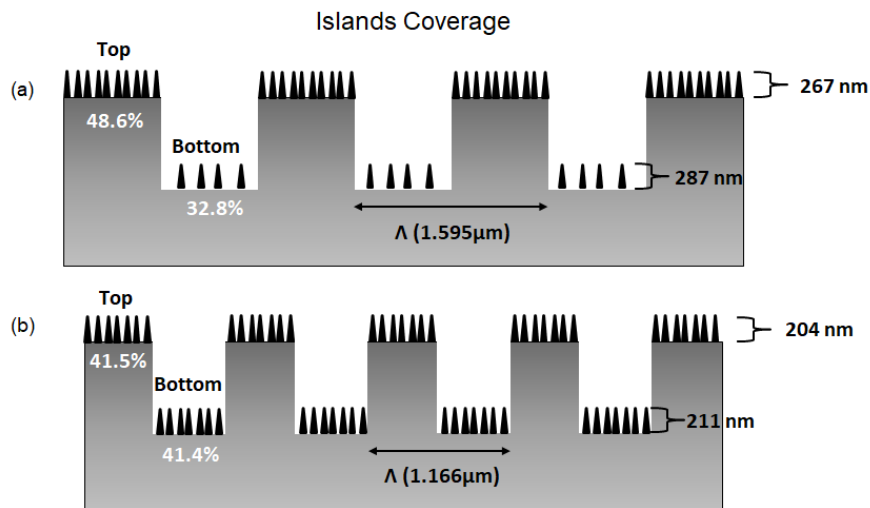


Figure 43: Visual representation of the percentage island coverage in the top and bottom of the rARSS grating with a period of (a) 1.595 μm and (b) 1.166 μm .

3.4 Optical performance vs angle of incidence

In this section, we present the diffraction efficiency performance of two near-wavelength period binary gratings at variable angle of incidence (AOI) for both S and P incidence polarizations. The transmission of the propagating diffracted orders was measured with varying angle of incidence from 0° to 70° in steps of 2° for the original unprocessed grating and rARSS grating. This was done for both S and P polarizations at three incident wavelengths (594nm, 612nm and 633nm). The data reported in this section is only for a wavelength of 612nm, as the maximum enhancement was measured at that wavelength and at the other wavelengths similar trends were observed with varying incidence angle. Individual propagating order efficiencies were measured and then summed to get the total transmission intensity for a particular AOI and polarization state. The plots (Figure 44 - 47) represent a direct comparison of transmission intensity post and pre-fabrication of rARSS on top of the gratings.

The $1.595\mu\text{m}$ period grating has 5 propagating orders (-2, -1, 0, +1, +2) at 0° AOI and as the AOI increases “+1” and “+2” orders become evanescent and higher orders (-3, -4 and -5) become non-evanescent. Figure 44 and 45 show the transmission intensity plots with varying AOI for S and P polarized incident light. Comparing the total transmission efficiency, we observed a definite enhancement across all AOI for rARSS grating compared to the original grating. The enhancement for S polarized light (Figure 44(a)) was higher compared to the P polarized light (Figure 45(a)). This was due to the fact that for an unprocessed flat substrate, the S polarized light has less efficiency than the P polarization at higher AOI, and we observe a polarization splitting for AOI greater

than 30° . For a rARSS processed flat substrate, a report indicated that polarization insensitivity was observed for AOI up to 55° [11]. A similar effect was observed in case of the total summed transmission of gratings to get the polarization insensitivity at higher AOI, due to which the enhancement for S polarized light was higher compared to P polarization for AOI greater than 40° . It is commonly known that internal reflections from front and back surface of an optical window results in interference effects. These interference effects lead to oscillations in the transmission intensity with variable AOI, which was observed in the case of total summed transmission efficiency for the unprocessed gratings from 0° to 20° . Due to processing of rARSS on both the surfaces of the grating, the internal reflections from the flat side vanish and we observe a much smoother curve without oscillations in the transmission intensity with varying AOI.

Total summed diffraction efficiency plots for $1.595\mu\text{m}$ period grating (Figure 44(a) and 45(a)) show a large drop in the intensity at an incidence angle of 40° . This happens mainly due to the +1 order (maximum efficiency order) becoming evanescent at 40° AOI, creating a grating anomaly. After rARSS fabrication it was observed that the intensity loss at the anomaly has been reduced by a factor of 10-20%. This is due to distribution of the lost light into other propagating orders compensating for the loss from +1 order.

Figure 44 (b₁ – b₈) and 45 (b₁ – b₈) show the individual order comparison with varying AOI for S and P polarized incident light. It was observed that the cut-off angle for the +2 and +1 diffraction orders remained unchanged, due to the unchanged grating period. And overall the intensity of the orders was enhanced by fabrication of rARSS onto the grating profile.

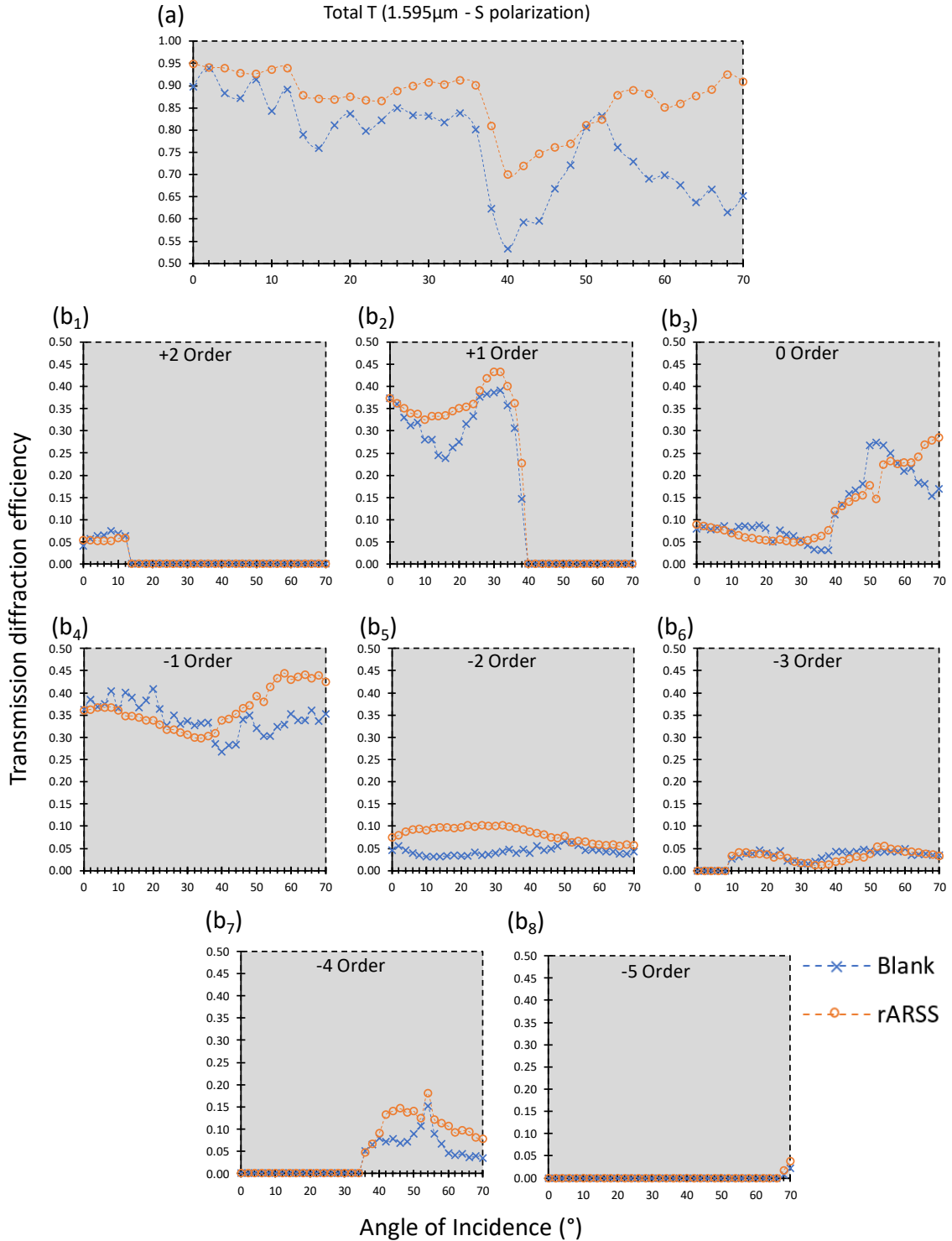


Figure 44: Measured transmission diffraction efficiency vs AOI for 1.595 μm period grating at S polarization. The cross labels represent the original grating, while the circles represent the rARSS grating. The plots represent (a) Total summed efficiency and (b₁ – b₈) individual order efficiencies.

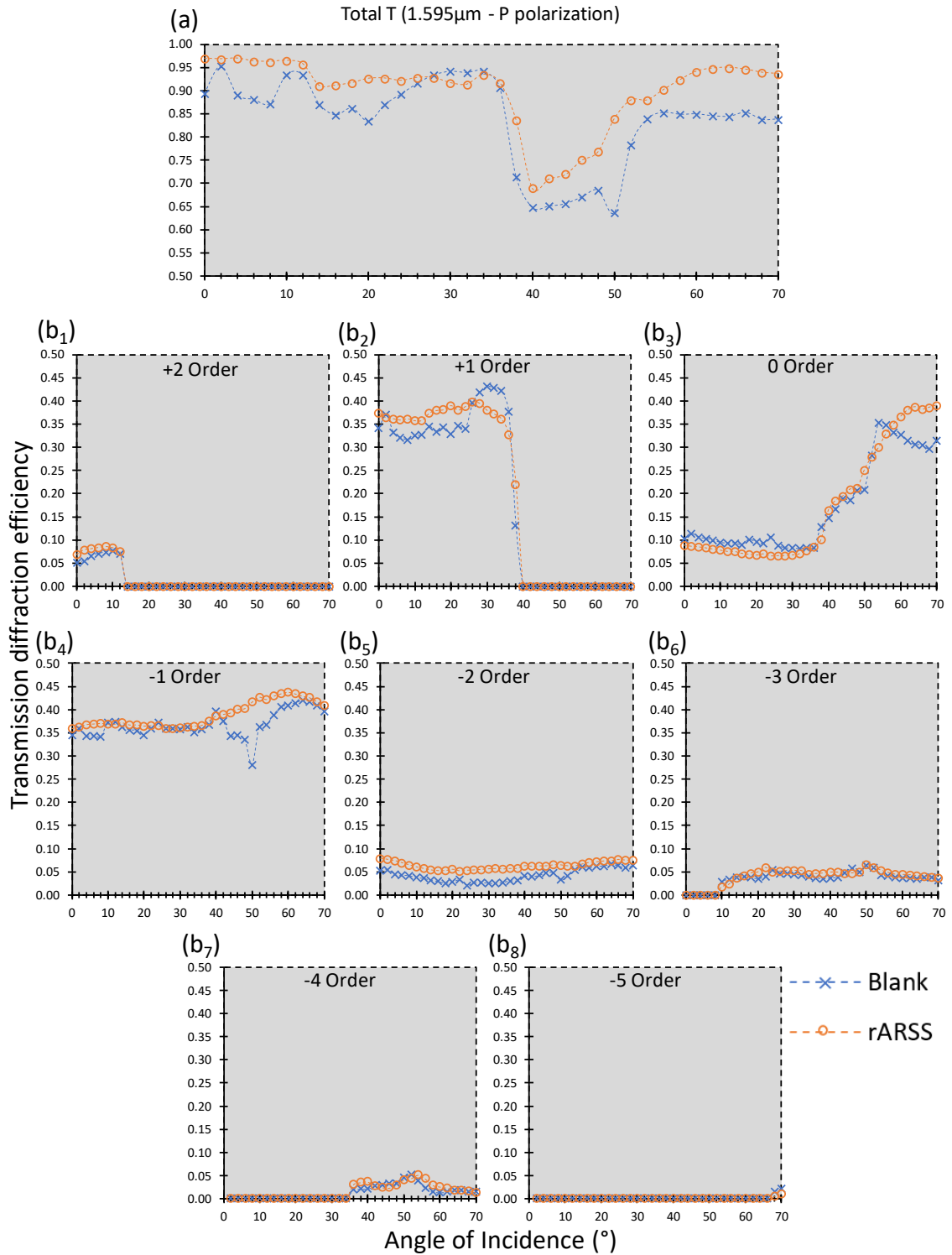


Figure 45: Measured transmission diffraction efficiency vs AOI for 1.595 μm period grating at P polarization. The cross labels represent the original grating, while the circles represent the rARSS grating. The plots represent (a) Total summed efficiency and (b₁ – b₈) individual order efficiencies.

The 1.166 μm period grating has 3 propagating orders (-1, 0, +1) at 0° AOI and as the AOI increases “+1” order becomes evanescent and higher orders (-2 and -3) become non-evanescent. Comparing the total transmission efficiency, a definite enhancement across all AOI was observed for rARSS grating compared to the original grating. The enhancement for S polarized light (Figure 46(a)) was higher compared to the P polarized light (Figure 47(a)). The interference effects were observed in the case of total summed transmission efficiency for the unprocessed gratings from 0° to 20° and for rARSS grating, a smooth curve was observed without oscillations in the transmission intensity along variable AOI.

Total summed diffraction efficiency plots for 1.166 μm period grating (Figure 46(a) and 47(a)) show a large drop in the intensity at an incidence of 30° due to the +1 order becoming evanescent at 30° AOI. After rARSS fabrication it was observed that the intensity loss at the anomaly has been again reduced by a factor of 10-20%. A similar effect of higher enhancement for S polarized light for AOI greater than 50° was observed for total summed transmission efficiency of the grating.

Figure 46 (b₁ – b₅) and 47 (b₁ – b₅) show the individual order comparison with varying AOI for S and P polarized incident light. A similar effect was observed for the cut-off angle of +1 diffraction order, which remained unchanged. The overall intensity of the orders was enhanced by fabrication of rARSS onto the grating profile. Although for 0th order, the shape of the diffraction efficiency curve with varying AOI changed after rARSS fabrication and a much smoother transition was observed across the AOI (Figure 46(b₂)).

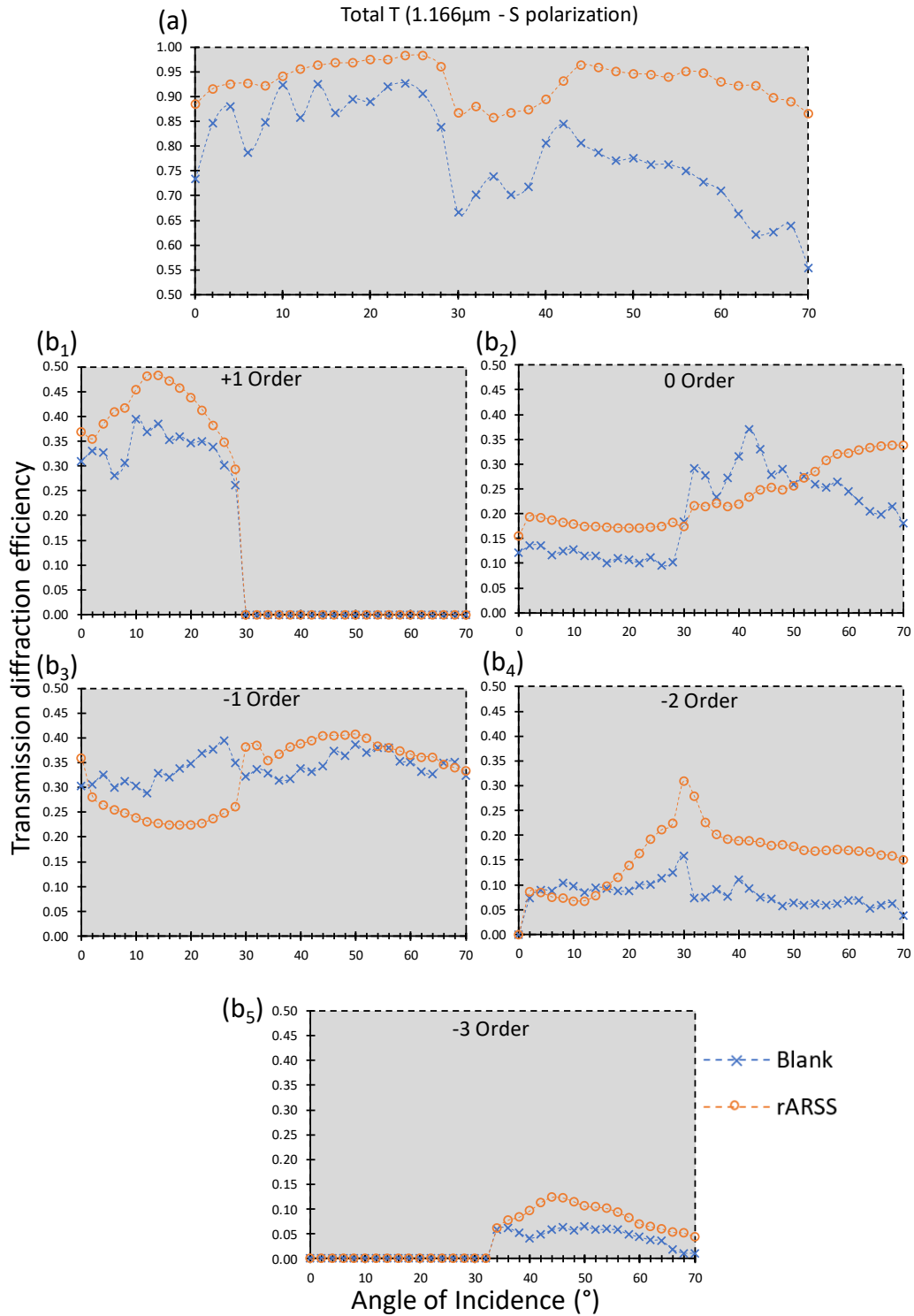


Figure 46: Measured transmission diffraction efficiency vs AOI for 1.166 μm period grating at S polarization. The cross labels represent the original grating, while the circles represent the rARSS grating. The plots represent (a) Total summed efficiency and (b₁ – b₅) individual order efficiencies.

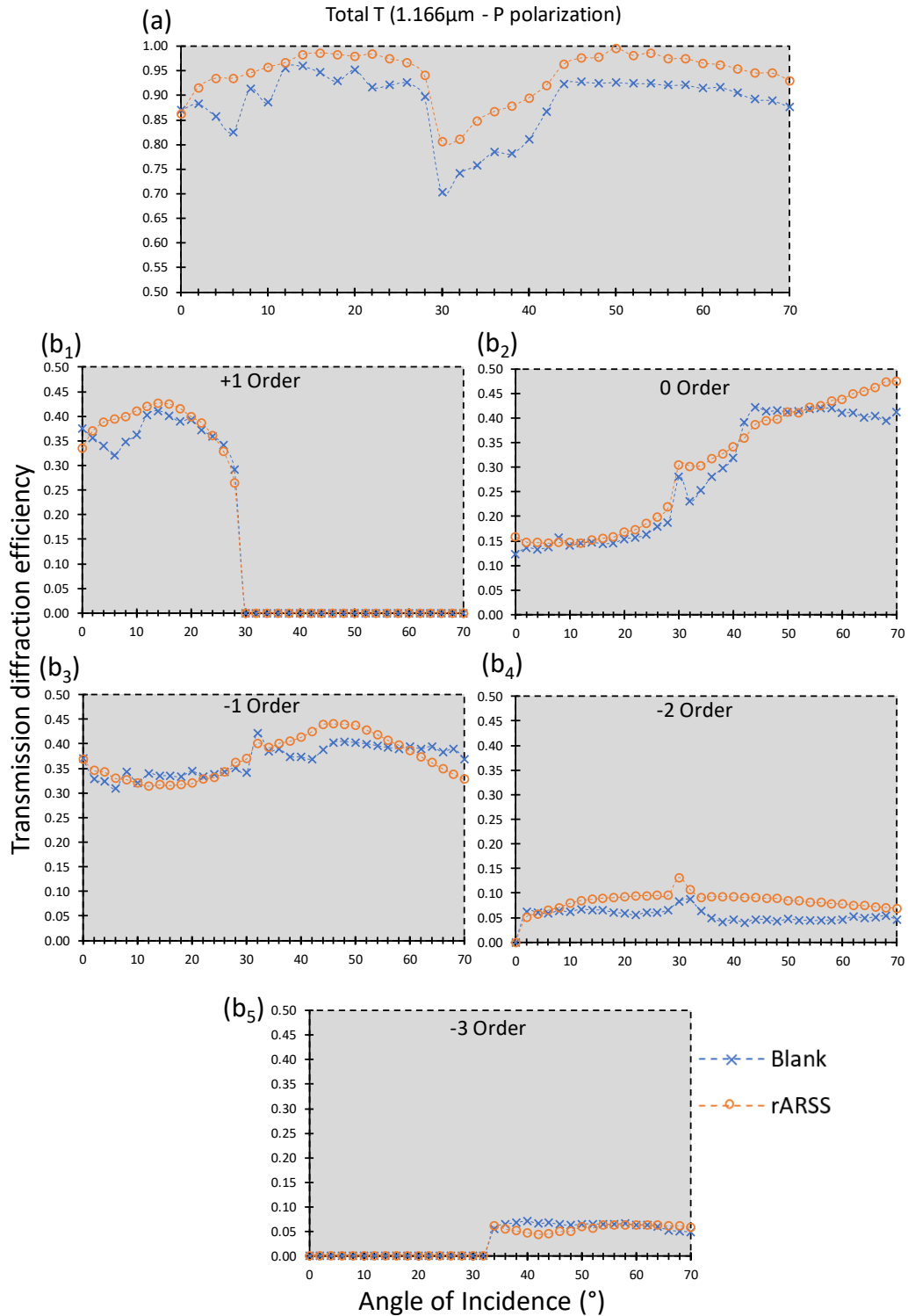


Figure 47: Measured transmission diffraction efficiency vs AOI for 1.166 μm period grating at P polarization. The cross labels represent the original grating, while the circles represent the rARSS grating. The plots represent (a) Total summed efficiency and (b₁ – b₅) individual order efficiencies.

3.5 Diffraction efficiency comparison of measured and simulated gratings

To verify the measured diffracted efficiency results of the gratings, each grating was simulated in VirtualLab Fusion software [55] and using a rigorous coupled wave analysis (RCWA) routine in MATLAB. VirtualLab is a packaged software, where as the RCWA routine is a MATLAB program. Both use vector analysis to find the efficiencies of the propagating transmission orders. The unprocessed (Blank) grating and a perfect single-layered anti-reflective (SLAR) processed grating were simulated using the software. A refractive index of $\sqrt{n_{FS}n_{Air}}$ was used as the material for the SLAR interface. The measured and simulated data of the original grating, the simulated date of the SLAR grating and measured data of rARSS grating were compared (Figure 48).

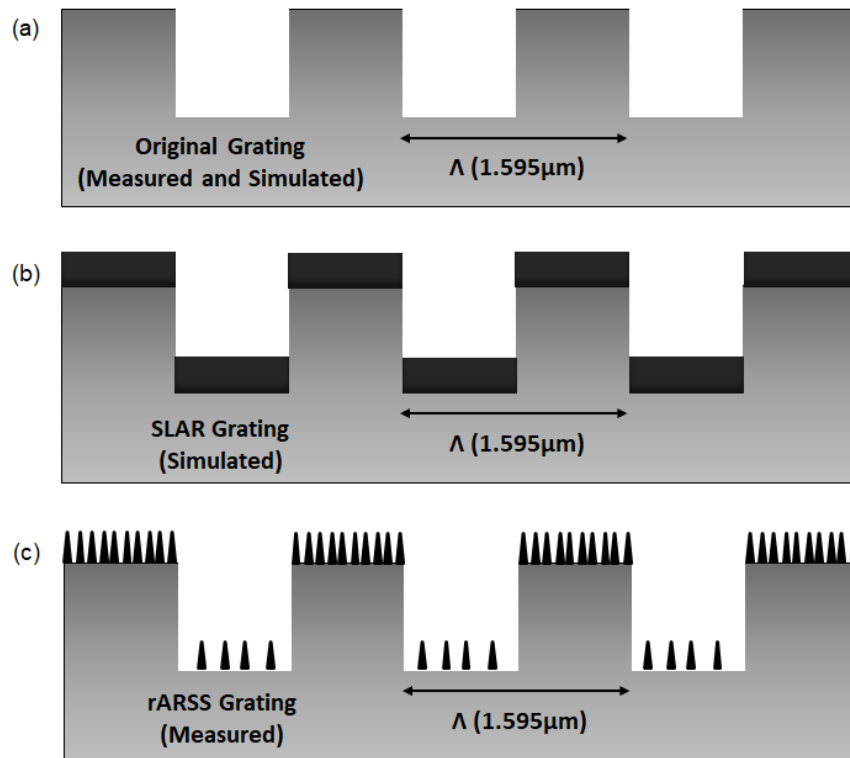


Figure 48: Visual representation of the comparison between (a) original, (b) SLAR, and (c) rARSS grating.

Figure 49 and 50 show the comparison of measured and simulated efficiency of the diffracted orders as a function of incidence angle for 1.595 μm and 1.166 μm gratings, at 612nm incident wavelength and S polarized light. Good agreement was observed between the simulated and measured total diffraction efficiency for the original unprocessed gratings (Figure 49(a) and 50(a)). For 1.595 μm grating, the total diffraction efficiency for SLAR grating data matches with the rARSS grating to 38° incidence, and for AOI greater than 40° the transmission of SLAR is much lower compared to the rARSS grating (Figure 49(a)). Similar trend was observed for 1.166 μm period grating, where the total transmission of SLAR and rARSS was similar to about 30°, after which we can see a huge enhancement in transmission of rARSS grating at higher AOI (Figure 50(a)). The rARSS grating was more efficient than a SLAR grating at higher angles of incidence. At the anomalies of total transmission, the enhancement due to rARSS was much higher compared to the SLAR. With regards to the individual order efficiency, the SLAR grating simulation shows a similar enhancement for all the order with no change in the shape of the diffraction efficiency curve with varying AOI. But in case of rARSS grating some orders had a much smoother transition across the AOI, which was mainly visible for the 0th diffraction order (Figure 49(b₃) and Figure 50(b₂)).

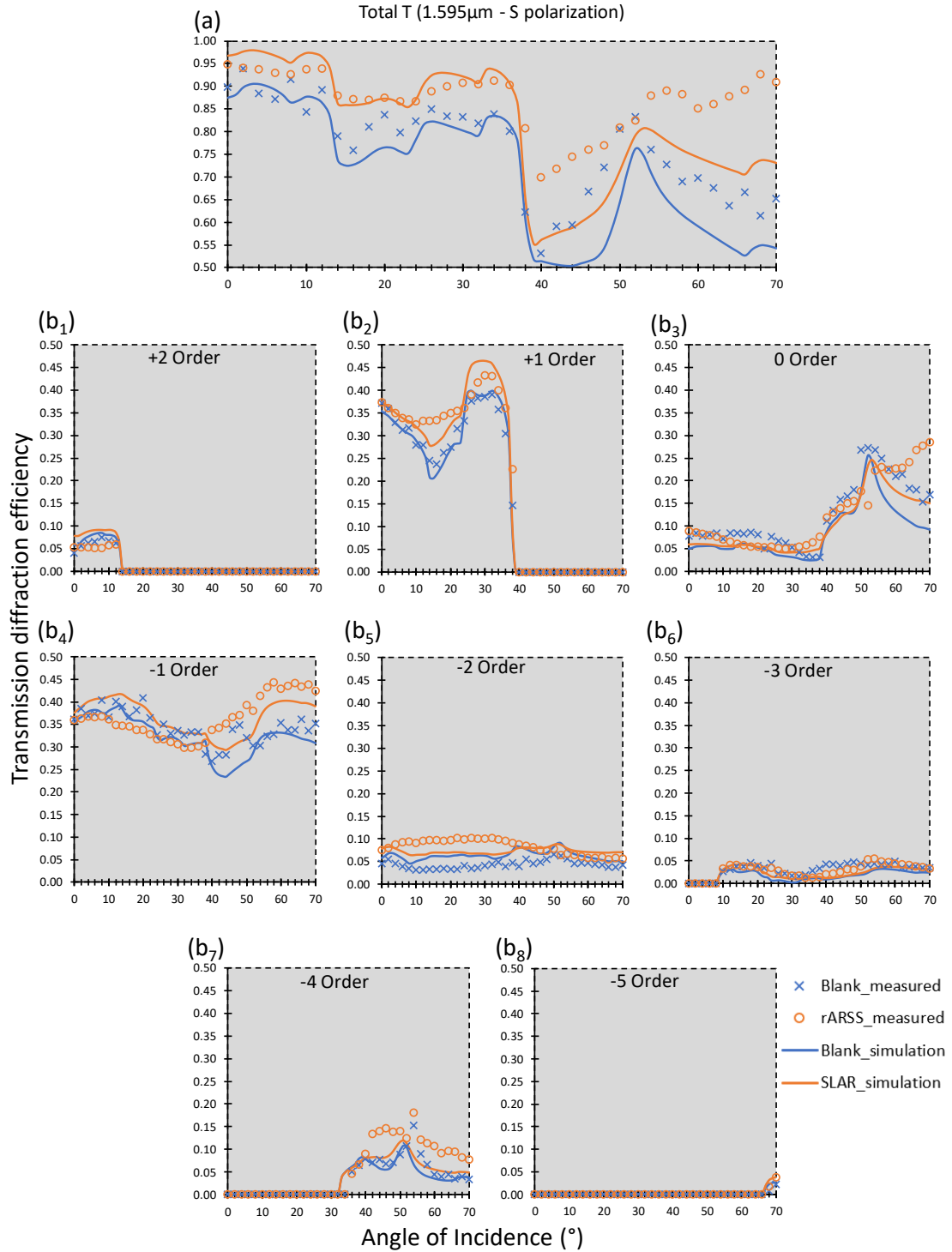


Figure 49: Measured and simulated transmission diffraction efficiency vs AOI for 1.595 μm period grating at 612 nm incidence wavelength (S polarization). The plots give a comparison between the original (blank), SLAR and rARSS grating. The plots represent (a) Total summed efficiency and (b₁ – b₈) individual order efficiencies.

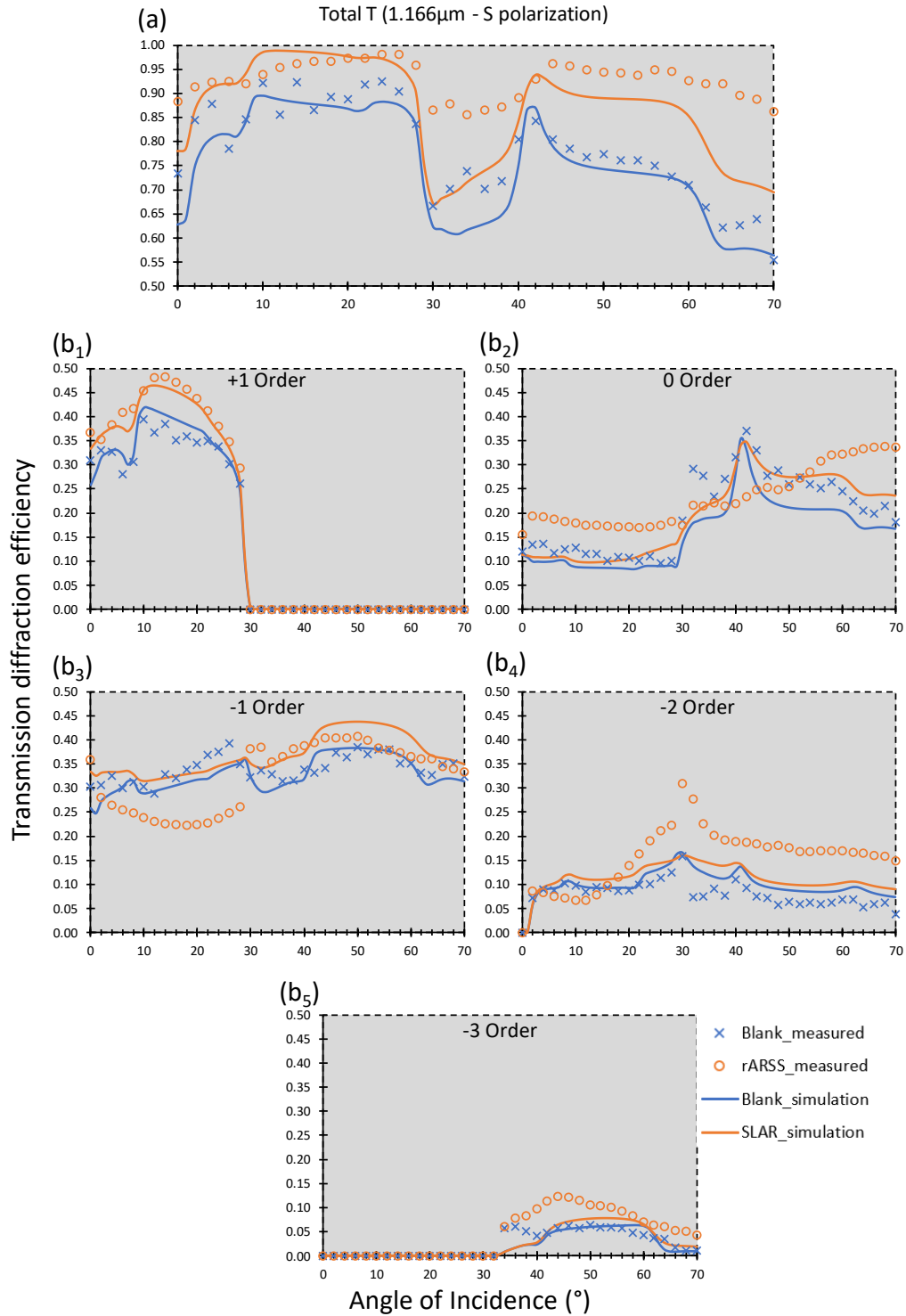


Figure 50: Measured and simulated transmission diffraction efficiency vs AOI for 1.166 μm period grating at 612 nm incidence wavelength (S polarization). The plots give a comparison between the original (blank), SLAR and rARSS grating. The plots represent (a) Total summed efficiency and (b₁ – b₅) individual order efficiencies.

Finally, comparing +1 and -1 order diffraction efficiency vs AOI to of each other for 1.595 μm period grating. The curves intersect at a particular AOI for the unprocessed grating, which changes after rARSS fabrication (Figure 51). From the simulation of cross-section point of ± 1 order vs changing phase depth of the 1.595 μm grating, it was observed that the measured phase depth variation due to random structures match the simulation of varying phase depth for both S and P incidence polarization (Figure 52). This can be used as a technique to estimate the phase depth of the grating without dicing the actual grating. It works as a non-destructive technique to monitor the surface modification on gratings due to the etching process. It also indicates an effective depth (phase) for the randomly structured layer.

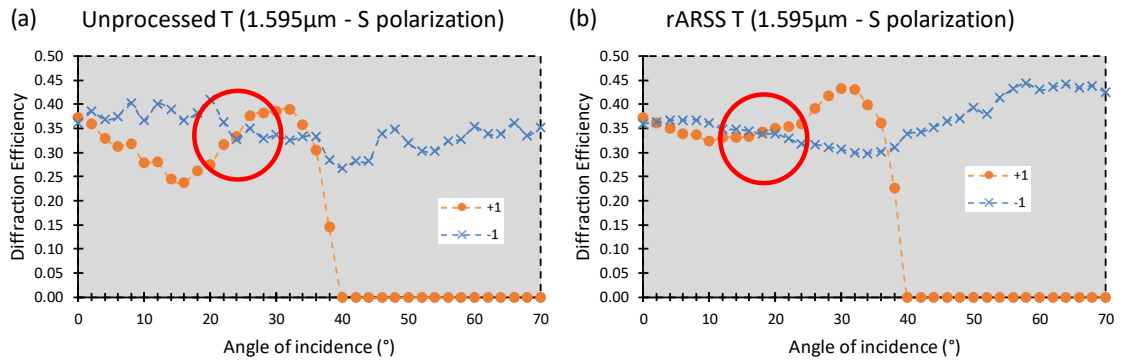


Figure 51: Figure showing the intersection point of +1 and -1 order for (a) unprocessed and (b) rARSS processed 1.595 μm period grating.

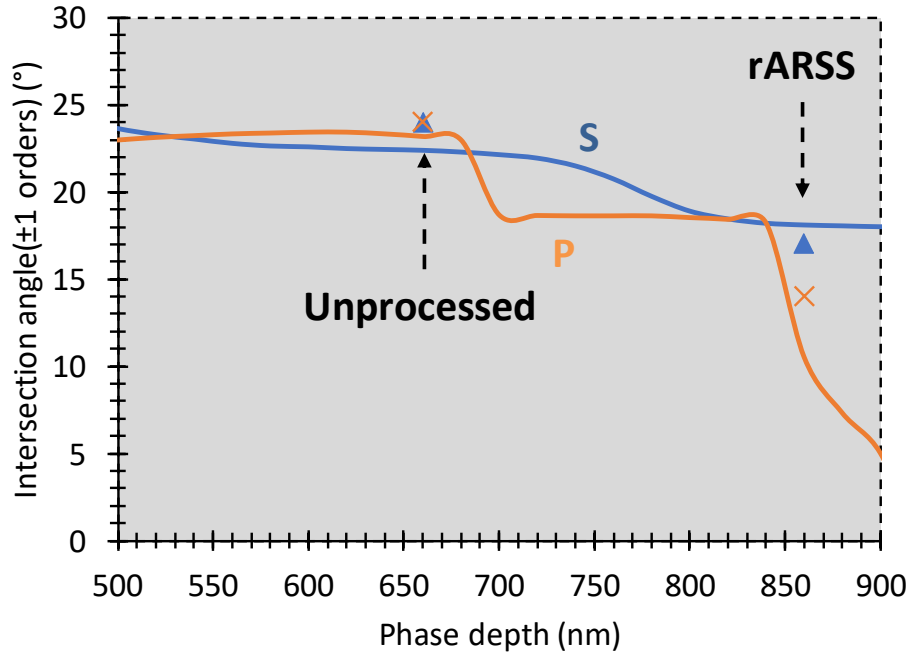


Figure 52: Comparison of the variation of the intersection angle of ± 1 order with changing phase depth of the grating. The solid lines represent the simulated results and the individual points represents the measured data for both S and P incidence polarization.

3.6 Summary and Discussion

The rARSS nanostructuring treatment on near-wavelength scale period, linear, binary, phase gratings were tested to observe performance effects. The structures were fabricated on two commercially purchased gratings with periods of $1.595 \pm 0.050 \mu\text{m}$ and $1.166 \pm 0.050 \mu\text{m}$ using a single-step etching process in a reactive-ion etching tool. The same etch parameters were used to fabricate random nanostructures on both the gratings, and on both respective surfaces (front-back).

The SEM images verified the presence of random structures on the top and inside the grooves (trenches) of both gratings. The periodicity of the gratings appeared to be

unaffected, as the binary phase sidewalls were not perturbed, which was confirmed by measurement of the diffraction angles of all propagating diffraction orders, under all test conditions. We concluded that the rARSS treatment has no adverse effects on the grating periodicity after the etching fabrication process.

The reflected diffraction efficiency was reduced by a factor of 10 after rARSS fabrication on top of the gratings, which suggests that the structures act as an anti-reflective treatment. The reflection efficiency of both the gratings was less than 2% on average, at normal and Bragg incidence conditions. A definite enhancement of the total diffracted transmission efficiency of the sum of all propagating orders was verified, which confirms that the reduced reflection efficiency results in transmission enhancement and not scattering. This result suggests that the small columnar defect at the edge of the binary phase transition sidewall has minimal adverse effects, mainly due to its considerably subwavelength diameter.

Comparing individual propagating diffraction efficiencies for the transmitted orders we measured a preferential enhancement in a particular order for each grating under different mounting conditions. For the large period grating ($1.595\mu\text{m}$), equal grating transmission intensities of the ± 1 orders for both s and p polarizations was observed at 1st Bragg incidence, and at normal incidence we observed that the rARSS grating ± 1 order transmission efficiency were unequal. For the small period grating ($1.166\mu\text{m}$), at 1st Bragg incidence, the +1st order transmission efficiency is higher with rARSS, while at 2nd Bragg incidence, the -2nd order transmission efficiency is higher with the random structures present. The effect was more pronounced with S-polarized incident light, and not as much with P-polarization. Simulations confirmed that this preferential

diffraction efficiency enhancement is possible for a single thin-film AR coating, provided that the film thickness at the elevated grating feature is “thinner” than the film thickness in the groove of the grating. The same value preferential transmission enhancement for the simulations was noted for a factor of four (4x) larger than the one we measured in the gratings tested. This discrepancy may be due to the simplified simulation model we used, as a single-layer AR coating with index equal to the radical of the fused silica index ($\sqrt{n} \cong 1.21$), and not a gradient index profile.

The presence of the rARSS on the grating surfaces had no measurable effect on the transverse beam profiles of the diffracted orders, at any test conditions presented here. The granulometry data showed that the percent coverage of voids and islands for 1.166 μm period grating has the same ratio on bottom and top surface, whereas for 1.595 μm period grating, the bottom has much higher percentage of voids compared to the top. This changes the effective index of the AR surface on top and bottom for the 1.595 μm period grating.

Measuring the total diffraction transmission efficiency with varying AOI from 0° to 70°, a definite enhancement was observed for both the grating at S and P polarizations. The oscillations at lower AOI were reduced and an enhancement of more than 20% was observed for S polarization at AOI greater than 40°. Comparing the RCWA simulation of a SLAR grating with the rARSS grating, similar enhancement was observed till 30° AOI, but the SLAR grating did not show the huge enhancement like the rARSS grating for AOI greater than 40°.

Based on our extensive test results, we conclude that the fabrication of random nanostructures on pre-existing binary fused silica gratings have the desired reduction in diffracted reflection efficiency, and enhancement of the total diffraction transmission efficiency, acting as an anti-reflective treatment. No adverse effects were observed on the diffractive properties of the original grating [56, 57].

CHAPTER 4: CONCLUSIONS

4.1 Summary of Optical performance of Random Anti-reflection Structured Surfaces on Flat Optical Windows

Two fundamentally different fabrication techniques were used to apply rARSS to flat optical windows. Random structures were created on fused silica by a two-step etching process. The first step involved gold sputtering to deposit a 20nm discontinuous layer on fused silica substrate, that acts as a seed layer to initiate the etch process. The second step involved etching the substrate in a fluorine plasma. The samples were tested for different etch times. It was observed that increasing the etch time resulted in an increased transmission enhancement at longer wavelengths.

The anti-reflective surface was characterized by measuring the effective depth and lateral dimensions of the random structures. Confocal microscope measurements showed that increasing the etch time increased the effective depth. This measurement indicated that the scattering edge of the transmission spectrum shifts to longer wavelengths due to the increase in effective depth of the random surface. The structure effective depth for maximum enhancement in the visible wavelength region was measured to be 0.5 μ m, which is of the order of a wavelength. Granulometry of the scanning electron micrographs of the etched surface gave a mean structure lateral dimension of around 55nm. This implies that the anti-reflective surface consists of tall, thin conical features. Maximum transmission, greater than 99%, was achieved within the 500 – 800 nm spectral region, for a double side processed fused silica substrate. Overall, the etching

technique created random nanostructures on fused silica substrate that act as a broad-band anti-reflective treatment, without thin film interference effects.

A different fabrication technique was used to create rARSS on Cleartran ZnS optical windows. A high-power, nanosecond duration pulsed laser was used to irradiate the surface and create roughness using localized sputtering and redeposition in atmosphere. This technique does not involve any etching or lithographic process.

Roughness measurements of the surface after irradiation have shown an increase in the effective ablated depth by increasing the net irradiation energy. It was also observed that the roughness does not change considerably for variable energy density for a set of pulses. The stratification ratio remained unchanged for the various irradiation tests performed, indicating a similar surface coverage profile density for all the irradiations tested. These results indicated a control on the measurable roughness on Cleartran ZnS.

Cleartran has a Fresnel's reflection loss of 14% per surface in the IR region. A single side irradiated surface showed a maximum transmission enhancement of 7% across the MWIR (3 - 10 μm) spectral region. No contaminations were formed on the surface due to oxidation in atmosphere like ZnO. Confocal microscopy measurements indicated the random surface structure height value of 135nm and, the granulometry of the random surface has shown the structure lateral dimensions to be around 25nm for the maximum enhanced sample.

The random structured surfaces were formed through an ablation and re-deposition process, triggered by the high-power laser pulse and performed as an anti-

reflective treatment on Cleartran surface. Overall, the irradiation technique enhancement was measured to be 7%, which was comparable to 6-10% enhancements found in the literature. The enhancement reported in the literature is due to a combined effect of nanostructuring and a thin film effect. The work presented here, successfully created rARSS on Cleartran ZnS with no oxidation observed (no thin film effect), implying the enhancement is completely due to the random nanostructuring.

The flat optical windows work has shown two different fabrication techniques to create random surface anti-reflective structures for visible and infrared optical windows.

4.2 Summary of Optical performance of Random Anti-reflection Structured Surfaces on Binary Diffraction Gratings

The rARSS nanostructuring treatment applied to flat optical windows was transferred on diffraction gratings, to observe any performance changes. The structures were fabricated on two commercially purchased gratings, with periods of $1.595 \pm 0.050 \mu\text{m}$ and $1.166 \pm 0.050 \mu\text{m}$, using a similar etching process as a flat window. The SEM images verified the presence of random structures on the top and inside the grooves (trenches) of both gratings. The periodicity of the gratings appeared to be unaffected, as the binary phase sidewalls were not perturbed, which was confirmed by measurement of the diffraction angles of all propagating diffraction orders.

The initial optical performance test involved comparing the reflected diffraction efficiency of rARSS grating and comparing it with the unprocessed grating. The results indicated a reduced reflection efficiency by a factor of 10 for both the gratings. The

resulting reflection efficiency over all orders of rARSS gratings was less than 2% on average for the performed test conditions. The next test was to observe if the reduced reflection efficiency resulted in an enhanced transmission or to losses due to scattering from the random surface profile. Comparing the total diffracted transmission efficiency (sum of all propagating orders), it was verified that the reduced reflection efficiency was converted to transmission enhancement. This was a verification that the random nanostructures acted as an AR treatment on binary diffraction gratings.

Next, the individual propagating transmission orders efficiencies were compared pre and post-application of rARSS. Since both the gratings were 50% duty cycle, the unprocessed gratings had an equal efficiency of ± 1 orders at normal incidence, while the remaining orders were suppressed. Post rARSS application, an asymmetry in the ± 1 orders was observed for the large period grating ($1.595\mu\text{m}$), although other orders still had less efficiencies compared to ± 1 orders. For the small period grating ($1.166\mu\text{m}$) the ± 1 orders had equal efficiencies post processing with an enhancement in the transmission efficiency.

The transverse beam profiles of the diffracted orders were measured, and no changes were observed in the profile due to rARSS fabrication. Granulometry data was taken for the SEM images and it showed that the coverage density of the random nanostructures was different on bottom and top surface for the $1.595\mu\text{m}$ period grating, and similar for the $1.166\mu\text{m}$ period grating. This implies that the effective index of the AR surface on top and bottom (grooves) for the $1.595\mu\text{m}$ period grating is different by a small amount.

To observe the effect of rARSS at high AOI, intensity of the transmitting diffracted orders was measured from 0° to 70° and summed together to get the total diffraction transmission efficiency at varying AOI. The results showed a definite enhancement in the transmission at all AOI for both the grating at S and P polarizations. Other interesting effects that were observed were, at lower AOI the oscillations from internal reflections were reduced and more than 20% enhancement was observed after rARSS fabrication for S polarization for AOI greater than 40° . To understand these effect, RCWA simulations of a SLAR coated grating were performed and compared with the rARSS grating measurements. A similar enhancement was observed to 30° AOI, but the SLAR grating did not show the huge enhancement, compared to the rARSS grating measurements for AOI greater than 40° .

In conclusion, the fabrication of random nanostructures on pre-existing binary fused silica gratings was possible and produced the desired reduction in diffracted reflection efficiency, and enhancement of the total diffraction transmission efficiency, acting as an anti-reflective treatment, while maintaining the original diffractive properties of the pre-fabricated grating.

4.3 Potential Future Work

The work presented in the dissertation has shown that random nanostructuring treatment on pre-existing binary diffraction gratings has resulted in an increase in the transmission while not effecting the diffractive properties such as the period, duty cycle, angular spread and the beam profiles. Other diffractive optic components such as Fresnel

lens (Figure 53(a)) and spot array generators (Figure 53(b)) also are subject to Fresnel's reflections. Reducing the reflections using AR thin film coating for these components is much more complicated than the case of a grating, due to the Fresnel lens changes in spatial variation of the period and the spot arrays having a complex structure profile.

It would be interesting to investigate how the rARSS treatment on these optical components affects their diffractive properties and whether we get enhanced transmission. It would also be useful as the rARSS treatment can be done on pre-fabricated components and do not have to be considered prior to the fabrication of the optical component itself.

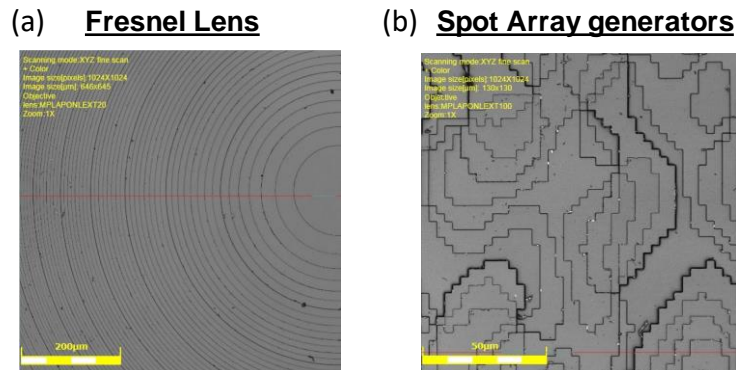


Figure 53:Microscope image of (a) Fresnel lens and (b) Spot array generators.

REFERENCES

- [1] D. Chen, "Anti-reflection (AR) coatings made by sol-gel processes: a review," *Solar Energy Materials and Solar Cells*, vol. 68, pp. 313-336, 2001.
- [2] S. Chattopadhyay, Y. Huang, Y.-J. Jen, A. Ganguly, K. Chen, and L. Chen, "Anti-reflecting and photonic nanostructures," *Materials Science and Engineering: R: Reports*, vol. 69, pp. 1-35, 2010.
- [3] Q. Yang, X. A. Zhang, A. Bagal, W. Guo, and C.-H. Chang, "Antireflection effects at nanostructured material interfaces and the suppression of thin-film interference," *Nanotechnology*, vol. 24, p. 235202, 2013.
- [4] D. H. Raguin and G. M. Morris, "Antireflection structured surfaces for the infrared spectral region," *Applied Optics*, vol. 32, pp. 1154-1167, 1993.
- [5] D. H. Raguin and G. M. Morris, "Analysis of antireflection-structured surfaces with continuous one-dimensional surface profiles," *Applied Optics*, vol. 32, pp. 2582-2598, 1993.
- [6] D. S. Hobbs and B. D. MacLeod, "High laser damage threshold surface relief micro-structures for anti-reflection applications," in *Boulder Damage Symposium XXXIX: Annual Symposium on Optical Materials for High Power Lasers*, 2007, pp. 67200L-67200L-10.
- [7] H. Kikuta, Y. Ohira, H. Kubo, and K. Iwata, "Effective medium theory of two-dimensional subwavelength gratings in the non-quasi-static limit," *JOSA A*, vol. 15, pp. 1577-1585, 1998.
- [8] D. S. Hobbs, B. D. MacLeod, and J. R. Riccobono, "Update on the development of high performance anti-reflecting surface relief micro-structures," in *Proc. SPIE*, 2007, p. 65450Y.
- [9] B. Zollars, S. Savoy, Q. Xue, J. John, K. Hoover, G. Elpers, *et al.*, "Performance measurements of infrared windows with surface structures providing broadband, wide-angle, antireflective properties," in *Proc. of SPIE Vol*, 2013, pp. 87080Q-1.
- [10] G. Sapkota, J. R. Case, L. E. Busse, J. A. Frantz, L. B. Shaw, J. S. Sanghera, *et al.*, "Characterization of random anti-reflecting surface structures and their polarization response at off-normal angles of incidence," in *Nanoengineering: Fabrication, Properties, Optics, and Devices XIII*, 2016, p. 992712.
- [11] A. Peltier, G. Sapkota, J. R. Case, and M. K. Poutous, "Polarization insensitive performance of randomly structured antireflecting planar surfaces," *Optical Engineering*, vol. 57, p. 037109, 2018.
- [12] L. E. Busse, J. Frantz, M. K. Poutous, I. Aggarwal, B. Shaw, and J. Sanghera, "Harsh environment tests of random antireflective surface structures on optics," in *CLEO: Science and Innovations*, 2017, p. JTu5A. 124.
- [13] D. S. Hobbs and B. D. MacLeod, "High laser damage threshold surface relief micro-structures for anti-reflection applications," in *Proc. SPIE*, 2007, p. 67200L.
- [14] D. S. Hobbs and B. D. MacLeod, "Design, fabrication, and measured performance of anti-reflecting surface textures in infrared transmitting materials," in *Proc. SPIE*, 2005, p. 578640.
- [15] L. E. Busse, C. M. Florea, J. A. Frantz, L. B. Shaw, I. D. Aggarwal, M. K. Poutous, *et al.*, "Anti-reflective surface structures for spinel ceramics and fused

- silica windows, lenses and optical fibers," *Optical Materials Express*, vol. 4, pp. 2504-2515, 2014.
- [16] A. Peltier, G. Sapkota, M. Potter, L. E. Busse, J. A. Frantz, L. Brandon, *et al.*, "Control of spectral transmission enhancement properties of random anti-reflecting surface structures fabricated using gold masking," in *Proc. of SPIE Vol.*, 2017, pp. 101150B-1.
- [17] S.-Y. Han, B. K. Paul, and C.-h. Chang, "Nanostructured ZnO as biomimetic anti-reflective coatings on textured silicon using a continuous solution process," *Journal of Materials Chemistry*, vol. 22, pp. 22906-22912, 2012.
- [18] Z.-P. Yang, L. Ci, J. A. Bur, S.-Y. Lin, and P. M. Ajayan, "Experimental observation of an extremely dark material made by a low-density nanotube array," *Nano letters*, vol. 8, pp. 446-451, 2008.
- [19] J. J. Steele and M. J. Brett, "Nanostructure engineering in porous columnar thin films: recent advances," *Journal of Materials Science: Materials in Electronics*, vol. 18, pp. 367-379, 2007.
- [20] M. Schulze, H. Fuchs, E. Kley, and A. Tünnermann, "New approach for antireflective fused silica surfaces by statistical nanostructures," in *Proc. SPIE*, 2008, p. 68830N.
- [21] N. Roxhed, P. Griss, and G. Stemme, "A method for tapered deep reactive ion etching using a modified Bosch process," *Journal of Micromechanics and Microengineering*, vol. 17, p. 1087, 2007.
- [22] C. Taylor, L. Busse, J. Frantz, J. Sanghera, I. Aggarwal, and M. Poutous, "Angle-of-incidence performance of random anti-reflection structures on curved surfaces," *Applied optics*, vol. 55, pp. 2203-2213, 2016.
- [23] E. R. Dougherty and R. A. Lotufo, "Hands-on morphological image processing," ed: SPIE press, 2003.
- [24] M. Schulze, D. Lehr, M. Helgert, E.-B. Kley, and A. Tünnermann, "Transmission enhanced optical lenses with self-organized antireflective subwavelength structures for the UV range," *Optics letters*, vol. 36, pp. 3924-3926, 2011.
- [25] C. Pacholski, C. Morhard, J. P. Spatz, D. Lehr, M. Schulze, E.-B. Kley, *et al.*, "Antireflective subwavelength structures on microlens arrays—comparison of various manufacturing techniques," *Applied optics*, vol. 51, pp. 8-14, 2012.
- [26] J. Elam, D. Routkevitch, P. Mardilovich, and S. George, "Conformal coating on ultrahigh-aspect-ratio nanopores of anodic alumina by atomic layer deposition," *Chemistry of Materials*, vol. 15, pp. 3507-3517, 2003.
- [27] T. Alasaarela, T. Saastamoinen, J. Hiltunen, A. Säynätjoki, A. Tervonen, P. Stenberg, *et al.*, "Atomic layer deposited titanium dioxide and its application in resonant waveguide grating," *Applied optics*, vol. 49, pp. 4321-4325, 2010.
- [28] A. Szeghalmi, E. B. Kley, and M. Knez, "Theoretical and experimental analysis of the sensitivity of guided mode resonance sensors," *The Journal of Physical Chemistry C*, vol. 114, pp. 21150-21157, 2010.
- [29] T. Weber, T. Käsebier, A. Szeghalmi, M. Knez, E.-B. Kley, and A. Tünnermann, "High aspect ratio deep UV wire grid polarizer fabricated by double patterning," *Microelectronic Engineering*, vol. 98, pp. 433-435, 2012.

- [30] H. Shimomura, Z. Gemici, R. E. Cohen, and M. F. Rubner, "Layer-by-layer-assembled high-performance broadband antireflection coatings," *ACS applied materials & interfaces*, vol. 2, pp. 813-820, 2010.
- [31] C. Martinet, V. Paillard, A. Gagnaire, and J. Joseph, "Deposition of SiO₂ and TiO₂ thin films by plasma enhanced chemical vapor deposition for antireflection coating," *Journal of Non-Crystalline Solids*, vol. 216, pp. 77-82, 1997.
- [32] N. Selvakumar and H. C. Barshilia, "Review of physical vapor deposited (PVD) spectrally selective coatings for mid-and high-temperature solar thermal applications," *Solar Energy Materials and Solar Cells*, vol. 98, pp. 1-23, 2012.
- [33] B. K. Kim, K.-H. Kim, J. Hong, W.-J. Kim, H. Ko, C. Huh, *et al.*, "Sensitivity response to coating material thickness for an optical resonant reflective biosensor based on a guided mode resonance filter," *BioChip Journal*, vol. 8, pp. 35-41, 2014.
- [34] C.-H. Chang, J. A. Dominguez-Caballero, H. J. Choi, and G. Barbastathis, "Nanostructured gradient-index antireflection diffractive optics," *Optics letters*, vol. 36, pp. 2354-2356, 2011.
- [35] D. J. Economou, "Modeling and simulation of plasma etching reactors for microelectronics," *Thin Solid Films*, vol. 365, pp. 348-367, 2000.
- [36] R. Hsiao and J. Carr, "Si/SiO₂ etching in high density SF₆/CHF₃/O₂ plasma," *Materials Science and Engineering: B*, vol. 52, pp. 63-77, 1998.
- [37] C. Cardinaud, M.-C. Peignon, and P.-Y. Tessier, "Plasma etching: principles, mechanisms, application to micro-and nano-technologies," *Applied Surface Science*, vol. 164, pp. 72-83, 2000.
- [38] S. Pearton and F. Ren, "Plasma etching of ZnS, ZnSe, CdS, and CdTe in electron cyclotron resonance CH₄/H₂/Ar and H₂/Ar discharges," *Journal of Vacuum Science & Technology B: Microelectronics and Nanometer Structures Processing, Measurement, and Phenomena*, vol. 11, pp. 15-19, 1993.
- [39] E. Gadelmawla, M. Koura, T. Maksoud, I. Elewa, and H. Soliman, "Roughness parameters," *Journal of Materials Processing Technology*, vol. 123, pp. 133-145, 2002.
- [40] *Cleartran manufacturer*. Available: <https://www.edmundoptics.com/f/zinc-sulfide-cleartran-windows/14004/>
- [41] *Cleartran Applications*. Available: <https://www.photonics.com/EDU/Handbook.aspx?AID=25495>
- [42] K. J. Major, C. M. Florea, M. K. Poutous, L. E. Busse, J. S. Sanghera, and I. D. Aggarwal, "Surface transmission enhancement of ZnS via continuous-wave laser microstructuring," in *SPIE LASE*, 2014, pp. 896810-896810-8.
- [43] M. A. Sheehy, L. Winston, J. E. Carey, C. M. Friend, and E. Mazur, "Role of the background gas in the morphology and optical properties of laser-microstructured silicon," *Chemistry of Materials*, vol. 17, pp. 3582-3586, 2005.
- [44] J. Zhu, G. Yin, M. Zhao, D. Chen, and L. Zhao, "Evolution of silicon surface microstructures by picosecond and femtosecond laser irradiations," *Applied Surface Science*, vol. 245, pp. 102-108, 2005.
- [45] A. Vorobyev and C. Guo, "Direct creation of black silicon using femtosecond laser pulses," *Applied Surface Science*, vol. 257, pp. 7291-7294, 2011.

- [46] M. J. Smith, M. Winkler, M.-J. Sher, Y.-T. Lin, E. Mazur, and S. Gradečak, "The effects of a thin film dopant precursor on the structure and properties of femtosecond-laser irradiated silicon," *Applied Physics A*, vol. 105, pp. 795-800, 2011.
- [47] W. Gong, Z. Zheng, J. Zheng, H. Zhao, X. Ren, and S. Lu, "Femtosecond laser induced submicrometer structures on the ablation crater walls of II–VI semiconductors in water," *Applied Surface Science*, vol. 255, pp. 4351-4354, 2009.
- [48] R. R. Gattass and E. Mazur, "Femtosecond laser micromachining in transparent materials," *Nature photonics*, vol. 2, p. 219, 2008.
- [49] T. Y. Choi, D. J. Hwang, and C. P. Grigoropoulos, "Femtosecond laser induced ablation of crystalline silicon upon double beam irradiation," *Applied surface science*, vol. 197, pp. 720-725, 2002.
- [50] D. Von der Linde, K. Sokolowski-Tinten, and J. Bialkowski, "Laser–solid interaction in the femtosecond time regime," *Applied Surface Science*, vol. 109, pp. 1-10, 1997.
- [51] J. Goldman and J. Prybyla, "Ultrafast dynamics of laser-excited electron distributions in silicon," *Physical review letters*, vol. 72, p. 1364, 1994.
- [52] D. Von der Linde and K. Sokolowski-Tinten, "The physical mechanisms of short-pulse laser ablation," *Applied Surface Science*, vol. 154, pp. 1-10, 2000.
- [53] J. A. Frantz, L. E. Busse, L. B. Shaw, J. S. Sanghera, I. D. Aggarwal, K. J. Major, *et al.*, "Antireflective Surface Structures on Optical Elements," ed: Google Patents, 2018.
- [54] X. Ye, X. Jiang, J. Huang, F. Geng, L. Sun, X. Zu, *et al.*, "Formation of broadband antireflective and superhydrophilic subwavelength structures on fused silica using one-step self-masking reactive ion etching," *Scientific reports*, vol. 5, p. 13023, 2015.
- [55] *VirtualLab Fusion*. Available: <https://www.lighttrans.com/>
- [56] K. Kunala, G. Sapkota, and M. K. Poutous, "Optical characterization of random anti-reflecting subwavelength surface structures on binary gratings," in *Optical Components and Materials XV*, 2018, p. 105280S.
- [57] K. Kunala and M. K. Poutous, "Diffraction efficiency performance of random anti-reflecting subwavelength surface structures on prefabricated fused silica binary gratings," *Applied optics*, vol. 57, pp. 4421-4427, 2018.

APPENDIX A: Publications

- **Karteek Kunala**, Gopal Sapkota, Menelaos K. Poutous, “Optical characterization of random anti-reflecting subwavelength surface structures on binary gratings”, **Proc SPIE Vol. 10528**, Optical Components and Materials XV, 105280S (February 2018).
- Menelaos K. Poutous, Ishwar D. Aggarwal, **Karteek Kunala**, Lynda E. Busse, Jesse A. Frantz, Leslie B. Shaw, Jsbinder S. Sanghera, Kevin J. Major, “Antireflective Surface Structures on Optical Elements”, **U.S. Patent Publication US20180136368A1** (May 2018). Patent Pending.
- **Karteek Kunala**, Menelaos K. Poutous, “Diffraction efficiency performance of random anti-reflecting subwavelength surface structures on pre-fabricated fused silica binary gratings”, **Appl. Opt.****57,4421-4427** (May 2018).
- **Karteek Kunala**, Menelaos K. Poutous, “Random anti-reflective nanostructuring on near-wavelength period gratings”, **Optical Engineering** **57(8)**, **087106** (August 2018).
- **Karteek Kunala**, Menelaos K. Poutous, “Angle of incidence performance of random anti-reflection structures on binary gratings”, **Optics Letters** (To be submitted October 2018).

APPENDIX B: List of Optical Components

Component	Specifications
Binary diffraction grating	1.595 μ m period, 50% duty cycle
Binary diffraction grating	1.166 μ m period, 50% duty cycle
Zinc Sulfide Cleartran Windows (Uncoated)	25mm diameter, 3mm thickness

Thorlabs Components

Component	Model	Quantity
Photodiode Power Sensor	S120C	1
Power Meter Console	PM100A	1
Graduated Ring-Actuated Iris Diaphragm	SM1D12C	1
Dual Scanning Slit Beam Profiler	BP209-IR	1
CCD Camera Beam Profiler	BC106N-VIS	1
Continuously variable ND filter	NDC-100C	1

Other Components

Component	Manufacturer	Model	Quantity
Tunable Helium-Neon (HeNe) Laser	Newport	R-30602/ R-30603	1